INVESTIGATIONS OF CEREBRAL HEMODYNAMICS IN INFANTS WITH CRITICAL CONGENITAL HEART DISEASE USING DIFFUSE OPTICS

Jennifer M. Lynch

A DISSERTATION

in

Physics and Astronomy

Presented to the Faculties of the University of Pennsylvania

in

Partial Fulfillment of the Requirements for the

Degree of Doctor of Philosophy

2014

Supervisor of Dissertation

_____

Arjun G. Yodh

James M. Skinner Professor of Science, Department of Physics and Astronomy

Graduate Group Chairperson

_____

Randall Kamien

Vicki and William Abrams Professor in the Natural Sciences, Department of Physics and Astronomy

Dissertation Committee

Gary Bernstein, Professor of Physics

Daniel Licht, Associate Professor of Neurology

Philip Nelson, Professor of Physics

Timothy Zhu, Professor of Radiation Oncology

Joel Greenberg, Professor of Neurology

INVESTIGATIONS OF CEREBRAL HEMODYNAMICS IN INFANTS WITH CRITICAL CONGENITAL HEART DISEASE USING DIFFUSE OPTICS

ACKNOWLEDGEMENT

I would like to thank a few key individuals for their contributions to this work and constant support during these past five years. I met my advisor Arjun Yodh while I was still in college. I came to Penn to work in his soft-condensed matter group, however within the first year I became more interested in biomedical optics. Arjun was extremely supportive of my decision to change research groups, and I am thankful for the opportunities he has given me. Arjun has been a great mentor, and I greatly appreciate everything he has taught me.

After switching into biomedical optics, I met Erin Buckley who was a graduate student working in Arjun's lab. I cannot express how invaluable Erin was during my first few years in this group. She taught me everything I needed to know to get started in the field and introduced me to amazing collaborators and mentors around Penn and at CHOP.

Specifically, Erin introduced me to Dan Licht, whose influence and generosity has shaped not only my work while in graduate school, but also my career path to follow. Under Dan's guidance, I have collaborated on extraordinary clinical projects, opportunities for which I am tremendously grateful. His patience over the past few years, as he continually re-explained physiology and medicine to a physicist, is greatly appreciated. Dan has been an invaluable mentor, whether listening to practice talks, giving career advice, or just lending an ear during stressful times.

I must thank the many other members of the Yodh and Licht labs who have helped me with this work as well as made these years in graduate school enjoyable. Peter Schwab, who has been a great friend to work with and made early morning MRIs much

more enjoyable; Maddie Winters, who made my life these past few years significantly easier, whether through taking more shifts during our studies or just listening to me vent; David Busch, who was always willing to work through problems with me and brainstorm; and the many other lab members who I have had the privilege to work with—Han Ban, Wes Baker, Tiffany Ko, Ann McCarthy, Steve Schenkel, Maryam Naim, and Ashwin Parthasarathy.

Last but not least, I thank my family for everything they have done to get me to this point. They have been there for me with unconditional support through every step of my life, and I greatly appreciate their love and guidance throughout my time in graduate school.

ABSTRACT

INVESTIGATIONS OF CEREBRAL HEMODYNAMICS IN INFANTS WITH CRITICAL CONGENITAL HEART DISEASE USING DIFFUSE OPTICS

Jennifer M. Lynch

Arjun G. Yodh

Congenital heart defects (CHD) are the most common type of birth defect, affecting approximately 30,000 children each year, one third of whom require cardiac surgery in their first year of life. Surgical advances have improved the cardiac outcomes for these children, and since the majority of these patients now reach school age, the research focus has shifted to address neurodevelopmental difficulties of survivors. A key physiological factor appears to be the high prevalence of hypoxic-ischemic white mater brain injury observed in these children. The exact timing of the injury occurrence, however, is difficult to ascertain due to limitations of the imaging modalities employed for this fragile, infant population.

This thesis develops and explores the use of diffuse optical spectroscopy techniques for investigation of the risk factors for hypoxic-ischemic brain injury in these infants. The optical techniques utilize near-infrared (NIR) light and the diffusion approximation to model light transport in order to probe the static and dynamic properties of tissue. Frequency-domain diffuse optical spectroscopy (FD-DOS) is a technology, similar to widely used near-infrared spectroscopy (NIRS), that permits quantification of tissue oxygen saturation and total hemoglobin concentration. Diffuse correlation spectroscopy (DCS) is a relatively newer technique, centered on an idea similar to

dynamic light scattering, which enables quantification of blood flow. Both FD-DOS and DCS are used in this research.

The experiments presented in this thesis explore a variety of biophysics and biomedical questions. Arguably, the most important clinical findings to emerge from this dissertation are new risk factors associated with brain injury in infants with a certain form of CHD called hypoplastic left heart syndrome (HLHS). Using the aforementioned optical techniques, we found that longer time-to-surgery, lower cerebral oxygen saturation, and higher cerebral blood flow measured on the morning of surgery were associated with the risk of acquiring post-operative brain injury in this cohort. The results are novel for the community and shift our understanding of when these neonates are most at risk for acquiring brain injury. Most importantly, these results and the technology developed should improve current clinical care of this patient population.

TABLE OF CONTENTS

1 Introduction 1

1.1 Critical Congenital Heart Disease 1

1.2 Associated Neurodevelopmental Outcomes 1

1.3 Periventricular Leukomalacia 1

1.4 Imaging and Monitoring of the Infant Brain 2

1.5 Novel Role of Diffuse Optical Spectroscopies 3

1.6 Summary and Thesis Organization 3

2 Diffuse Optical Spectroscopy 6

2.1 Photon Diffusion in Tissue 7

2.1.1 Diffuse Photon Density Waves (DPDWs) 9

2.1.2 Semi-Infinite Geometry 11

2.2 Phantom Calibration 15

2.3 Differential Pathlength Method 16

2.4 Frequency Domain Instrumentation 17

2.5 Calculation of Physiological Parameters 18

3 Quantification and Validation of Venous Oxygenation 20

3.1 Introduction 20

3.2 Materials and Methods 22

3.2.1 Population 22

3.2.2 Study Protocol 22

3.2.3 Data Analysis 23

3.2.4 Statistical Analysis 26

3.3 Results 27

3.3.1 Validation Study 27

3.3.2 Healthy Volunteers 30

3.4 Discussion 31

3.5 Conclusion/Future 33

4 Diffuse Correlation Spectroscopy 35

4.1 Dynamic Light Scattering 35

4.2 Correlation Diffusion Equation 37

4.3 Instrumentation 41

4.4 Validation Studies 42

4.5 Effect of optical properties on BFI 44

4.6 Cerebral effects of intravenous adenosine 46

4.6.1 Introduction 46

4.6.2 Methods 47

4.6.3 Results 49

4.6.4 Discussion 53

4.6.5 Conclusion 54

5 Diffuse Optical Measurements of Cerebral Oxygen Metabolism 55

5.1 Hybrid DOS/DCS Instrumentation 55

5.2 Calculation of Cerebral Metabolic Rate of Oxygen 56

5.3 Validation Studies 58

5.4 Cerebral hemodynamics in children with pulmonary hypertension 60

5.4.1 Introduction 60

5.4.2 Methods 61

5.4.3 Results 64

5.4.4 Discussion 66

5.4.5 Conclusion 66

6 Investigating risks for brain injury in infants with critical CHD 67

6.1 Introduction 67

6.1.1 Physiology of a healthy heart 69

6.1.2 Hypoplastic Left Heart Syndrome 70

6.1.3 Transposition of the Great Arteries 72

6.2 Study Protocol 73

6.2.1 Brain MRI 75

6.2.2 DOS/DCS Measurements 75

6.2.3 Statistical Analysis 76

6.3 Patient population 76

6.4 Results 78

6.4.1 Differences between HLHS and TGA 81

6.4.2 Risk factors for PVL in HLHS 86

6.4.3 Differences between HLHS and TGA: Revisited 100

6.4.4 Serial pre-operative measurements 102

6.5 Conclusion 104

7 Conclusions and Future Directions 105

LIST OF TABLES

Table 1: List of patient demographics for validation study of DOS measured SvO_2.....28

Table 2: List of measured parameters during cardiac catheterization for validation study of DOS measured SvO_2.....28

Table 3: Parts list for an 8-Channel, 2 laser DCS box.....42

Table 4: Summary of validation studies of DCS measurements of changes in BFI in human brain due to a perturbation.....43

Table 5: Summary of demographic data for subjects studied undergoing an ACMR.....50

Table 6: Description of groups used to categorize subjects.....77

Table 7 Demographic data for the infants with CHD studied.....78

Table 8: Preoperative optical variables for all infants with CHD studied.....79

Table 9: Postoperative optical variables for all infants with CHD studied.....80

Table 10: Pre-operative and post-operative volumes of PVL averaged over the four different groups of patients.....81

Table 11: Patient demographics for all infants with HLHS and TGA.....81

Table 12: Pre-operative and post-operative volumes of PVL averaged over the population of infants with HLHS and infants with TGA.....82

Table 13: Pre-operative optical variables for infants with HLHS and TGA.....84

Table 14: Post-operative variables measured with optics.....85

Table 15: Summary of demographic and pre- and post-operative cerebral hemodynamic variables measured for all subjects with HLHS.....88

Table 16: Summary of demographic and pre- and post-operative cerebral hemodynamic variables measured for subjects with and without new or worsened PVL > 76.3 mm^3 91

LIST OF FIGURES

Figure 1: A sample absorption spectrum of the main chromophores of tissue: HbO_2, Hb, and H_2O 6

Figure 2: Illustration of a semi-infinite geometry in a homogeneous medium 11

Figure 3: A diagram for the extrapolated boundary condition for the semi-infinite geometry 13

Figure 4: Linear relationships used to calculate k_i and k_r 14

Figure 5: Sample unfiltered time series, Fourier transform, and filtered time series of $\Delta[Hb]$ and $\Delta[HbO_2]$ 25

Figure 6: Flowchart of data processing for calculation of SvO_2^{DOS} 27

Figure 7: Cerebral venous saturation measured with near-infrared spectroscopy compared to venous saturation measured from a blood sample invasively taken from the SVC 29

Figure 8: Bland-Altman plot of the difference in SvO_2^{DOS} and SvO_2^{NIRS} versus the mean of these two parameters 30

Figure 9: The effect of the SNR cutoff for validation of SvO_2^{DOS} 32

Figure 10: Illustration depicting dynamic light scattering in the single scattering limit. 36

Figure 11: Sample DCS data from the frontal cortex of an infant undergoing a hypercapnia intervention 40

Figure 12: Picture of DCS module used in the work presented in this thesis. 41

Figure 13: Correlation of BFI measured with optics and CBF measured with VENC-MRI 44

Figure 14: Comparison of BFI calculated using various values of μ_s' to CBF measured with VENC-MRI 45

Figure 15: Schematic of study protocol 49

Figure 16: Changes in CBF due to an adenosine infusion in patients who are awake or anesthetized during the infusion 51

Figure 17: Changes in THC due to an adenosine infusion in patients who are awake or anesthetized during the infusion 51

Figure 18: Changes in HR due to an adenosine infusion in patients who are awake or anesthetized during the infusion 52

Figure 19: Hybrid DOS/DCS module used for the work presented in this thesis 56

Figure 20: Correlation of $CMRO_{2,i}$ measured with optics and $CMRO_2$ measured with MRI 59

Figure 21: Comparison of $CMRO_{2,i}$ calculated using various values of μ_s' to $CMRO_2$ measured with MRI 60

Figure 22: Picture of optical probe that combines optical fibers for DOS and DCS 62

Figure 23: Timeline of pulmonary hypertension study 62

Figure 24: Changes in StO_2 due to 40ppm iNO and due to the addition of 100% O_2 64

Figure 25: Relative changes in CBF due to 40ppm iNO and due to the addition of 100% O_2 65

Figure 26: Relative changes in OEF, CaO_2, and $CMRO_2$ due to 40ppm iNO and due to the addition of 100% O_2 65
Figure 27: Example of MR image depicting an infant brain with PVL 68
Figure 28: Schematic diagram of a healthy heart 69
Figure 29: Timeline of study of infants with CHD 74
Figure 30: Boxplot of post-operative PVL volumes for infants with HLHS and TGA 83
Figure 31: Boxplot of pre-operative optical variables for infants with HLHS and TGA 85
Figure 32: Boxplot of post-operative variables for infants with HLHS and TGA 86
Figure 33: Volumetric amount of pre- and post-operative PVL in neonates with HLHS 87
Figure 34: Change in volume of PVL between pre- and post-operative MRI scans 89
Figure 35: An example of a small volume and a large volume of PVL. 90
Figure 36: Boxplot of new or worsened PVL 93
Figure 37: Pre-operative cerebral oxygenation as a function of time-to-surgery 94
Figure 38: Pre-operative cerebral oxygenation as a function of pre-operative BFI 96
Figure 39: Pre-operative oxygen extraction fraction as a function of time-to-surgery and pre-operative BFI 98
Figure 40: Boxplots of pre-operative BFI for infants with HLHS and TGA who went to surgery earlier or later than day-of-life 4 101
Figure 41: Daily measurements of StO_2 from birth until surgery in subjects with HLHS and TGA 103

Figure 42: Daily measurements of BFI from birth until surgery in subjects with HLH and TGA 103

LIST OF ACRONYMS

ACMR	adenosine stress cardiac MR
ASL-MRI	arterial spin labeling magnetic resonance imaging
BFI	blood flow index
CaO_2	arterial oxygen concentration
CBF	cerebral blood flow
CBV	cerebral blood volume
CCC	concordance correlation coefficient
CHD	congenital heart defect
CHOP	the Children's Hospital of Philadelphia
CICU	cardiac intensive care unit
$CMRO_2$	cerebral metabolic rate of oxygen
$CMRO_{2,i}$	index of cerebral metabolic rate of oxygen
CoA	Coarctation of Aorta
CPB	cardiopulmonary bypass
DCS	diffuse correlation spectroscopy
DHCA	deep hypothermic circulatory arrest
DILV	double inlet left ventricle
DOS	diffuse optical spectroscopy
DPDW	diffuse photon density waves
Hb	deoxy-hemoglobin

HbO_2	oxy-hemoglobin
HLHS	hypoplastic left heart syndrome
HR	heart rate
IAA	interrupted aortic arch
iNO	inhaled nitric oxide
IQR	interquartile range
MRI	magnetic resonance imaging
NIRS	near-infrared spectroscopy
NO	nitric oxide
NP	Nasopharyngeal
OEF	oxygen extraction fraction
PA	pulmonary atresia
PET	positron emission tomography
PH	pulmonary hypertension
PVL	periventricular leukomalacia
RTE	radiative transfer equation
SaO_2	arterial oxygen saturation
SNR	signal-to-noise ratio
StO_2	cerebral tissue oxygen saturation
SVC	superior vena cava
SvO_2	venous oxygen saturation
TCD	transcranial Doppler ultrasound

TGA	transposition of the great arteries
THC	total hemoglobin concentration
TMS	total maturation score
ToF	Tetralogy of Fallot
VENC-MRI	velocity encoded magnetic resonance imaging
VSD	ventricular septal defect
Xenon-CT	xenon-enhanced computer tomography

1 Introduction

1.1 Critical Congenital Heart Disease

Congenital heart defects (CHD) are among the most common birth defects in humans. CHD affect 1 out of every 120 babies in the United States and over 1 million babies worldwide. Complex congenital heart defects account for approximately a third of these cases. Infants born with these complex defects require cardiac surgery in their first few months of life [1]. Two common complex congenital heart defects that are the focus of the work presented in this thesis are transposition of the great arteries and hypoplastic left heart syndrome. These specific defects are described in detail in Section 6.1.

1.2 Associated Neurodevelopmental Outcomes

Surgical advances over the last 20 years have significantly improved survival and cardiac outcomes in infants with critical CHD. Now that more of these children are reaching school age, neurodevelopmental dysfunction has been reported to occur in approximately half of all survivors [2]. These school-age survivors are at higher risk for inattention and hyperactivity, impaired cognitive and fine motor skills, learning and speech disabilities, and lower IQs [3-6]. Thus, the focus of research has now shifted to improvement of the neurocognitive outcomes in this population.

1.3 Periventricular Leukomalacia

The underlying cause of the high prevalence of neurobehavioral symptoms seen in children with CHD is believed to be the high prevalence of a specific form of brain

injury called periventricular leukomalacia (PVL) [7]. PVL is a specific form of hypoxic-ischemic white matter injury that commonly occurs in a vascular watershed zone near the lateral ventricles. This region of white matter is highly susceptible to hypoxic-ischemic injury during early brain development due to the maturation stage of the oligodendrocytes [8]. PVL is most often observed in preterm neonates, who have neurodevelopmental outcomes remarkably similar to those of term patients with CHD. This injury is observed in magnetic resonance imaging (MRI) scans as T1-hyperintense lesions, further enabling quantification of injury severity [7, 9, 10]. However, the exact timing of this injury remains unknown.

1.4 Imaging and Monitoring of the Infant Brain

To elucidate the timing and cause of PVL, a monitor of cerebral oxygenation and blood flow during periods of highest risk is imperative. Although various techniques are available and have been used for imaging and monitoring the infant brain, all of these techniques have associated disadvantages. A complete summary of these techniques and their advantages and disadvantages has been reported [11, 12].

Current established tools for measuring cerebral blood flow (CBF) include various forms of MRI, transcranial Doppler ultrasound (TCD), positron emission tomography (PET) and Xenon enhanced computer tomography (Xenon-CT). A major disadvantage of most of these techniques is that they can only be used as spot measurements of CBF, i.e., they cannot be employed for continuous monitoring. This situation presents a significant limitation for investigation of periods of risk for infants with CHD, because they may be susceptible to PVL during long pre-operative, operative

and post-operative time periods. While TCD can be used for non-invasive monitoring of cerebral hemodynamics, assumptions about the cerebral vessel diameters can cause large errors in measurements of cerebral blood flow velocity. TCD is also unable to measure regional variations in cerebral blood flow. Additionally, PET and Xe-133 expose the patient to radiation, which can be particularly harmful to neonates.

1.5 Novel Role of Diffuse Optical Spectroscopies

Thus there exists an unfilled niche for a non-ionizing, non-invasive, continuous monitor of cerebral hemodynamics for neonates. Diffuse optical spectroscopy (DOS) and diffuse correlation spectroscopy (DCS) are optical techniques based on the diffusion approximation for light transport that enable quantification of cerebral oxygenation, total hemoglobin concentration, and blood flow. These optical techniques are non-invasive, utilize non-ionizing radiation, and can be deployed at the bedside. Since they can be performed at the patient's bedside, they permit continuous monitoring of cerebral hemodynamic parameters, a capability that most other modalities fail to provide. I describe these techniques in further detail in Sections 2 and 4.

1.6 Summary and Thesis Organization

Neonates with critical CHD experience a high risk for neurobehavioral symptoms later in life and an associated hypoxic-ischemic white matter injury termed PVL. And, as noted above, diffuse optical spectroscopies provide a novel tool for monitoring cerebral oxygenation and blood flow in these neonates that enables elucidation of the

exact timing and cause of this brain injury. I will describe my research on this problem and related studies of hemodynamics in the baby brain.

In Chapter 2 of this thesis, I describe the instrumental and theoretical ideas that underpin DOS. In Chapter 3, I explain research that I have done further developing and validating a novel that utilizes frequency-filtered DOS for determination of cerebral venous oxygenation. This work has led to a publication [13].

In Chapter 4, I describe the physics associated with DCS, and I describe the DCS instrument that I assembled and used for the results presented here. I also describe work that I have done in validating this technique in-vivo, which has also been published [14]. Finally, I demonstrate an important new clinical use for DCS, i.e., I describe a clinical study that I conducted wherein I employ DCS to measure changes in cerebral blood flow due to clinically administered adenosine. This work is currently in preparation for publication and has been presented at an international conference [15].

In Chapter 5, I describe the combined use of DOS and DCS for measuring cerebral oxygen metabolism. I first discuss the hybrid instrument that I assembled. I then describe work that I did in validating measurements of cerebral oxygen metabolism, which has led to a publication [14]. Finally, I describe work demonstrating the clinical usefulness of hybrid DOS/DCS measurements in a clinical study measuring cerebral oxygen metabolism in children with pulmonary hypertension.

Finally, in Chapter 6, I describe an investigation on a cohort of infants with CHD that I have been studying for the past 4 years. I summarize what we have learned through the use of diffuse optics about the underlying cause for brain injury seen in this cohort. I

will specifically highlight my major clinical result, which has led to a publication [16] on predictive risk factors for brain injury in certain forms of CHD.

2 Diffuse Optical Spectroscopy

Diffuse optical spectroscopy (DOS), also known as Near-Infrared Spectroscopy (NIRS), utilizes near-infrared light to noninvasively probe the optical properties of tissue, namely tissue absorption and scattering. The primary NIR-light-absorbing chromophores in brain tissue are oxy-hemoglobin (HbO_2), deoxy-hemoglobin, (Hb) and water (H_2O). Thus, by quantifying the light absorption of tissue, one can derive and elucidate clinically meaningful physiological parameters from the concentrations of these chromophores.

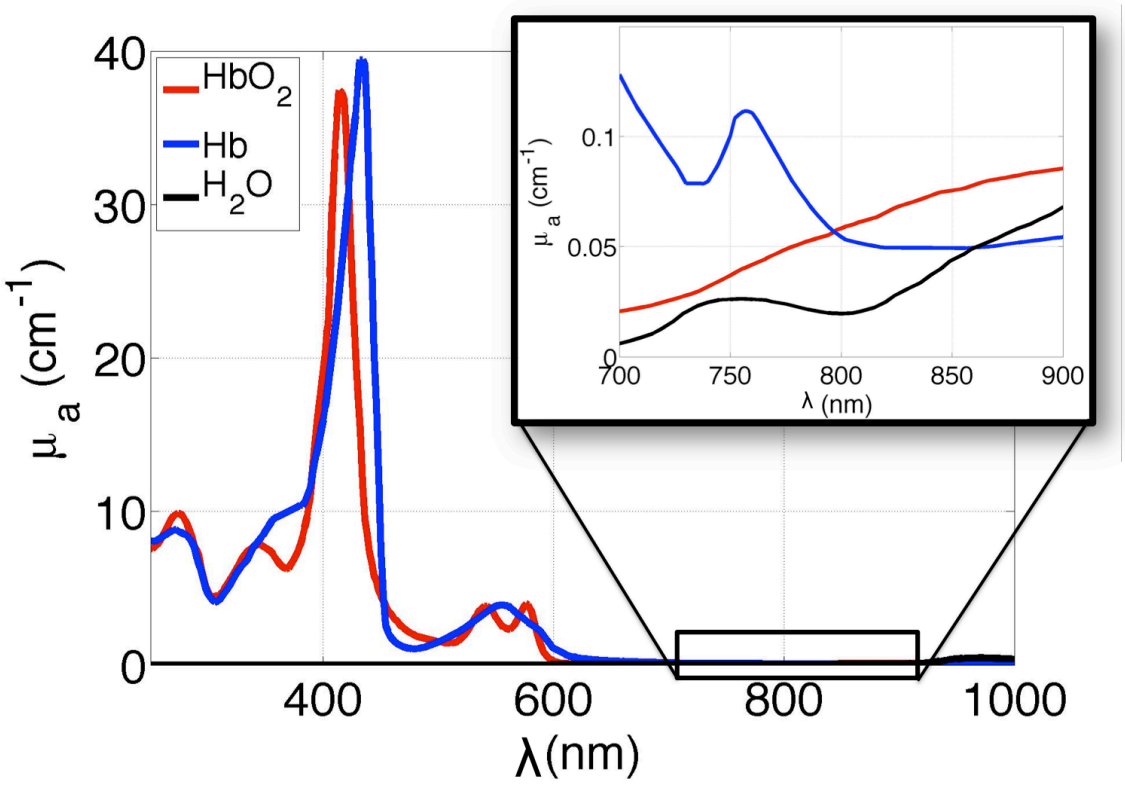

Figure 1: A sample absorption spectrum of the main chromophores of tissue: HbO_2 (red), Hb (blue), and H_2O (black). The zoomed-in region depicts the NIR region of light in which scattering, not absorption, dominates for biological tissue, allowing for photons to deeply penetrate.

To understand why wavelengths in the near-infrared (NIR) are well-suited for DOS, Figure 1 shows an example of the absorption spectra of the main chromophores in brain tissue. This plot shows the wavelength-dependent absorption coefficient, $\mu_a(\lambda)$, in units of cm^{-1}, as a function of wavelength (λ) for the three main chromophores in brain tissue. The absorption coefficient of a tissue chromophore, $\mu_a(\lambda)$, is the inverse of the mean distance that a photon of wavelength λ travels in tissue containing that chromophore before it has an e^{-1} probability of having been absorbed. Inside the NIR region, the absorption of light is low, permitting deep penetration of photons. Additionally in this region, the spectral dependence of the absorption of light due to the three main chromophores is distinct, thereby permitting separation of the effects of each chromophore (Figure 1).

In order to quantify the amount of light that is absorbed by different components of the tissue and thus quantify $\mu_a(\lambda)$, one needs to separate out the light scattering property of tissue from the light absorbing property of tissue. The wavelength-dependent scattering coefficient, $\mu_s(\lambda)$, is the inverse of the mean distance that a photon of wavelength λ travels in tissue before it has an e^{-1} probability of having been scattered. The following section will discuss how one separates the effects of these two optical properties. Later in this chapter, I will describe the instrumentation employed to carry out these measurements and, finally, the physiological parameters that can be extracted.

2.1 Photon Diffusion in Tissue

NIR light propagation through tissue can be approximated as a diffusive process, with each photon traveling along a random walk trajectory. Mathematical modeling of

the transport of photon energy in tissue typically begins with the radiative transfer equation (RTE) [17]

$$\frac{1}{v}\frac{\partial L(\vec{r},\hat{s},t)}{\partial t} + \nabla \cdot L(\vec{r},\hat{s},t)\hat{s} = -\mu_t L(\vec{r},\hat{s},t) + \mu_s \int L(\vec{r},\hat{s},t)\, f(\hat{s}',\hat{s})ds' + S(\vec{r},\hat{s},t). \quad (2.1)$$

Here the radiance, $L(\vec{r},\hat{s},t)$, is described using conservation of energy and is defined as the power of light per unit area traveling in direction $\hat{s}$ around position $\vec{r}$ at time t with units W/(cm^2·sr); v is the speed of light in the medium; μ_t is the total transport coefficient defined as $\mu_t = \mu_a + \mu_s$; $f(\hat{s}',\hat{s})$ is essentially the probability of light scattering in a single event from the $\hat{s}'$ direction into the $\hat{s}$ direction; and $S(\vec{r},\hat{s},t)$ is the term representing the light source. This equation assumes that the scattering and absorption lengths are much larger than the wavelength of the light, that the light is unpolarized, and that v is spatially homogeneous throughout the medium. The diffusion approximation of light transport describes the photon fluence rate, $\Phi(r,t)$, and the photon current density, $\vec{J}(\vec{r},t)$, which are related to light radiance as follows:

$$\Phi(\vec{r},t) = \int L(\vec{r},\hat{s},t)\, d\hat{s}; \quad (2.2)$$

$$\vec{J}(\vec{r},t) = \int L(\vec{r},\hat{s},t)\, \hat{s} d\hat{s}. \quad (2.3)$$

The RTE is simplified by expanding terms using spherical harmonics:

$$L(\vec{r},\hat{s},t) \approx \sum_{l=0}^{N}\sum_{m=-l}^{l} \Phi_{l,m}(\vec{r},t) Y_{l,m}(\hat{s}); \quad (2.4)$$

$$S(\vec{r},\hat{s},t) = \sum_{l=0}^{N}\sum_{m=-l}^{l} q_{l,m}(\vec{r},t) Y_{l,m}(\hat{s}). \quad (2.5)$$

For nearly isotropic radiance, a P_1 approximation can be performed to leave only the $l = 0$ and $l = 1$ terms [18, 19], and then it is readily shown that

$$L(\vec{r},\hat{s},t) = \frac{1}{4\pi}\Phi(\vec{r},t) + \frac{3}{4\pi}\vec{J}(\vec{r},t)\cdot\hat{s}. \tag{2.6}$$

Thus with this approximation of an isotropic source and an additional assumption of isotropic scattering (i.e., $f(\hat{s}',\hat{s}) = f(\hat{s}'\cdot\hat{s})$), the RTE can be simplified to the photon diffusion equation:

$$\nabla\cdot\left((D(\vec{r})\nabla\,\Phi(\vec{r},t)\right) - v\mu_a(\vec{r})\Phi(\vec{r},t) + vS(\vec{r},t) = \frac{\partial\Phi(\vec{r},t)}{\partial t}. \tag{2.7}$$

Here, $D(\vec{r})$ is the photon diffusion coefficient in units of cm^2/s and is defined as:

$$D(\vec{r}) = \frac{v}{3(\mu_s'(\vec{r})+\mu_a(\vec{r}))} \cong \frac{v}{3(\mu_s'(\vec{r}))}. \tag{2.8}$$

The reduced scattering coefficient, μ_s' is related to the scattering coefficient by $\mu_s'(\vec{r}) = \mu_s(1-g)$, where g is defined as the average cosine angle of a scattering event,

$$g = \int f(\hat{s}\cdot\hat{s}')\hat{s}\cdot\hat{s}'ds' = \langle cos\theta\rangle. \tag{2.9}$$

Thus, μ_s' is approximately the mean inverse distance a photon travels before its direction has an e^{-1} probability of becoming randomized (i.e., the inverse distance of μ_s' is the photon random walk step).

The photon diffusion equation can be further simplified by assuming that tissue is a homogeneous medium, i.e., $D(\vec{r}) = D$, $\mu_s'(\vec{r}) = \mu_s'$ and $\mu_a(\vec{r}) = \mu_a$. The resulting simplified equation is:

$$D\nabla^2\,\Phi(\vec{r}) - v\mu_a\Phi(\vec{r},t) + vS(\vec{r},t) = \frac{\partial\Phi(\vec{r},t)}{\partial t}. \tag{2.10}$$

2.1.1 Diffuse Photon Density Waves (DPDWs)

The work presented in this thesis utilizes Frequency Domain DOS (FD-DOS), which is a specific technique of exploiting the photon diffusion equation to quantitatively

estimate the tissue optical properties μ_a and μ_s'. In FD-DOS, the intensity of the light source is modulated sinusoidally at an angular frequency ω. Thus, a point source at the origin can be expressed as:

$$S(\vec{r}, t) \equiv (S_{DC} + S_0 e^{-i\omega t})\delta(\vec{r} = 0). \tag{2.11}$$

This source produces a fluence rate in the medium composed of an AC and a DC component that can be expressed as:

$$\Phi(\vec{r}, t) \equiv \Phi_{DC}(\vec{r}) + \Phi(\vec{r})e^{-i\omega t}. \tag{2.12}$$

The AC component of the fluence rate represents the propagation of diffuse photon density waves (DPDWs) that result when modulated light travels through a highly scattering medium such as tissue [19]. Isolating the AC component of the fluence rate, the photon diffusion equation becomes:

$$D\nabla^2 \Phi(\vec{r}) - v\mu_a\Phi(\vec{r}) + vS_0\delta(0) = -i\omega\Phi(\vec{r}). \tag{2.13}$$

This equation can be rewritten in Helmholtz equation form as:

$$(\nabla^2 + k^2)\,\Phi(\vec{r}) = -\frac{vS_0}{D}\delta(0), \tag{2.14}$$

where $k^2 = (i\omega - v\mu_a)/D$.

For an infinite homogeneous geometry, this equation has a closed form analytical solution [18, 19]:

$$\Phi(\vec{r}) = \frac{vS_0}{4\pi D}\frac{e^{ikr}}{r}, \tag{2.15}$$

where $k = k_r + ik_i = \sqrt{(i\omega - v\mu_a)/D}$ is the complex wave vector. Note that this solution describes an overdamped spherical wave radiating outward from the source. These fluence rate waves are often called diffuse photon density waves (DPDWs) or

diffusive waves. The real and imaginary components of the wavevector can be expressed as:

$$k_r = \sqrt{\frac{v\mu_a}{2D}}\left[\sqrt{1+\left(\frac{\omega}{v\mu_a}\right)^2}-1\right]^{1/2}; \tag{2.16}$$

$$k_i = \sqrt{\frac{v\mu_a}{2D}}\left[\sqrt{1+\left(\frac{\omega}{v\mu_a}\right)^2}+1\right]^{1/2}. \tag{2.17}$$

Therefore, measurement of k_r and k_i enables determination of tissue μ_a and μ_s'.

2.1.2 Semi-Infinite Geometry

For many real-world biomedical applications, including those presented in this thesis, a semi-infinite geometry is more appropriate than an infinite geometry. Here, the source and detector optical fibers are placed on the surface of tissue, and boundary conditions are imposed on the photon propagation. A depiction of this geometry is shown in Figure 2.

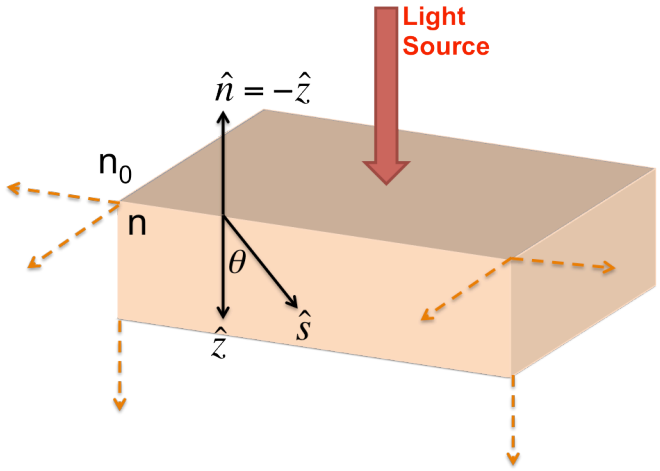

Figure 2: Illustration of a semi-infinite geometry in a homogeneous medium. The turbid homogeneous medium (tissue) with index of refraction n is separated by a planar boundary at z=0 from a non-scattering medium with index of refraction n_0.

In the applications of DOS in this thesis, the boundary is often made between tissue ($n = 1.4$) and silicon rubber ($n_0 = 1.4$), which is the material from which we make our optical probes that house the fiber optics. Typically, once diffuse light exits the tissue into the non-scattering medium, it will never return to the tissue. We can express the total inward radiance at the boundary as the integral of the reflected radiance [17]:

$$E_{in} = \int_0^{2\pi} \int_{\pi/2}^{\pi} R_{Fresnel}(\hat{s}) L(\hat{s}) \cdot \hat{n} sin\theta d\theta d\phi. \tag{2.18}$$

Here, E_{in} is the total incoming diffuse radiance and $R_{Fresnel}$ is the Fresnel reflection coefficient, which can be expressed as

$$R_{Fresnel}(\theta) = \begin{cases} \frac{1}{2}\left(\frac{ncos\theta' - n_0 cos\theta}{ncos\theta' + n_0 cos\theta}\right)^{1/2} + \frac{1}{2}\left(\frac{ncos\theta - n_0 cos\theta'}{ncos\theta + n_0 cos\theta'}\right)^{1/2} & ; 0 \le \theta \le \theta_C \\ 1 & ; \theta_C \le \theta \le \pi/2 \end{cases} \tag{2.19}$$

where θ is the angle of incidence; θ' is the refracted angle; and θ_C is the critical angle. Evaluating this equation for the inward radiance using the approximation for nearly isotropic radiance yields the partial-flux boundary condition [17]:

$$\phi = \frac{1+R_j}{1-R_\phi}(-2j_z), \tag{2.20}$$

where j_z is the magnitude of the photon flux in the $\hat{z}$-direction and:

$$R_\phi \equiv \int_0^{\frac{\pi}{2}} 2sin\theta\, cos\theta R_{Fresnel}(\theta) d\theta; \tag{2.21}$$

$$R_j \equiv \int_0^{\frac{\pi}{2}} 3sin\theta\, cos^2\theta R_{Fresnel}(\theta) d\theta. \tag{2.22}$$

At the tissue surface, i.e., $z = 0$, the partial-flux boundary condition translates to:

$$\phi = 2D \frac{1+R_{eff}}{1-R_{eff}} \frac{d\phi}{dz}, \tag{2.23}$$

at z=0, where R_{eff} is defined as

$$R_{eff} = \frac{R_\Phi + R_j}{2 - R_\Phi + R_j}. \tag{2.24}$$

However, the partial-flux boundary condition is difficult to use in practice, so we approximate with the extrapolated-zero boundary condition where the fluence rate falls to zero at a point z_b on the rubber probe side of the boundary (i.e., $\Phi(z = -z_b) = 0$), where $z_b = -\frac{2}{3\mu_s'}$ [17]. The method of images can then be used to find the solution to the diffusion equation given this boundary condition.

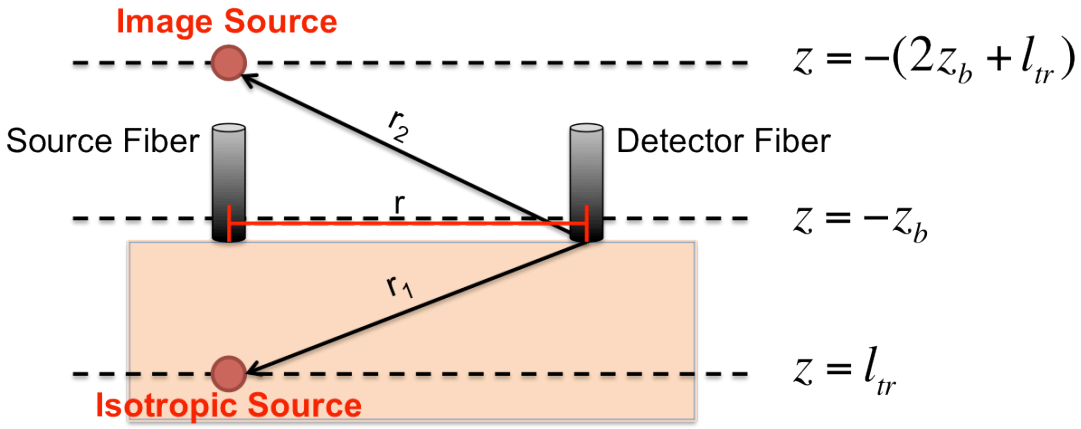

Figure 3: A diagram for the extrapolated boundary condition for the semi-infinite geometry. An extrapolated boundary exists at $z = -z_b$ where the fluence rate falls to 0. The method of images is used to solve for a solution for $\Phi(\vec{r})$.

As shown in **Figure 3**, given a source placed at $z = l_{tr}$, an added source with the same magnitude but opposite sign placed at $z = -(2z_b + l_{tr})$ will satisfy the boundary condition. Thus, the solution to the diffusion equation is:

$$\Phi(\vec{r}) = \frac{vS_0}{4\pi D}\left[\frac{e^{ikr_1}}{r_1} - \frac{e^{ikr_2}}{r_2}\right], \tag{2.25}$$

where $r_1 = \sqrt{r^2 + (z - l_{tr})^2}$, $r_2 = \sqrt{r^2 + (z + l_{tr} + 2z_b)^2}$ and $r = |\vec{r}|$ is the source-detector separation.

For a source-detector separation $r = |\vec{r}| \gg l_{tr}$, the above solution for the diffusion equation can be simplified as:

$$\Phi(\vec{r}) = \frac{vS_0}{4\pi D}\frac{e^{-kr}}{r^2}[2k(l_{tr}z_b + {z_b}^2)] = A(r)e^{i\theta(r)}, \tag{2.26}$$

where $A(r)$ is the amplitude and $\theta(r)$ is the phase of the detected light [20, 21]. From this equation, the following two relationships can be derived:

$$\ln(A(\vec{r})r^2) = -k_i r + A_0; \tag{2.27}$$

$$\theta(\vec{r}) = k_r r + \theta_0. \tag{2.28}$$

where k_i and k_r depend on the absorption and scattering properties of the medium.

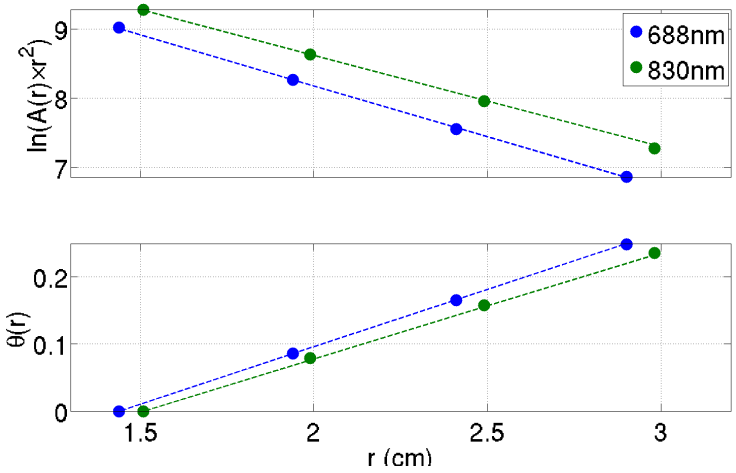

Figure 4: Linear relationships used to calculate $\boldsymbol{k_i}$ and $\boldsymbol{k_r}$. The top figure shows the linear relationship of $\boldsymbol{\ln(A(\vec{r})r^2)}$ versus $\boldsymbol{r}$, the slope of which is $\boldsymbol{-k_i}$. The bottom figure shows the linear relationship of $\boldsymbol{\theta(\vec{r})}$ versus $\boldsymbol{r}$, the slope of which is $\boldsymbol{k_r}$.

The slope of the linear relationship of $\ln(A(\vec{r})r^2)$ versus r is $-k_i$. Similarly, the slope of the linear relationship of $\theta(\vec{r})$ versus r is k_r. Thus, by measuring the amplitude attenuation and phase shift for multiple values of $|\vec{r}|$, the tissue optical properties can be calculated from the following equations:

$$\mu_a = \frac{\omega}{2v}\left(\frac{k_i}{k_r} - \frac{k_r}{k_i}\right); \tag{2.29}$$

$$\mu_s{}' = \frac{2v}{3\omega} k_i k_r. \tag{2.30}$$

The frequency domain formulation for diffuse optical spectroscopy (FD-DOS) provides a very powerful approach to estimate tissue optical properties. However, practical considerations, such as differences in tissue-fiber light coupling efficiencies and the need for multiple detector positions, lead to some limitations of the technique. I address these limitations in the following sections.

2.2 Phantom Calibration

One primary requirement for the effective use of the FD-DOS formulation is the need to make the frequency domain measurements at multiple source-detector separations. In practice, measurements at multiple source-detector separations (i.e., multiple values of $r = |\vec{r}|$) are accomplished by using multiple source fibers placed at different distances with respect to a single detection fiber on the surface of the skin. Unfortunately, the efficiencies of light coupling of multiple fibers to the tissue cannot be assumed to be uniform. Therefore, the measurements must be calibrated to account for variations in the transmission of these fibers and variations in laser intensity. To do this,

we define a coupling coefficient for each source, c_i. Then, the measured fluence rate is related to the theoretical fluence rate for the i^{th} source by the following equation:

$$\Phi_i^{measured} = c_i \Phi_i^{theoretical}. \tag{2.31}$$

This equation can be expanded to separate the amplitude and phase contributions, resulting in the following two equations:

$$A_i^{measured} = c_i^A A_i^{theoretical}; \tag{2.32}$$

$$\theta_i^{measured} = c_i^P + \theta_i^{theoretical}. \tag{2.33}$$

To determine these coupling coefficients, we conduct measurements on a phantom of known optical properties, i.e., a known $A_i^{theoretical}$ and $\theta_i^{theoretical}$.

2.3 Differential Pathlength Method

One practical consideration for the FD-DOS formulation is the need to make measurements at more than one source detector separation; multiple separations enable one to quantitatively estimate tissue optical properties. When multiple source-detector separations are not possible, however, valuable information can still be extracted about *changes* in $\mu_a(\lambda)$ over time and thus *changes* in physiological parameters as a function of time (see Section 2.5). Although the Beer-Lambert Law, in its traditional form, cannot be used due to the high-scattering of tissue, a modified version of this law can be derived which is useful for estimating changes in the tissue absorption coefficient. This modified Beer-Lambert law is written as [22]:

$$\ln\left(\frac{I(\lambda,t)}{I(\lambda,0)}\right) = \Delta\mu_a(\lambda,t) L_{eff}(\lambda), \tag{2.34}$$

or

$$\Delta\mu_a(\lambda, t) = \frac{\ln\left(\frac{I(\lambda,t)}{I(\lambda,0)}\right)}{L_{eff}(\lambda)}. \quad (2.35)$$

Here, $\Delta\mu_a(\lambda, t)$ is the change from baseline (t=0) in the absorption coefficient at wavelength λ; $I(\lambda, t)$ is the intensity of detected light; and $L_{eff}(\lambda)$ is the mean optical pathlength of detected photons. $L_{eff}(\lambda)$ depends on the source-detector separation, the sample geometry, and the wavelength of light. For the work presented in this thesis, I use a population average value for $L_{eff}(\lambda)$ for neonates reported by Duncan et al. [23].

2.4 Frequency Domain Instrumentation

The DOS instrument used in this work was a custom designed, commercially available device assembled by ISS. This device contains 16 source laser diodes consisting of 4 different wavelengths of light (690nm, 730nm, 780nm, 830nm). A radio-frequency (RF) oscillator modulates the amplitude of the light source sinusoidally at 110 MHz. The light is delivered to and detected at the tissue surface by optical fibers. The device contains two photomultiplier tubes, which are employed for heterodyne detection.

As opposed to homodyne detection in which the amplitude and phase shifts are detected at the same RF carrier frequency that modulates the light source, heterodyne detection converts the detected RF signal to a lower frequency before determination of the phase shift. In this system, the source signal is modulated at 100 MHz while the detection is modulated at 110 MHz + 5kHz. Mixing these two signals yields a slower beat frequency of 5kHz, which allow measurement of the phase shift with a higher accuracy.

2.5 Calculation of Physiological Parameters

As stated previously, μ_a is related to the concentration of the NIR light absorbing chromophores. The absorption coefficient is essentially a linear combination of the extinction coefficient of the chromophores weighted by their concentration in the sampling volume and can be described by the following equation:

$$\mu_a(\lambda) = \sum_i \varepsilon_i(\lambda) C_i. \tag{2.36}$$

Here $\varepsilon_i(\lambda)$ is the wavelength-dependent extinction coefficient of the i^{th} chromophore at wavelength λ and C_i is the concentration of the chromophore. Assuming that the dominant chromophores in brain tissue are oxy-hemoglobin (HbO_2), deoxy-hemoglobin (Hb), and water (H_2O), the measured $\mu_a(\lambda)$ of brain tissue can be expressed as:

$$\mu_a(\lambda) = \varepsilon_{HbO_2}(\lambda) C_{HbO_2} + \varepsilon_{Hb}(\lambda) C_{Hb} + \varepsilon_{H_2O}(\lambda) C_{H_2O} \tag{2.37}$$

These extinction coefficients have been measured and reported previously [24]. All of the results reported in this thesis were measured using only two wavelengths, 690 nm and 830 nm; to solve the system of equations for C_{HbO_2} and C_{Hb}, I assumed the water concentration of brain tissue to be 75% [25][1]. Once C_{HbO_2} and C_{Hb} have been calculated, total hemoglobin concentration (THC) and tissue oxygen saturation (StO_2) can be calculated using the following equations:

[1] Due to the relatively low absorbance of water in the NIR, an error in the assumed 75% water concentration has a minimal effect on the calculated concentrations of Hb and HbO_2 and thus on StO_2. A difference in water concentration of 5% would yield a difference in StO_2 of approximately 1%.

$$THC = C_{HbO_2} + C_{Hb};$$ (2.38)

$$StO_2 = \frac{C_{HbO_2}}{THC} \times 100\%.$$ (2.39)

Cerebral blood volume (CBV, units of mL/100 g brain tissue) can be calculated from THC from the following formula:

$$CBV = \frac{THC \times MW_{Hb}}{[Hgb] \times R \times D_{bt} \times 10^5} = \frac{0.89 \times THC}{[Hgb]},$$ (2.40)

where MW_{Hb}=6.45x10^4 [g/moles] is the molecular weight of hemoglobin, $[Hgb]$ is the concentration of arterial hemoglobin, R=0.69 is the cerebral small-to-large vessel hematocrit ratio, and D_{bt} is the density of brain tissue. For the results presented in this thesis on neonates, the value used for D_{bt} was 1.05 g/mL [26].

Additionally, oxygen extraction fraction (OEF) can be calculated from StO_2 and arterial oxygenation (SaO_2) measured from an arterial blood sample using the following formula:

$$OEF = \frac{SaO_2 - SvO_2}{SaO_2} = \frac{1}{\gamma}\frac{SaO_2 - StO_2}{SaO_2},$$ (2.41)

where γ is the percentage of blood in the venous compartment and is assumed to be 75% [27].

3 Quantification and Validation of Venous Oxygenation

In the previous chapter, I described DOS and FD-DOS, and I described how this technique is used to measure tissue oxygen saturation (StO_2). In this chapter, I describe an experiment that I have done to extract only the venous component of the signal. Thus, I am able to use DOS to measure venous oxygen saturation (SvO_2). The work presented in this chapter has been published in [13].

3.1 Introduction

Quantitative measures of oxygen extraction are important for assessment of brain tissue health in many critically-ill patient populations at risk for altered cerebral hemodynamics. Knowledge of cerebral oxygen extraction helps the clinician balance oxygen delivery with cerebral demand thus preventing cell death secondary to metabolic failure.

As explained in Section 2.5, in order to calculate oxygen extraction fraction from StO_2, one needs to assume that a certain percentage of the probed blood volume, typically 75%, is from the venous system. This is because optically-measured StO_2 represents the oxygenation of the microvasculature in the volume underneath the probe, and this tissue volume is composed of capillaries, arterioles, and venules.

While the assumption of 75% provides a rough rule of thumb, it is not always valid. Thus, a method for isolating the venous component of the optical signal to quantify SvO_2 would be very useful. Typically, such schemes require a functional perturbation of cerebral blood volume to isolate the venous component of the optical signal, such as tilting of the head or venous occlusion [28-30]. However, these perturbation-based

measurements do not offer the possibility of continuous monitoring of SvO_2. Furthermore, the potential to use such perturbations in clinical settings is limited. For example, postural manipulation in preterm infants has been shown to cause changes in intracranial pressure, increasing the risk of intracranial hemorrhage [31].

As an alternative to functional perturbation methods for quantification of SvO_2, isolation of the venous component of the DOS signal using the oscillations of venous blood volume caused by respiratory excursions has been suggested [32-35]. Briefly, the method, which we employ herein, relies on the fact that blood volume in the veins oscillates at the respiration rate. This sensitivity to the venous portion of the vasculature arises because of the relatively large compliance of veins; pressure oscillations induced by the diaphragm motion during breathing thus affect the venous components of the vasculature much more than the rest of the vasculature [35, 36]. This method has been employed in neonates [35] and adults [37],[34],[32], and it has been validated against the gold standard venous blood draw in the hind leg of piglets [37]. While encouraging, the total number of studies is quite limited, and rigorous validation of this method in humans has not been performed.

In this chapter, I validate this respiratory-frequency-locked DOS method in humans for the first time against gold standard invasive measurements of central venous saturation. The investigation was carried out in a human pediatric population with pulmonary hypertension undergoing cardiac catheterization. This population is attractive for validation, because all subjects are mechanically ventilated at a constant respiration rate and because superior vena cava (SVC) saturations are measured as part of the clinical

protocol. In addition, I applied this method to five healthy volunteers to demonstrate that it can be generalized to populations whose respiration rate is volitionally, not mechanically, controlled.

3.2 Materials and Methods

3.2.1 Population

The pulmonary hypertension team at the Children's Hospital of Philadelphia identified and screened for study inclusion all patients undergoing cardiac catheterization to diagnose or treat pulmonary hypertension and who were approached for participation. All subjects had pulmonary hypertension and were receiving an intravascular catheterization procedure for clinical purposes. Blood samples from the SVC were obtained as part of the clinical procedure to quantify venous oxygenation.

In addition to this validation study, five healthy adult volunteers were recruited to test the method feasibility for use in other populations.

This study was approved by the Children's Hospital of Philadelphia Institutional Review Board.

3.2.2 Study Protocol

All subjects in the validation study were placed under general anesthesia (via sevo- and isoflurane and pancuronium) and mechanically ventilated on room air. After sedation, a flexible black rubber optical probe was placed on the right or left side of the subject's forehead and secured with an elastic bandage. As a part of routine clinical care,

a central venous catheter was placed, using access from the right internal jugular vein (n=3) or a femoral vein (n=7). Access to the superior vena cava (SVC), between the right subclavian and left innominate veins, was thus obtained and confirmed with fluoroscopy. After hemodynamic stability was confirmed, a blood sample from the SVC was obtained and cerebral venous oxygen saturation (SvO_2^{SVC}) was quantified using a whole blood oximeter (Avoximeter 1000E). Immediately after obtaining the SVC blood sample, DOS data were acquired continuously at 6 Hz for 2 minutes in order to optically derive SvO_2. Vital signs, including blood pressure and heart rate, were monitored continuously.

To demonstrate the feasibility of the frequency-filtered, non-invasive DOS method in other populations (e.g., non-ventilated healthy humans), we acquired optical data from five healthy volunteers. The same optical probe was secured to the volunteer's forehead with an elastic bandage. DOS data were acquired for 10 minutes at approximately 6 Hz. During data acquisition, the subject was instructed to inhale to the beat of a metronome set at the subject's resting state respiration (approximately 0.18 Hz) in order to maintain a steady respiration rate.

3.2.3 Data Analysis

The optically derived DOS data was first processed to estimate changes in concentrations of oxy- and deoxy-hemoglobin, using the procedure described in Section 2.3. Using the time series of $\Delta[HbO_2]$ and $\Delta[Hb]$ and following the method outlined in [37], I derive a measure of venous oxygen saturation, which I denote herein as SvO_2^{DOS},

that represents the microvasculature underneath the optical probe that is secured to the subject's forehead. Briefly, this method quantifies the changes in [HbO_2] and [Hb] which occur at the respiration frequency and makes the assumption that these changes are happening mostly in the veins.

Specifically, I apply a narrow bandpass frequency filter (filter.m, Mathworks) to the concentration time series, in order to select contributions only from frequencies within 1% of the subject's known respiration rate. The resultant filtered times series of [HbO_2] and [Hb] variation, i.e., with frequencies within 1% of the respiration rate, is due to mostly venous blood, since the venous blood volume will be oscillating predominantly at this frequency. This resultant filtered time series is exhibited in Figure 5**e** and **f**. I assume that the saturation of the blood that is displaced from the veins during respiration is representative of the saturation of all venous blood. I calculate the saturation of the displaced blood by first quantifying the amplitudes for each period of these filtered time series, denoted herein as $A_{\Delta[\mathrm{Hb}]_{resp}}$ and $A_{\Delta[\mathrm{HbO_2}]_{resp}}$. Then $SvO_2{}^{DOS}$ is calculated for each period as

$$\mathrm{SvO_2^{NIRS}} = \frac{A_{\Delta[\mathrm{HbO_2}]_{resp}}}{A_{\Delta[\mathrm{Hb}]resp} + A_{\Delta[\mathrm{HbO_2}]_{resp}}} \times 100\%. \quad \textbf{(3.1)}$$

A value of $SvO_2{}^{DOS}$ for each subject is obtained by averaging over all periods.

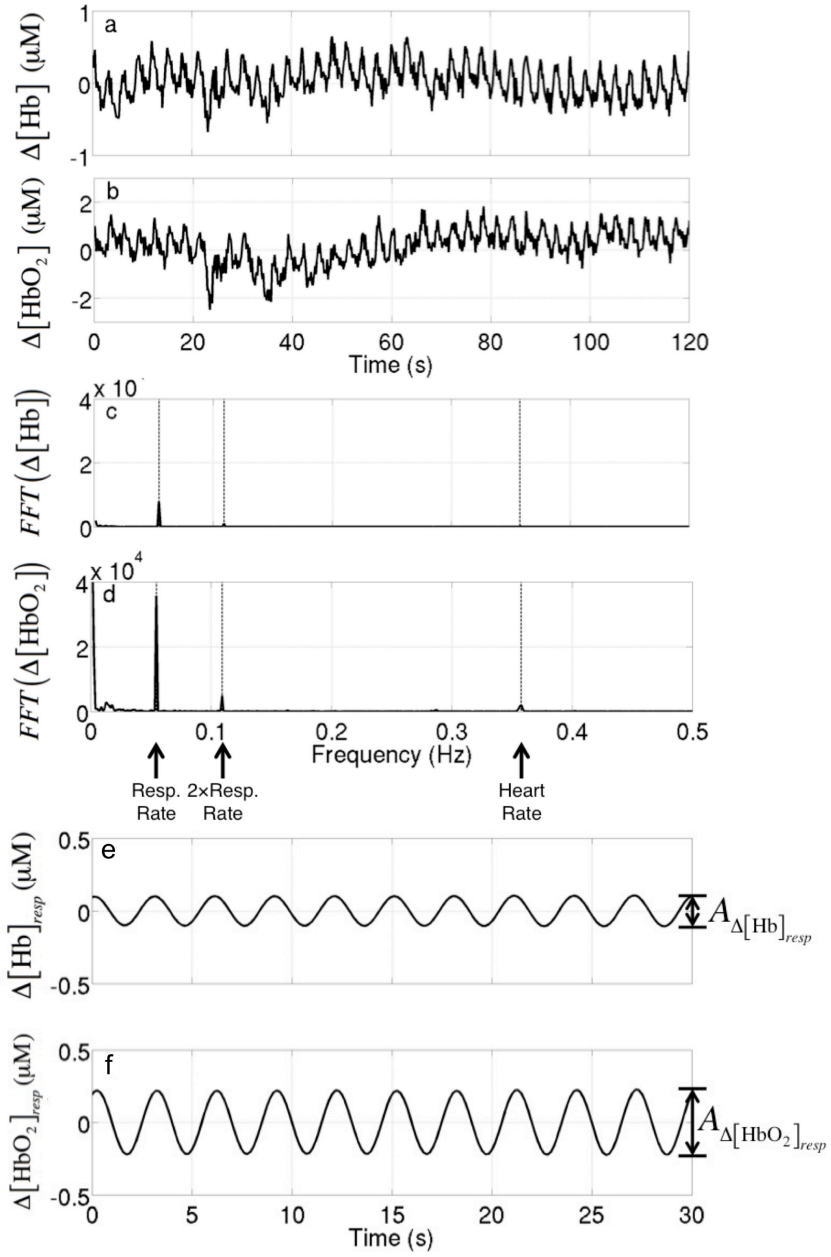

Figure 5: Sample unfiltered time series, Fourier transform, and filtered time series of Δ[Hb] and Δ[HbO_2]. Figures (a) and (b) depict unfiltered time series of Δ[Hb] (and Δ[HbO_2], respectively. Figures (c) and (d) show the Fourier transform of the Δ[Hb] time series and the Δ[HbO_2] time series, respectively. The dashed lines mark the respiration rate, the second harmonic of the respiration rate, and the heart rate. The bottom two plots show sample time series of Δ[Hb] (e) and Δ[HbO_2] (f) after bandpass filtering at the respiration rate/frequency.

The data quality of this measurement is related to the signal strength at the respiration rate/frequency. To evaluate this signal strength, I compare the peak of the Fourier component of the signal at the respiration rate/frequency to the standard deviation of the Fourier components of the signal at nearby frequencies. Specifically, I define a signal-to-noise ratio for both Δ[Hb] and Δ[HbO_2] to be $SNR_{Hb} = \frac{(FFT(Hb))_{freq=resp}}{\sigma_{freq<resp}}$ and $SNR_{HbO_2} = \frac{(FFT(HbO_2))_{freq=resp}}{\sigma_{freq<resp}}$, respectively. Here $(FFT(Hb))_{freq=resp}$ is the peak of the Fourier signal of Δ[Hb] at the respiration frequency (Figure 5), and $\sigma_{freq<resp}$ is the standard deviation of the Fourier signals at frequencies between the respiration rate/frequency and 32.5 mHz less than the respiration rate/frequency. In practice, I only utilize the standard deviation at lower frequencies, because the variance in the Fourier signal of the lower frequencies is large compared to that at the higher frequencies. All data with $SNR_{HbO_2} < 2.5$ and/or $SNR_{Hb} < 2.5$ is excluded from the subsequent analysis. This process is summarized in Figure 6.

3.2.4 Statistical Analysis

All statistical analyses were performed using R 2.11 software [38]. Statistical significance was declared for p-values < 0.05. To quantify the relationship between venous saturation measured non-invasively with DOS (SvO_2^{DOS}) and venous saturation measured from blood samples drawn from the SVC (SVO_2^{SVC}), I fit a simple linear regression model. I report the Pearson's correlation coefficient, R, which varies from 0 to 1.0 to estimate the extent to which a linear model explains variability in the data. Note that R gives only a measure of linear correlation. To quantify the agreement between

SvO_2^{DOS} and SVO_2^{SVC}, we report Lin's concordance correlation coefficient, CCC, which combines a measure of precision and accuracy [39]. A Bland-Altman plot was constructed to visualize the extent of agreement between the two methods [40].

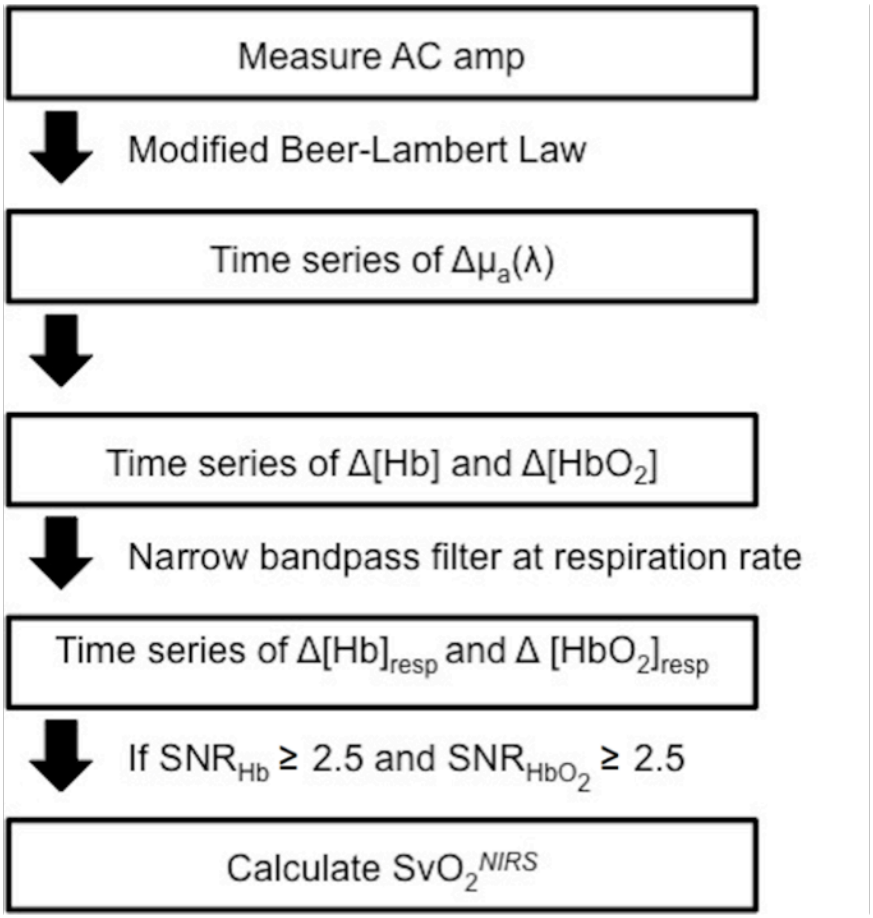

Figure 6: Flowchart of data processing for calculation of SvO_2^{DOS}.

3.3 Results

3.3.1 Validation Study

Twenty-two patients were consented for this study. Of this population, 10 patients (with ages from 2 months to 14 years) had both SVC blood samples obtained

during the catheterization and usable optical data (i.e., based on the criteria stated in Section 2.3). Patient characteristics are summarized in Table 1.

Table 1: List of patient demographics for validation study of DOS measured SvO_2. Continuous variable are listed as median (interquartile range, IQR).

	Median (IQR)
Age (yrs)	5.3 (1.3, 9.7)
Weight (kg)	15.3 (8.7, 24.1)
Height (cm)	99.9 (69.9, 124.8)
Sex (Male:Female)	5:5

Table 2: List of measured parameters during cardiac catheterization for validation study of DOS measured SvO_2. Continuous variables are listed as median (interquartile range, IQR).

	Median (IQR)
Respiration Rate (breaths per min)	20 (17, 20)
Heart Rate (beats per min)	103 (87, 134)
SvO_2^{SVC} (%)	64 (62, 67)
SvO_2^{DOS} (%)	59.6 (56.4, 65.9)
SNR_{Hb}	50.0 (16.5, 111.0)
SNR_{HbO_2}	25.5 (18.4, 51.8)

Table 2 shows median (interquartile range, IQR) SvO_2 measured with both DOS and co-oximetry. As shown in Figure 7, we see a strong and significant linear relationship ($R^2 = 0.80,\ p < 0.001$) between optically measured SvO_2^{DOS} and the venous saturation measured invasively from the SVC (SvO_2^{SVC}) with a slope (95% confidence interval) of $1.16\ (0.68, 1.64)$. The Bland-Altman plot (Figure 8) for these

two measurements suggests good agreement, with a mean difference of

$2.61\ (-4.56, 9.77)$. The concordance coefficient of 0.80 is high.

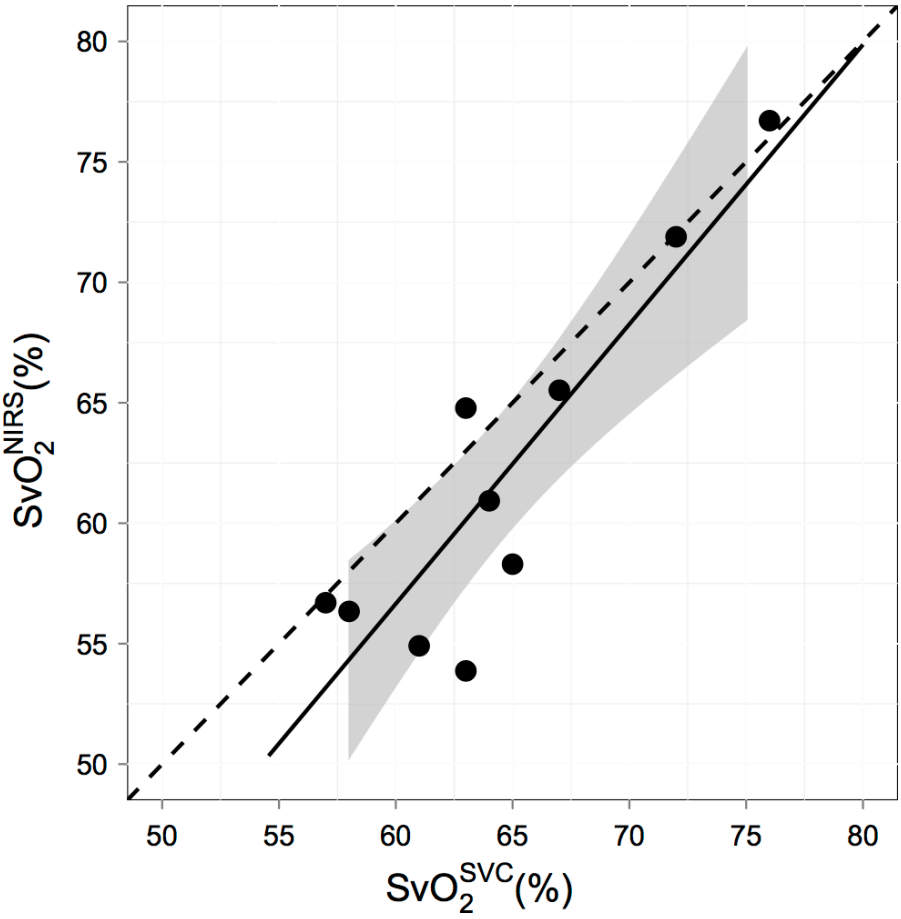

Figure 7: Cerebral venous saturation measured with near-infrared spectroscopy compared to venous saturation measured from a blood sample invasively taken from the SVC. The solid line represents the best-fit line to the data (R^2=0.80, p<0.001); the dashed line indicates the line of perfect concordance; and the gray ribbon denotes the 95% confidence interval for the mean SvO_2^{NIRS}.

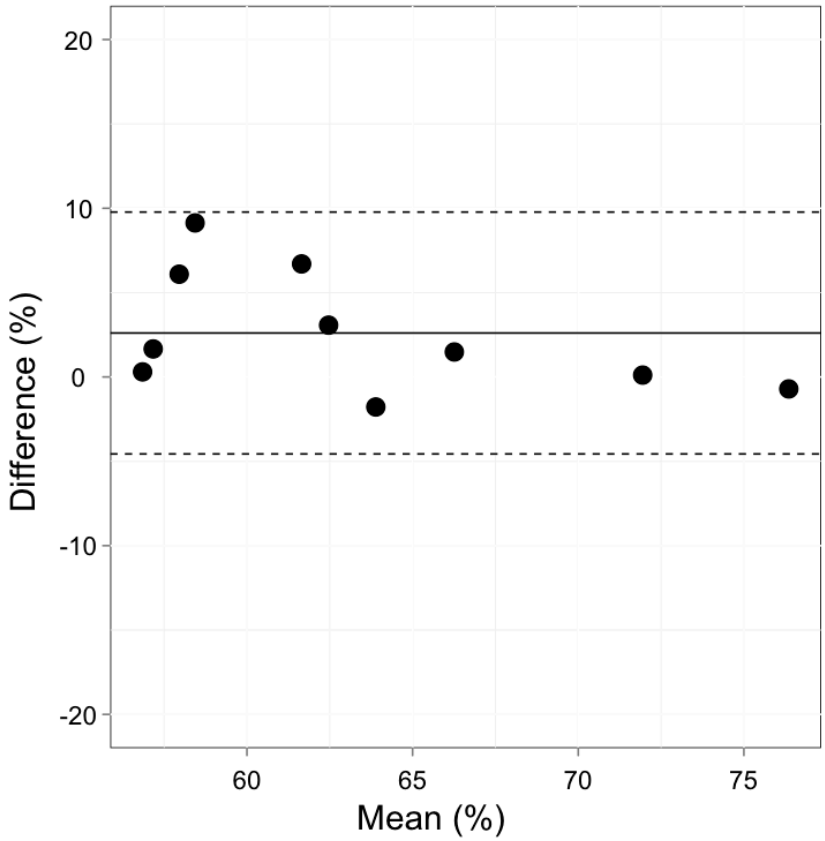

Figure 8: Bland-Altman plot of the difference in SvO_2^{DOS} and SvO_2^{NIRS} versus the mean of these two parameters. The solid horizontal line indicates the mean difference between these two parameters; the dotted lines indicate the 95% limits of agreement.

3.3.2 Healthy Volunteers

To demonstrate feasibility in other populations, SvO_2^{DOS} was measured in five healthy volunteers. The average (standard deviation) SvO_2^{DOS} calculated over a 10 minute period in each healthy subject was 79.4 (6.8)%. This value is in good agreement with the expected average central venous saturation for a healthy adult of 76.8±1.0% [41]. Importantly, even though these subjects were awake and were not using a respirator, the data quality was sufficient for accurate determination of SvO_2^{DOS} in each

subject, with an average (standard deviation) SNR_{HbO_2} of 57.6 (33.8) and SNR_{Hb} of 31.9 (27.5).

3.4 Discussion

Significant ($R^2 = 0.80, p < 0.001$) correlation and agreement (slope $= 1.16 \pm 0.48$) was observed between cerebral venous saturations determined by respiration-frequency filtered DOS and by the gold standard measurement of central venous saturation, i.e., oximetry of blood samples taken from the SVC. SvO_2^{DOS} is a measure of the venous saturation in the microvasculature underneath the optical probe that is secured to the subject forehead. SvO_2^{SVC} is a measure of central venous saturation, which includes venous saturation of the brain and upper extremities. Roughly speaking, we would expect these values to be similar in anesthetized patients wherein the vast majority of oxygen consumption occurs in the brain. Thus, even though the two methods derive venous saturation from two different vasculatures, the agreement between them is encouraging.

I measured SvO_2^{DOS} in free-breathing volunteers to demonstrate the feasibility of this technique in subjects who are not mechanically ventilated. The measured SvO_2^{DOS} in the healthy volunteers is in good agreement with the average central venous saturation for a healthy adult of 76.8±1.0% [41] illustrating feasibility of this method in other (less-controlled) populations.

One of the main limitations of the optical method derives from use of a bandpass filter for isolating the respiration frequency. Optical data were acquired on 20 subjects;

however, SvO_2^{DOS} was only calculated for 10 of these subjects due to poor SNR_{HbO_2} or poor SNR_{Hb}. I found that lowering this SNR cut-off to below 2 in this patient group introduces significantly more scatter into the total population data, thus it is imperative to maintain a high SNR for this measurement. To illustrate the effect of this SNR cut-off on the validation results reported herein, Figure 9 shows the R^2 and p-value and the number of subjects for the correlation between SvO_2^{DOS} and SvO_2^{SVC} for different values of this SNR cut-off.

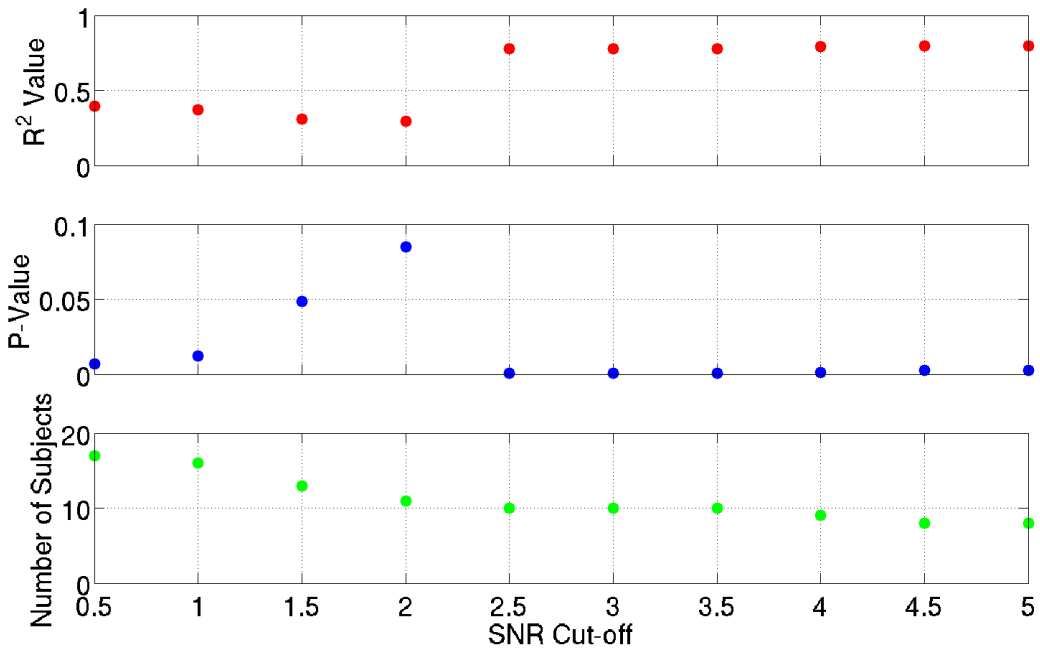

Figure 9: The effect of the SNR cutoff for validation of SvO_2^{DOS}. For different values of the SNR cutoff, the plots show the effect on the R^2 value of the correlation between SvO_2^{DOS} and SvO_2^{SVC} (top), on the p-value of this correlation (middle), and on the number of subjects that pass this cut-off (bottom).

Many factors can contribute to poor SNR, all of which lead to a less pronounced signal peak at the respiration rate in the frequency domain. These factors include motion artifacts, low amplitude of detected light, and irregular respiration. To minimize motion

artifacts, I found that it is imperative to secure the optical probe with an elastic bandage, e.g., instead of manually holding the probe during measurement. This adjustment in the measurement protocol yielded improved data quality in later recruited subjects. I also observed that SNR can be improved by acquiring data for longer than 2 minutes, but due to the restraints of the clinical setting, improvement of SNR was not possible in this study. In future studies, this SNR criteria can provide a useful new filter for data quality for this measurement.

Despite the caveats noted above, the method proved to work quite well in this patient population. Our worst deviation from SvO_2^{SVC} was less than 10%, which is encouraging given the approximate nature of the models used in the analysis. Of note, SvO_2^{DOS} is a measure of the *local* venous saturation of the vasculature probed by the NIR light. In many cases of injury or impairment wherein heterogeneity of cerebral saturations may exist, e.g., stroke, hemorrhage, etc., the optical method need not yield a quantity that is representative of the global cerebral SvO_2 and thus should not be expected to agree with SvO_2^{SVC}. These deviations, however, could find use for monitoring local injury and therapy responses.

3.5 Conclusion/Future

In this chapter, I have validated respiratory-frequency filtered diffuse optical spectroscopy (DOS) as a measure of cerebral venous oxygen saturation against a gold standard measurement in humans. Specifically, I employed DOS to measure SvO_2^{DOS} immediately after clinicians measured SvO_2^{SVC} and found good agreement between these two methods. I also demonstrated the feasibility for generalizing this method to other

populations by measuring SvO_2^{DOS} in healthy volunteers. Validation of this technique against the clinical gold standard in humans is the first step towards its wide use in clinical setting. Further work is needed to realize the potential of this non-invasive monitor of cerebral SvO_2 for management of critically ill patients with high risk of ischemic brain injury. Specifically, maximizing the SNR is crucial for widespread use of this technique. Along these lines, future work will focus on the use of this method in patients who are not mechanically ventilated and thus may not have a steady respiration rate.

4 Diffuse Correlation Spectroscopy

In this section, I will describe a second optical technique that is used to probe the dynamic properties of tissue, namely blood flow. I begin this chapter by discussing dynamic light scattering, which utilizes speckle fluctuations to derive information on the motion of small particles. Diffusion correlation spectroscopy (DCS) is similar to dynamic light scattering, in that it derives information on the motion of red blood cells using the speckle fluctuations of light that has traveled through biological tissue [42, 43]. I will discuss both techniques, and then I will describe the DCS instrument that I assembled and troubleshot which was used for the work presented in this thesis. I will then describe work that I have done in validating DCS in infants with congenital heart disease. Finally, I will demonstrate the clinical usefulness of DCS by describing a clinical study in which I utilized DCS to quantify changes in cerebral blood flow due to a clinically administered drug called adenosine.

4.1 Dynamic Light Scattering

Dynamic light scattering (DLS) is a method of measuring the motion of particles in a suspension using scattered light. In the single-scattering limit, the suspension is assumed to be dilute enough such that light traveling through the sample is either scattered once or not at all.

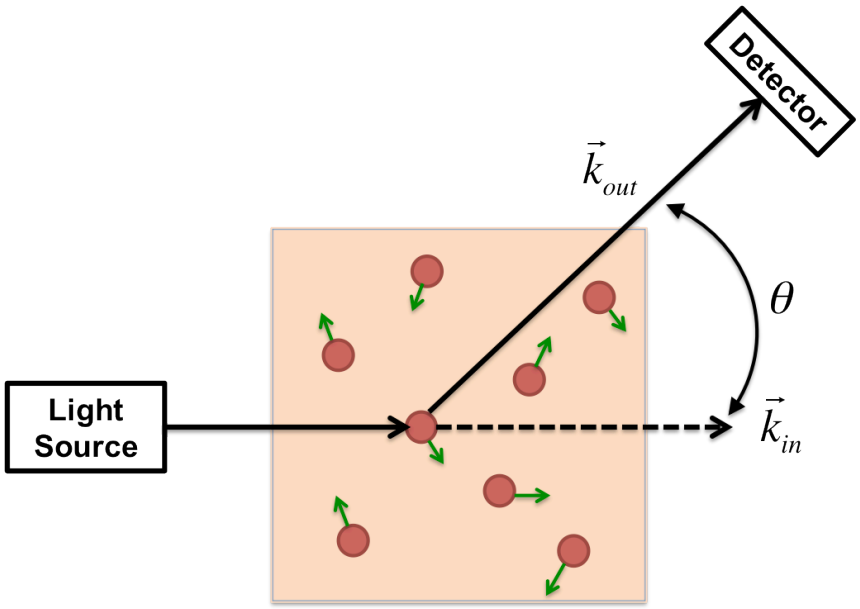

Figure 10: Illustration depicting dynamic light scattering in the single scattering limit.

As seen in Figure 10, in this single-scattering experiment, the incident light electric field ($\vec{k}_{in}$) is scattered by an angle which results in a momentum transfer, $\vec{q} = \vec{k}_{out} - \vec{k}_{in}$. The motion of particles and the scattering of the light cause constructive and destructive interference patterns for the light electric field at the detector, $\vec{E}(t)$, which changes over time. For independent particles, these detected fluctuations can be described by the normalized electric field temporal auto-correlation function [44-46]:

$$g_1(\tau) = \frac{\langle \vec{E}^*(t) \cdot \vec{E}(t+\tau) \rangle}{\langle |\vec{E}(t)|^2 \rangle} = e^{i2\pi f \tau} e^{-q^2 \langle \Delta r^2(\tau) \rangle / 6}. \quad (4.1)$$

Here, f is the frequency of incident light, and $\langle \Delta r^2(\tau) \rangle$ is the mean-square displacement of particles where $\langle\ \rangle$ denotes an ensemble average, which is assumed to be the same as the time average for the data presented in this thesis (and for most situations). For Brownian motion, $\langle \Delta r^2(\tau) \rangle = 6 D_b \tau$, where D_b is an effective Brownian diffusion

coefficient of the particle. For random flow, $\langle \Delta r^2(\tau) \rangle = \langle V^2 \rangle \tau^2$, where V is the second moment of the particle speed distribution.

In experiments, the light intensity auto-correlation function, $g_2(\tau)$, is often detected instead of the electric field auto-correlation function. The normalized intensity temporal auto-correlation function is defined as:

$$g_2(\tau) = \frac{\langle I(t) I(t+\tau) \rangle}{\langle I(t)^2 \rangle}. \tag{4.2}$$

$g_2(\tau)$ is related to $g_1(\tau)$ by the Siegert relation:

$$g_2(\tau) = 1 + \beta |g_1(\tau)|^2. \tag{4.3}$$

Here, β is inversely proportional to the number of detected light modes and is thus a constant that depends on the detection optics, coherence length and stability of the laser, and ambient light. Note, the Siegert relation is valid for Gaussian sources.

4.2 Correlation Diffusion Equation

In the above section, I described the single-scattering limit of DLS. However, biological tissue is a highly scattering medium. Ackerson et al [47] suggested that in this case, the unnormalized electric field auto-correlation function, $G_1(\tau) = \langle \vec{E}^*(\vec{r}, t) \cdot \vec{E}(\vec{r}, t+\tau) \rangle$, is analogous to the radiance and thus should obey a *correlation transfer equation*:

$$\nabla \cdot G_1(\vec{r}, \hat{s}, \tau)\hat{s} + \mu_t G_1(\vec{r}, \hat{s}, \tau) = Q(\vec{r}, \hat{s}) + \mu_s \int G_1(\vec{r}, \hat{s}', \tau)\, g_1(\hat{s}, \hat{s}', \tau) f(\hat{s}, \hat{s}') ds'. \tag{4.4}$$

As with the RTE, this correlation transport equation can be reduced to a correlation diffusion equation, and was done so by Boas et al. [42, 43]:

$$\left[\nabla \cdot (D(\vec{r})\nabla) - v\mu_a(\vec{r}) - \frac{\alpha}{3} v\mu_s' k_0^2 \langle \Delta r^2(\tau) \rangle\right] \mathrm{G}_1(\vec{r}, \tau) = -vS(\vec{r}). \tag{4.5}$$

Here, μ_a, μ_s', D, and v are the same as in the photon diffusion equation (see Section 2.1); α is the fraction of scattering events that occur from moving particles; k_0 is the wavenumber of light diffusion through the medium, and, again, $\langle \Delta r^2(\tau) \rangle$ is the mean-square displacement of the scattering particles. The main moving scatterers in tissue detected by DCS are red blood cells.

Several assumptions must be made in the derivation of this equation and have been described in depth [18]. Briefly, this equation assumes that the medium is highly scattering and isotropic, the scatterers are randomly oriented and have isotropic dynamics, and the correlation time is much less than the time it takes for the individual scatterers to move the wavelength of light.

The solutions for the correlation diffusion equation have the same form as the solutions for the photon diffusion equation. For the work presented in this thesis, I again assume a semi-infinite homogeneous medium with a tissue-silicon planar interface. Thus, the semi-infinite solution of $\mathrm{G}_1(\vec{r}, \tau)$ using an extrapolated boundary condition ($\mathrm{G}_1(z = -z_b, \tau) = 0$) and obtained with the method of images is (see Section 2.1) [18]:

$$\mathrm{G}_1(\vec{r}, \tau) = \frac{3\mu_s' S_0}{4\pi} \left(\frac{e^{-\kappa(\tau) r_1}}{r_1} - \frac{e^{-\kappa(\tau) r_2}}{r_2} \right), \tag{4.6}$$

where

$$\kappa(\tau) = \sqrt{\frac{v}{D} \left[\mu_a + \frac{\alpha}{3} \mu_s' k_0^2 \right] \langle \Delta r^2(\tau) \rangle}. \tag{4.7}$$

As with the solution for the photon diffusion equation, $r_1 = \sqrt{r^2 + (z - l_{tr})^2}$, $r_2 = \sqrt{r^2 + (z + l_{tr} + 2z_b)^2}$, and $l_{tr} = 1/\mu_s'$. The parameters α and $\langle \Delta r^2(\tau) \rangle$ are

related to the dynamics of the scatterers, i.e., blood flow. Due to the complex nature of microvasculature, we may expect the motion of the red blood cells to be nearly isotropic and that the mean-square displacement of particles can be described as random flow (i.e., $\langle \Delta r^2(\tau) \rangle = \langle V^2 \rangle \tau^2$). However, in practice, we find that the observed auto-correlation function more closely resembles the Brownian diffusion model (i.e., $\langle \Delta r^2(\tau) \rangle = 6 D_b \tau$). Thus, the equation for $\kappa(\tau)$ becomes:

$$\kappa(\tau) = \sqrt{\frac{v}{D}\left[\mu_a + \frac{\alpha}{3}\mu_s{}'\kappa_0^2\right] 6 D_b \tau}, \tag{4.8}$$

where αD_b depends on tissue dynamics. In the work presented in this thesis, the μ_a and $\mu_s{}'$ values measured with DOS are used for the fitting of the detected temporal intensity auto-correlation curve. We define a blood flow index, BFI:

$$BFI \equiv \alpha D_b. \tag{4.9}$$

A typical value for BFI for human brain tissue is of the order of 1×10^{-8} cm^2/s.

To illustrate how the measured intensity auto-correlation curves, and thus the fitted value for BFI, relate to cerebral blood flow, Figure 11 shows sample DCS data taken on the frontal cortex of an infant breathing room air (red curve), and then later breathing a mixture of room air and added CO_2. CO_2 acts as a cerebrovascular vasodilator and causes a significant increase in cerebral blood flow [48, 49]. As can be seen in Figure 11, the decay rate of g_2 decreases under these conditions, called hypercapnia. The fitted values of BFI for these two curves reflect the difference between the decay rates. BFI under the room air condition is 3.95×10^{-8} cm^2/s, while BFI under hypercapnia is 10.5×10^{-8} cm^2/s.

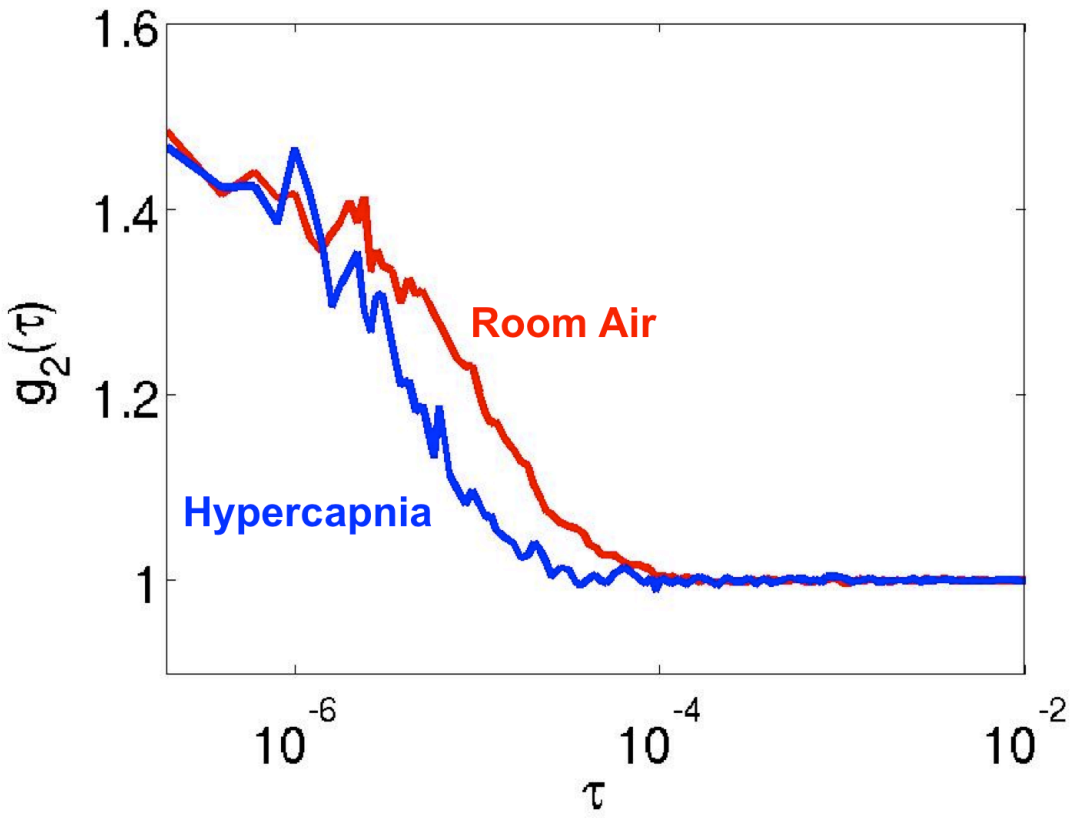

Figure 11: Sample DCS data from the frontal cortex of an infant undergoing a hypercapnia intervention. The red curve is the intensity auto-correlation curve from a frame of data taken when the patient was breathing room air. The blue curve is under hypercapnia.

In the following sections, I will describe the instrumentation used to measure BFI as well as validation studies comparing this value to other modalities for measuring cerebral blood flow.

4.3 Instrumentation

Figure 12 shows the DCS instrument that I assembled, troubleshot, and used for the work presented herein.

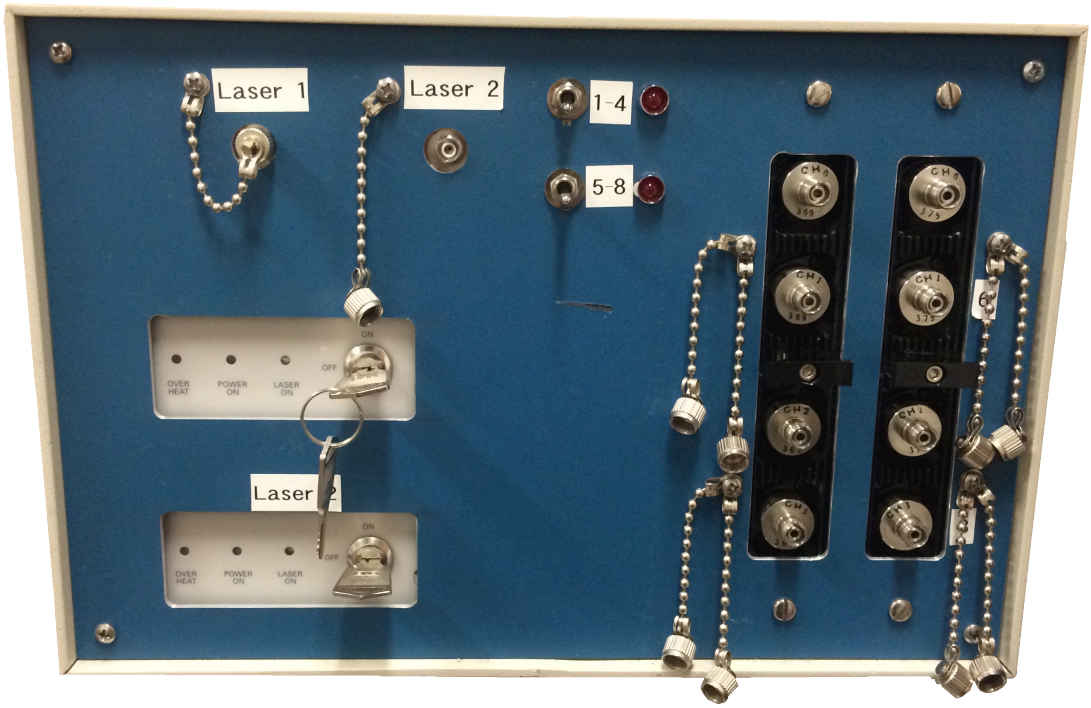

Figure 12: Picture of DCS module used in the work presented in this thesis.

This particular module consists of two long coherence length lasers with optical isolators operating at 785 nm. This wavelength was chosen due to its proximity to the isosbestic point at 810 nm where the absorption spectra of oxy- and deoxy-hemoglobin intersect in the near-infrared. On the detection end, eight single-mode fibers are coupled to 2 4-channel avalanche photon diodes (APDs). The detected signal is then fed into an 8-channel correlator that derives the intensity autocorrelation function based on photon arrival times. Table 3 provides a comprehensive parts list for the components of this 8-channel DCS module.

Table 3: Parts list for an 8-Channel, 2 laser DCS box.

Item	Quantity	Manufacturer/Distributor	Part Number
Long-coherence length lasers with optical isolator	2	Crystalaser	DL785-100-3O
4-Channel APD	2	Pacer	SPCM-AQ4C
4-Channel interface card	1	Pacer	SPCM-AQ4C-IO
8-Channel correlator	1	Correlator.com	Flex05-8ch
+5 V Power supply	1	Murata	SWS50-5
+28 V Power supply	1	Lambda	HSB-28-1.0
+2 V Power supply	1	ASTEC	LPT81
Data Acquisition Module	1	National Instrument	780115-01
Box enclosure	1	Newark	86F936
Lumex Indicator Light	2	Allied Electronics, Inc.	670-1305
Electroswitch Toggle	2	Allied Electronics, Inc.	747-0029
309 Ohm .125W Resistor	2	Allied Electronics, Inc.	70200773
50 Ohm 3W Resistor	5	Allied Electronics, Inc.	70201568

4.4 Validation Studies

DCS has been validated against multiple clinical modalities and in a variety of tissues [48-53]. Table 4 summarizes validation studies that compare relative changes in BFI measured with DCS against various “more” established modalities for measuring

cerebral blood flow (CBF) in humans. I contributed significantly to the data acquisition and interpretation of the validation study published by Buckley et al [48].

Table 4: Summary of validation studies of DCS measurements of changes in BFI in human brain due to a perturbation.

Age	Modality	Perturbation	Correlation Coefficient	Slope	Reference
Infant	ASL-MRI	Hypercapnia	0.7	0.85	[49]
Child	VENC-MRI	Hypercapnia	0.86	0.85-1.03	[48]
Adult	Xenon-CT	Pressors & Hyperventilation	0.73	1.1	[52]

ASL-MRI, arterial spin labeling magnetic resonance imaging; *VENC-MRI,* velocity encoded magnetic resonance imaging; *Xenon-CT*, xenon-enhanced computer tomography.

In addition to the validation studies shown in Table 4, I participated substantially in studies that aimed to validate *absolute* BFI in a subpopulation of the cohort reported in Section 6 (infants with CHD). For this work, which has been published [14], I played an integral role in data acquisition and data interpretation. Specifically, we compared BFI measured with optics to CBF measured in the sagittal sinus with velocity-encoded (VENC) MRI, i.e., VENC-MRI. We observed a significant correlation between BFI measured with optical-DCS and CBF measured with VENC-MRI (R^2=0.25, p=0.01**)** (Figure 13). The BFI in this comparison was calculated by fitting the intensity temporal auto-correlation curve while using values of μ_a and μ_s' measured in each patient by DOS. In following section, I discuss the effect of μ_s' on this validation of BFI, and indicate areas for future work.

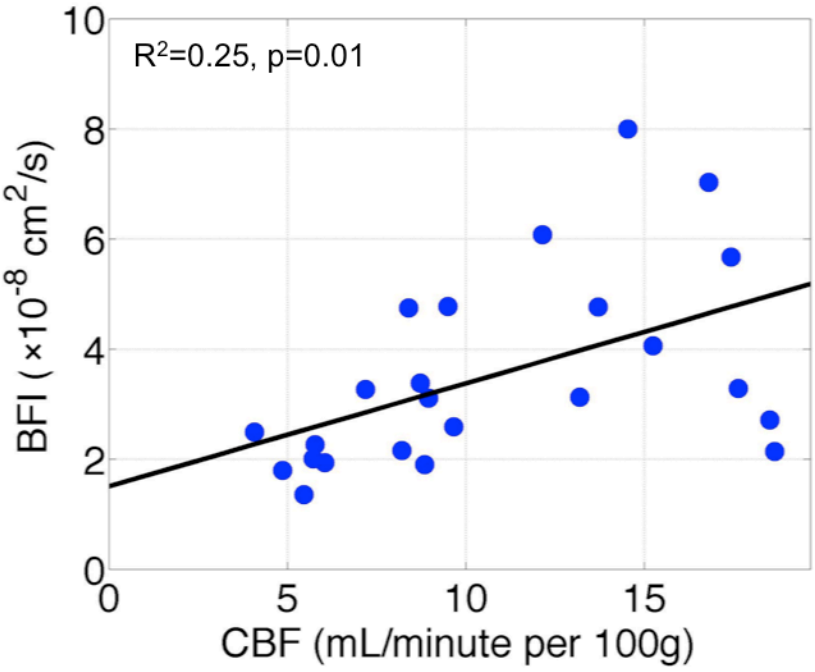

Figure 13: Correlation of BFI measured with optics and CBF measured with VENC-MRI. The black line denotes the line of best fit to the data (R^2=0.25, p=0.01). This work has been published [14].

4.5 Effect of optical properties on BFI

The effect of the values for μ_a and μ_s' in calculations of BFI has been described in reference [11]. One conclusion from that discussion is that the parameter μ_s' has a much greater influence on BFI than μ_a. Therefore, errors in μ_s' have more impact on BFI than errors in μ_a. In Section 6 of this thesis, I will report BFI values for a population of infants with complex congenital heart disease. In this section, I briefly describe the effect of μ_s' in the validation studies of BFI against VENC-MRI within a subset of this patient population [14].

In the previous section, I showed a correlation (R^2=0.25, p=0.01) between BFI measured with DCS and CBF measured with VENC-MRI, i.e., within in a subpopulation of the cohort presented in this thesis [14]. The BFI values used in the comparison were

calculated from the measured intensity temporal auto-correlation curve using each patient's measured μ_s'. BFI also is calculated this way for the results reported in Section 6 of this thesis. Perhaps surprisingly, when we calculated BFI assuming a fixed value μ_s' for all subjects, then the measurements of BFI and CBF exhibit a higher correlation. The value assumed for μ_s' had a significant effect on the slope of the BFI-CBF correlation, but not on the correlation coefficient.

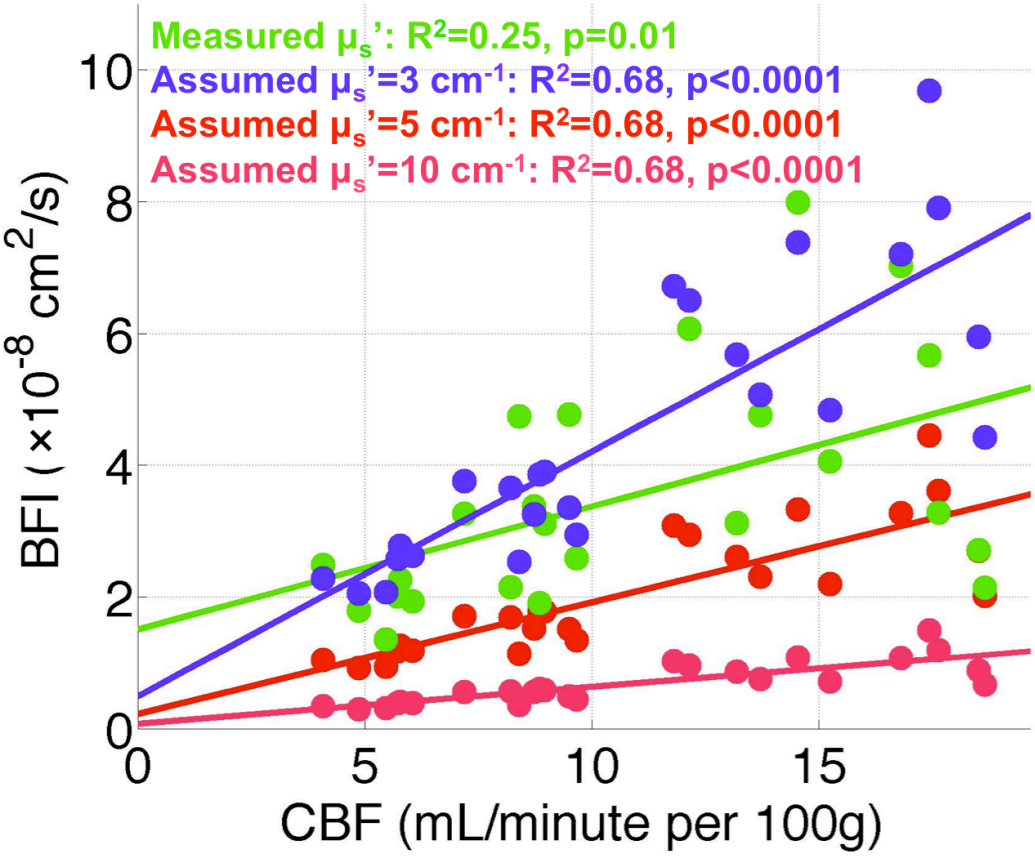

Figure 14: Comparison of BFI calculated using various values of $\boldsymbol{\mu_s'}$ to CBF measured with VENC-MRI. Each set of data has a line of best fit. Interestingly, the correlation between BFI and CBF seems to improve when assumed value of $\boldsymbol{\mu_s'}$ is used across all subjects for calculating BFI.

This observation is puzzling. Random and systematic noise in measured μ_s' must account for this effect. One possible explanation for the improvement of the correlation when assuming a fixed value for μ_s' for the entire population is that DOS is more sensitive to the superficial layers (i.e., the skull and scalp) than DCS, i.e., due to the multiple source-detector separations used for DOS.Further, we have found that our measurements of μ_s' typically had errors larger than 20% in these geometries and with these probes. This issue is deserving of further study; we have not resolved it. Nevertheless, we continue to use measured μ_s' in this thesis.

4.6 Cerebral effects of intravenous adenosine

DCS is a highly useful tool in clinical studies, as it enables non-invasive quantification of CBF and can be used at the patient's bedside and other operating/imaging suites throughout the hospital. In this section, I describe a clinical investigation that I conducted using DCS in patients undergoing cardiac imaging in a magnetic resonance (MR) suite. This study was performed to understand the effects on cerebral blood flow of adenosine, a drug given as part of clinical protocol for cardiac stress MRIs.

4.6.1 Introduction

Adenosine is a nucleoside that is present in the body and plays an important role in the regulation of vascular tone and thus the regulation of blood flow [54]. When given intravenously, adenosine has a vasodilatory effect on the coronary arteries. Because of this, adenosine infusions are often given in cardiac stress tests to evaluate myocardial perfusion. Specifically, patients complaining of chest pain, or children whose coronary

arteries have been manipulated due to prior cardiac surgery, undergo an adenosine stress cardiac MRI (ACMRI) in order to measure myocardial perfusion during resting state and during stress induced by the adenosine infusion.

While the effect of adenosine on the coronary arteries are well known, the cerebral effects of adenosine are poorly understood. There have been a few experimental studies on the effects of adenosine on cerebral hemodynamics, but these studies have conflicting results [55-58]. Sollevi et al. observed an increase in CBF measured with positron emission tomography (PET) in normoventilated, anesthetized human subjects upon receiving an infusion of adenosine [58]. Increases in CBF due to adenosine have also been observed in rabbits and baboons [55, 56]. However, Hussain et al. observed no change in CBF due to adenosine in awake humans [57], and others have reported that CBF does not change due to adenosine in cats and dogs [56].

Understanding the effects of intravenous adenosine on the cerebral vasculature is important for understanding the role of adenosine in regulating cerebral blood flow. In this study, I used DCS and DOS to non-invasively quantify changes in cerebral blood flow and oxygenation due to adenosine infusions during these cardiac stress tests.

4.6.2 Methods

Study Protocol

This study was approved by the Children's Hospital of Philadelphia Institutional Review Board. All patients undergoing an adenosine stress cardiac MRI (ACMRI) were evaluated for study inclusion. Patients were either induced under general anesthesia or stayed awake for the ACMRI. The subset of patients placed under general anesthesia

were induced with Sevoflorane. After induction of anesthesia (when used) and before the cardiac MRI, baseline DOS measurements of μ_a and μ_s' were acquired on both sides of the forehead. Once the patient is placed inside of the MRI scanner, an optical probe with one source-detector separation (see Section 2.3) was placed on the forehead and left on for the duration of the ACMRI.[2] All ACMRI were performed on the same scanner; Siemens Avanto 1.5T (Siemens Medical Systems, Malvern, NJ, USA). The duration of the ACMRI is approximately 60 minutes, during which MRI scans of the heart are acquired for baseline and post-infusion conditions. After the baseline scans are acquired, a cardiac anesthesiologist administers the intravenous adenosine infusion at a dosage of 140 micrograms/kg/min over 6 minutes.

Vital sign data were captured from clinical monitors using the Moberg CNS 1000 monitor (Moberg, Ambler, PA, USA). Optical data was acquired continuously throughout the duration of the ACMRI at a frame rate of approximately 0.3 Hz. Changes in μ_a were calculated from the baseline values taken before the MRI (see Section 2.3). The relative change in CBF (rCBF) due to the adenosine infusion was quantified by comparing an average BFI during the pre-infusion period to an average at the end of the 6-minute infusion period via the following formula:

$$rCBF = \frac{\langle BFI \rangle_{\text{During}}}{\langle BFI \rangle_{\text{Pre}}} \times 100\%. \tag{4.10}$$

[2] The use of a single source-detector separation was due to the lack of availability of an MR compatible probe with multiple source-detector separations. The probe with multiple source-detector separations used for baseline measurements was not MR compatible, and the fibers were not long enough to extend from the instrument which is placed in an adjoining control room to the patient in the scanner.

Here, ⟨ ⟩ denotes an average over 2 minutes either immediately before the adenosine infusion or during the last 2 minutes of the infusion (Figure 15). Similarly, changes in the total hemoglobin concentration THC, heart rate (HR), and mean arterial pressure (MAP) were calculated from the following formulas:

$$\Delta THC = \langle THC \rangle_{\text{During}} - \langle THC \rangle_{\text{Pre}}, \tag{4.11}$$

$$\Delta HR = \langle HR \rangle_{\text{During}} - \langle HR \rangle_{\text{Pre}}. \tag{4.12}$$

$$\Delta MAP = \langle MAP \rangle_{\text{During}} - \langle MAP \rangle_{\text{Pre}}. \tag{4.13}$$

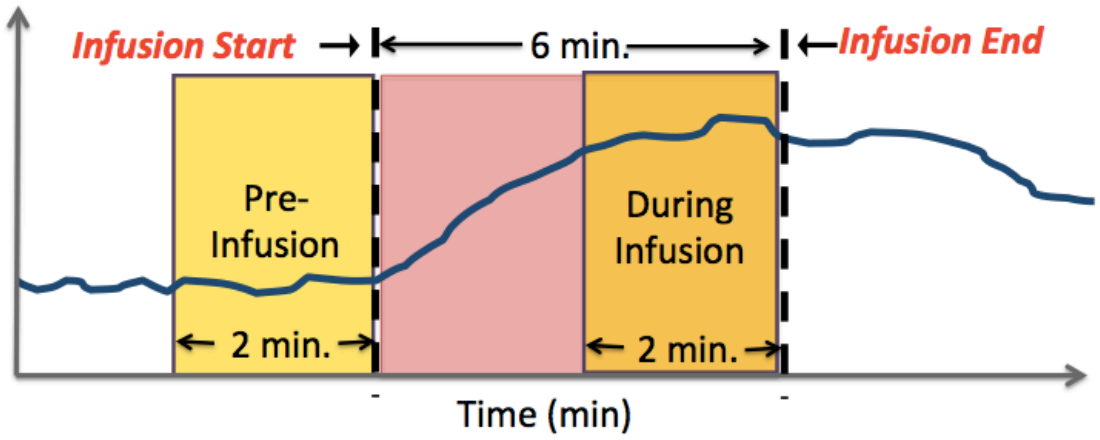

Figure 15: Schematic of study protocol. Optics and vitals data are recorded continuously throughout the duration of the MRI. The adenosine infusion lasts 6 minutes. Variables of interest are averaged over a 2-minute pre-infusion period and compared to an average during the last 2 minutes of the infusion.

4.6.3 Results

A total of N=20 patients were studied, and patient demographics are summarized in Table 5. Patients were predominately male, and the subgroup of patients who were

anesthetized for the ACMRI were significantly younger than those who were awake ($p<0.01$).

Table 5: Summary of demographic data for subjects studied undergoing an ACMR.

Group	N	Female (n)	Age (years)	Weight (kg)
Awake	11	0	16.0±2.9	70.3 ±15.2
Anesthetized	9	2	9.1±3.3	36.9±20.6
All	**20**	**2**	**12.9±3.1**	**55.3±17.6**

We observed a significant ($p=0.005$) difference in the change of CBF due to adenosine between the group of patients who were anesthetized and those who were awake for the ACMRI (Figure 16). Specifically, subjects who were awake for the ACMRI, had, on average, an increase in CBF due to adenosine, whereas the subjects who were anesthetized for the ACMRI had, on average, a decrease in CBF due to adenosine. We did not observe a significant difference between these two groups in the change in THC due to adenosine (Figure 17). Both groups had an increase in HR, but the group of subjects who were awake for the ACMRI had a significantly greater increase in HR due to adenosine (Figure 18). Additionally, the group of subjects who were anesthetized had a decrease in MAP whereas the group of subjects who were awake had, on average, no change in MAP due to adenosine.

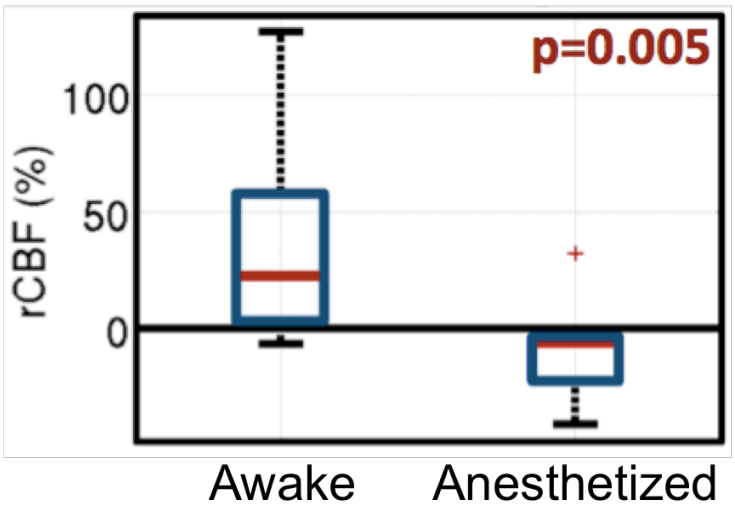

Figure 16: Changes in CBF due to an adenosine infusion in patients who are awake (N=11) or anesthetized (N=9) during the infusion. Patients who were awake during induction had a significant increase in CBF. The red line denotes the median value; the blue square extends to the 25th and 75th percentiles; the whiskers extend to the most extreme data points that are not outliers; and the outliers are plotted as individual points.

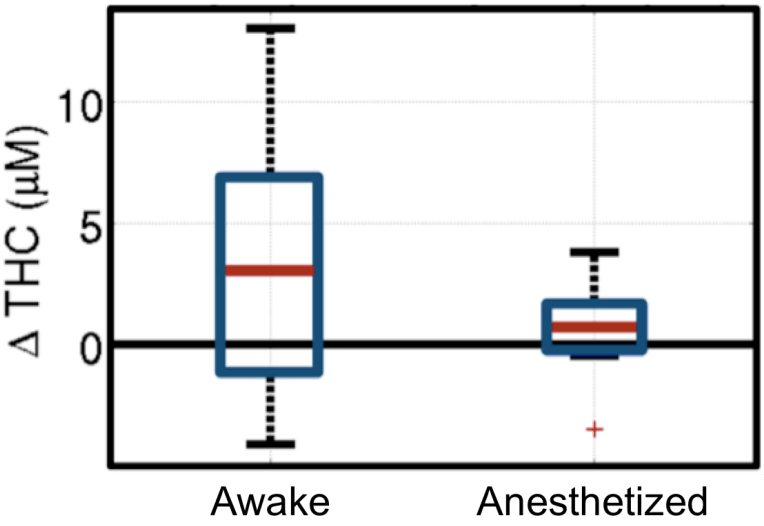

Figure 17: Changes in THC due to an adenosine infusion in patients who are awake (N=11) or anesthetized (N=9) during the infusion. There was no observed significant difference in change in THC due to adenosine between the two subgroups. The red line denotes the median value; the blue square extends to the 25th and 75th percentiles; the whiskers extend to the most extreme data points that are not outliers; and the outliers are plotted as individual points.

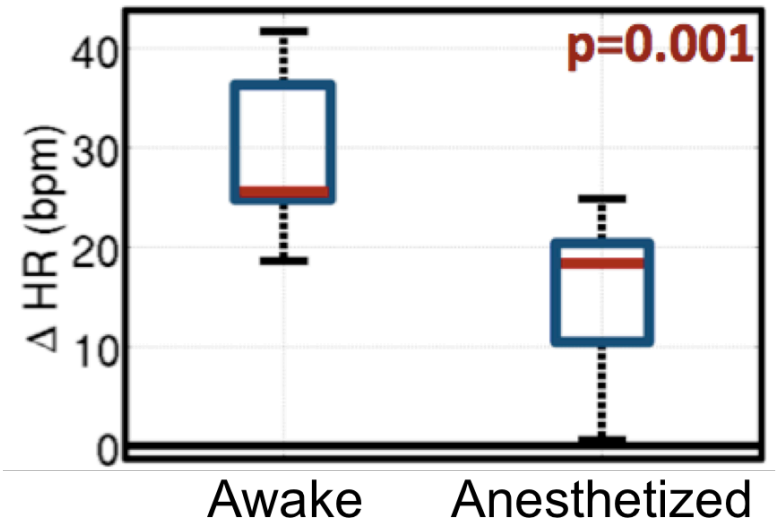

Figure 18: Changes in HR due to an adenosine infusion in patients who are awake (N=11) or anesthetized (N=9) during the infusion. Patients who were awake during induction had a significantly larger increase in HR due to adenosine. The red line denotes the median value; the blue square extends to the 25th and 75th percentiles; the whiskers extend to the most extreme data points that are not outliers; and the outliers are plotted as individual points.

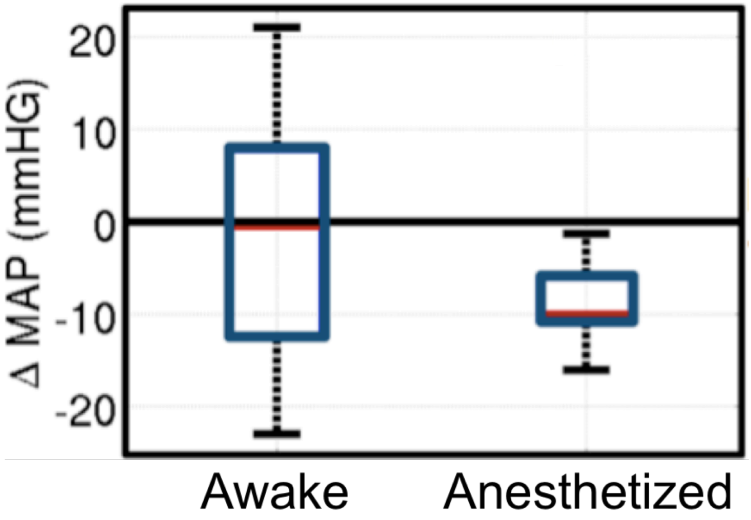

Figure 19: Changes in MAP due to an adenosine infusion in patients who are awake (N=11) or anesthetized (N=9) during the infusion. Patients who were awake during induction had on average no change in MAP, whereas patients who were anesthetized had a decrease in MAP due to adenosine. The red line denotes the median value; the blue square extends to the 25th and 75th percentiles; the whiskers extend to the most extreme data points that are not outliers; and the outliers are plotted as individual points.

4.6.4 Discussion

We observed that the effect of an intravenous adenosine infusion on CBF depends on whether or not the patient is anesthetized. This observation may explain some of the discrepancies reported seen in the literature. Additionally, we do not see an average increase in THC due to adenosine in either group. Since THC is related to cerebral blood volume (CBV), which should increase when there is vasodilation, the results herein suggests that perhaps adenosine does not have a vasodilatory effect on the cerebral vasculature. Thus, the reason for the increase in CBF observed in the group of awake subjects could be due to a reflex of the sympathetic nervous system. That is, the increase in CBF in the awake patients may be possibly due to a "fight-or-flight" response induced from the patient experiencing the drop in blood pressure caused by adenosine. Supporting this hypothesis is the difference in the change in heart rate due to adenosine seen between these two groups. The group of patients that were awake during the adenosine infusion had, on average, an increase in heart rate due to the infusion, whereas patients who were anesthetized did not. This suggests that the increase in heart rate is not due to the drug alone and may be influenced by the patient's awareness of the drug and thus caused by a sympathetic response.

Since CBF was observed to decrease due to adenosine in the subset of patients who were anesthetized, one could conclude that the primary effect of adenosine is actually to decrease CBF. Further investigations, specifically into the interaction with anesthetics, are needed to definitively elucidate the effect of adenosine on cerebral vasculature.

4.6.5 Conclusion

We observed that the effect of adenosine on cerebral blood flow depends on whether or not the patient is awake or anesthetized during the infusion. Specifically, the adenosine infusion caused an increase in cerebral blood flow in patients when they were awake and a decrease in cerebral blood flow in anesthetized patients. This result suggests that the increase in CBF observed in awake patients is due to a sympathetic response and not due to vasodilation of the cerebral vasculature driven by adenosine. Although the evidence herein suggests that the primary effect of adenosine on cerebral vasculature is a decrease in CBF, further investigation is necessary to understand the role of drug interactions between adenosine and the anesthetics.

5 Diffuse Optical Measurements of Cerebral Oxygen Metabolism

While DOS and DCS are both valuable tools on their own, together they can provide even greater insight into the health or impairment of the cerebral vasculature. In this chapter, I first describe the hybrid DOS/DCS instrument that I assembled and troubleshot for use in the work presented in this thesis. I then describe the theory behind using both of these techniques to measure cerebral oxygen metabolism. I also describe work that I have done in validating measurements of cerebral oxygen metabolism in infants with CHD. Finally, I demonstrate the clinical usefulness of a hybrid DOS/DCS device by describing a clinical study in which I use this hybrid instrument to measure cerebral oxygen metabolism in children with pulmonary hypertension.

5.1 Hybrid DOS/DCS Instrumentation

I combined the DOS module (Imagent, ISS Inc., Champagin, IL, see Section 2.4) and the DCS module (See Section 4.3) onto one portable cart and used them in tandem. Figure 20 shows the hybrid device that was used for all results reported herein.[3] One computer was used to control both devices. However, the devices were controlled via two separate user interfaces. The DCS module is operated with an in-house developed Labview program. This program controls a data acquisition (DAQ) module, which controls the laser's power source. The DOS module is controlled by a data acquisition software developed by ISS

[3] Two similar devices were used interchangeably. There were no practical differences between these two devices that affect any of the work presented herein.

called Boxy. This software allows for real-time analysis of μ_a and μ_s' to ensure adequate data quality.

Figure 20: Hybrid DOS/DCS module used for the work presented in this thesis.

5.2 Calculation of Cerebral Metabolic Rate of Oxygen

In addition to the advantage of using DOS to measure the optical properties to improve the fitting and thus accuracy of our DCS measurements, valuable information is obtained when measuring CBF and StO_2 concurrently, because one can then quantify the cerebral metabolic rate of oxygen ($CMRO_2$). $CMRO_2$ can be calculated using Fick's equation:

$$CMRO_2 = OEF \times CBF \times CaO_2. \tag{5.1}$$

Here, OEF is again oxygen extraction fraction (see Section 2.5), CBF is cerebral blood flow, and CaO_2 the arterial oxygen concentration which can be calculated using the formula:

$$CaO_2 = 1.39 \times SaO_2 \times [Hgb] + 0.003 \times PaO_2. \tag{5.2}$$

Here, 1.39 is the amount of oxygen in milliliters that a fully saturated gram of hemoglobin can carry; PaO_2 is the partial pressure of oxygen in arterial blood, which is measured from an arterial blood gas and has units of mmHg; and again SaO_2 is the arterial oxygen saturation and $[Hgb]$ is the hemoglobin concentration of arterial blood in units of grams per deciliter. CaO_2 has units of milliliters of O_2 per deciliter of blood. Equation 5.1 yields $CMRO_2$ in units of milliliters of O_2 per minute per 100 g of tissue.

Because DCS yields a BFI in units of cm^2/s, instead of CBF in traditional units of (mL/min/100 g of tissue), the quantification of oxygen metabolism reported in this thesis is an index of $CMRO_2$ denoted herein as $CMRO_{2,i}$. $CMRO_{2,i}$ has units of $mL/dL \times cm^2/s$ and can be calculated form the formula:

$$CMRO_{2,i} = OEF \times BFI \times CaO_2. \tag{5.3}$$

Recall from Section 2.5, $OEF = \frac{SaO_2 - SvO_2}{SaO_2}$. If DOS data is acquired at a fast enough rate and the SNR is sufficient, then SvO_2 can be calculated from the optical signal detected by DOS (see Chapter 3). Thus, the resulting formula for $CMRO_{2,i}$ is:

$$CMRO_{2,i} = \frac{SaO_2 - SvO_2{}^{DOS}}{SaO_2} \times BFI \times CaO_2. \tag{5.4}$$

When $SvO_2{}^{DOS}$ cannot be determined, $CMRO_{2,i}$ can be calculated from the following equation:

$$CMRO_{2,i} = \frac{1}{\gamma}\frac{SaO_2 - StO_2}{SaO_2} \times BFI \times CaO_2, \tag{5.5}$$

where, again, γ is the percentage of blood in the venous compartment and assumed in this work to be $\gamma = 0.75$. This assumption may be problematic, since γ may vary significantly from patient to patient or even over time for individual patients. For the majority of the work presented in this thesis, $CMRO_{2,i}$ is calculated from this equation.

5.3 Validation Studies

In the same study discussed in Section 4.5, we validated $CMRO_{2,i}$ measured by optics against $CMRO_2$ measured by MRI in a subset of the population reported in this thesis of infants with congenital heart disease [14]. In this study, $CMRO_{2,i}$ from optics was calculated from Equation 5.5. $CMRO_2$ measured by MRI was calculated using CBF and SvO_2 measured in the superior sagittal sinus via VENC-MRI and MR susceptometry, respectively. Arterial blood gases were used to calculate CaO_2 and SaO_2, and thus the same values were used for the calculations of both $CMRO_{2,i}$ and $CMRO_2$. We observe a significant correlation between the two methods of measuring oxygen metabolism ($R^2 = 0.31;\ p = 0.01$).

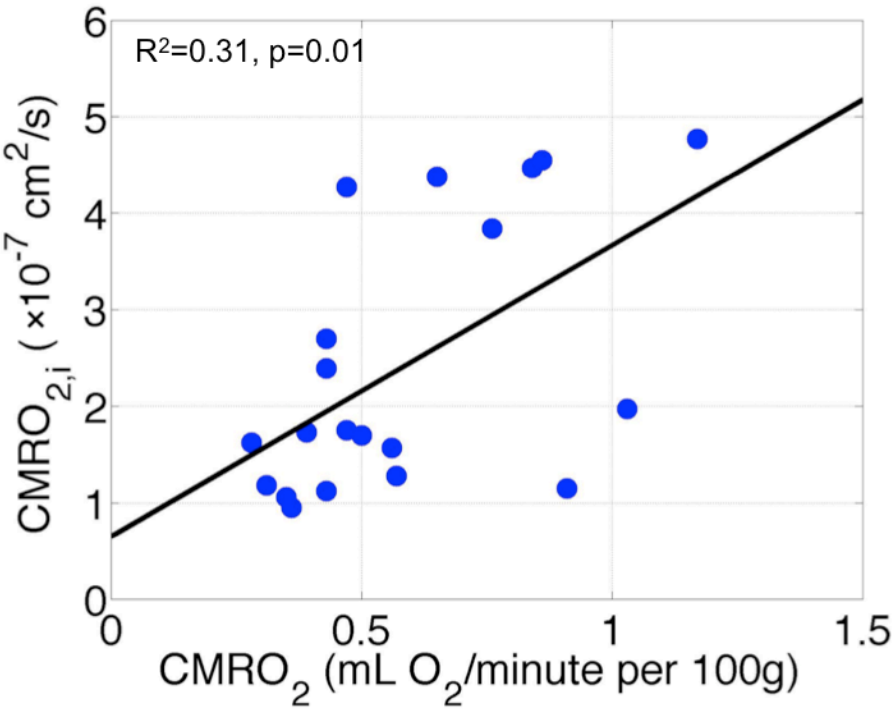

Figure 21: Correlation of $CMRO_{2,i}$ measured with optics and $CMRO_2$ measured with MRI. The black line denotes the line of best fit to the data (R^2=0.31, p=0.01).

However, as stated in Section 4.5, BFI depends significantly on μ_s'. Since BFI is used for calculating $CMRO_{2,i}$, choosing to use the measured value of μ_s' or an assumed value will also affect the validation of $CMRO_{2,i}$. When using BFI values calculated from assuming a single value of μ_s' for all patients, the correlation and significance improve ($R^2 = 0.69;\ p < 0.0001$) (Figure 22). However, the values of $CMRO_{2,i}$ reported in Section 6 of this thesis were derived from BFI that is calculated using the individual subject's measured μ_s'.

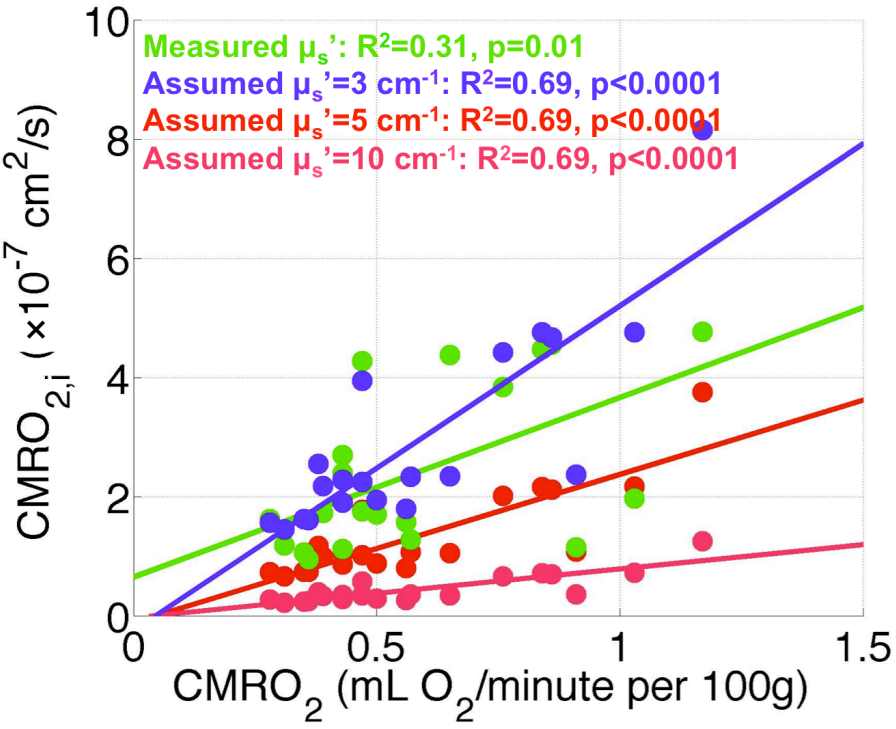

Figure 22: Comparison of $CMRO_{2,i}$ calculated using various values of $\boldsymbol{\mu_s'}$ to $CMRO_2$ measured with MRI. Each set of data has a line of best fit. The correlation between $CMRO_{2,i}$ and $CMRO_2$ improves when an assumed value of $\boldsymbol{\mu_s'}$ is used for calculating BFI.

5.4 Cerebral hemodynamics in children with pulmonary hypertension

5.4.1 Introduction

Pulmonary hypertension (PH) is a rare condition in which patients exhibit a reduction in pulmonary blood flow and an inability of the pulmonary vasculature to dilate. Currently, the severity of PH and the efficacy of treatment is assessed via invasive cardiac catheterization. This procedure evaluates pulmonary and systemic vascular resistance and blood flow during a baseline condition and during two conditions that are chosen to challenge the vaso-reactivity of the vessels in the lungs.

In the first condition, the inspired air is augmented with 40 parts per million inhaled nitric oxide (iNO), which acts as a local vasodialator of the pulmonary arterioles. iNO is not believed to have any significant extra-pulmonary effects due to its rapid degradation upon inhalation. There have been reports of iNO therapy mitigating some neurological complications, such as cerebral palsy, in premature neonates [59, 60], suggesting that iNO could have effects on cerebral vasculature under certain conditions.

In the second condition, while maintaining the iNO concentration of 40ppm, the inspired room air is replaced by 100% oxygen (O_2), which also acts as a pulmonary vasodilator. However, 100% O_2 is non-selective and has cerebral and systemic effects. Specifically, hyperoxia causes cerebral and systemic vasoconstriction in normal physiology and thus results in a decrease in CBF by approximately 10% [61, 62]. The goal of this investigation was to begin to explore the complex relationship between cerebral protective functions and diminishing lung function through quantification of cerebral metabolic rate of oxygen ($CMRO_2$) in patients with pulmonary hypertension during these conditions.

5.4.2 Methods

Study Protocol

This study was approved by the Children's Hospital of Philadelphia Institutional Review Board. All patients undergoing the cardiac catheterization protocol for pediatric pulmonary hypertension were evaluated for study inclusion. After induction of anesthesia with Sevoflurane, we placed the optical probe on one side of the forehead and secured with an elastic bandage for the duration of the cardiac catheterization. The

optical probe housed fibers for both DOS and DCS and had multiple source-detector separations for DOS (Figure 23). After this probe was secured on the patient's forehead, the cardiac catheterization commenced, starting with a baseline (room air) condition. A general timeline of the study is shown in Figure 24.

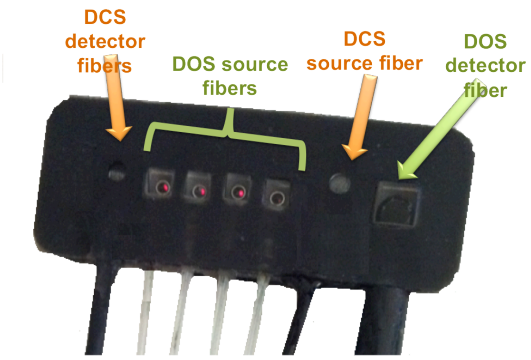

Figure 23: Picture of optical probe that combines optical fibers for DOS and DCS.

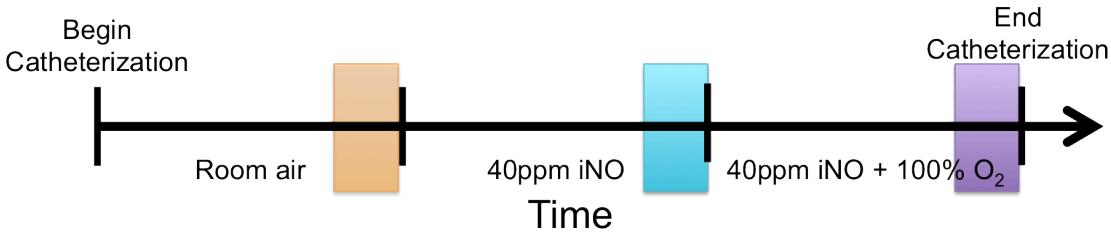

Figure 24: Timeline of study. The entire catheterization lasts approximately 90 minutes. The colored regions denote the times over which the optics data were averaged to calculate the effects of iNO and iNO+100% O_2.

Data Analysis

Vital sign data were captured from clinical monitors using the Moberg CNS 1000 monitor (Moberg, Ambler, PA, USA). Optical data was acquired continuously

throughout the duration of the cardiac catheterization at a frame rate of approximately 0.3 Hz. μ_a, μ_s' and BFI were quantified every frame (see Sections 2.2 and 4.2). The relative change in CBF (rCBF) due to 40ppm iNO was quantified by comparing an average BFI during the baseline room-air period to an average at the end of the 40ppm iNO condition from the following formula:

$$rCBF = \frac{\langle BFI \rangle_{\text{During}}}{\langle BFI \rangle_{\text{Pre}}} \times 100\%. \tag{5.6}$$

Here, $\langle BFI \rangle_{\text{Pre}}$ denotes an average of BFI over 2 minutes immediately before the iNO was turned on and $\langle BFI \rangle_{\text{During}}$ denotes an average of BFI over 2 minutes at the end of the iNO period (i.e., immediately before the addition of 100% O_2). The change in CBF due to 100% O_2 was also calculated using Equation 5.6, where $\langle BFI \rangle_{\text{Pre}}$ is the average BFI over 2 minutes immediately before the O_2 was increased from room air to 100% and $\langle BFI \rangle_{\text{During}}$ is the average BFI over 2 minutes immediately before the end of the catheterization.

Similarly, changes in StO_2 due to iNO and 100% O_2 were calculated from the following formula:

$$\Delta StO_2 = \langle StO_2 \rangle_{\text{During}} - \langle StO_2 \rangle_{\text{Pre}}. \tag{5.7}$$

Here, $\langle\ \rangle_{\text{Pre}}$ and $\langle\ \rangle_{\text{During}}$ have the same meaning as defined for Equation 5.6. Relative changes in $CMRO_2$ ($rCMRO_2$) due to iNO and 100% O_2 were calculated from the following formula:

$$rCMRO_2 = rCBF \times rOEF \times rCaO_2, \tag{5.8}$$

where $rCBF$ is defined from Equation 5.6, $rOEF = \frac{\langle OEF \rangle_{\text{During}}}{\langle OEF \rangle_{\text{Pre}}}$, and $rCaO_2 = \frac{\langle CaO_2 \rangle_{\text{During}}}{\langle CaO_2 \rangle_{\text{Pre}}}$.

Again, $\langle\,\rangle_{Pre}$ and $\langle\,\rangle_{During}$ have the same meaning as defined for Equation 5.6

5.4.3 Results

A total 29 patients have been studied so far. The average age was 6.2±5.0 years and 16/29 of the patients were female. We observed a significant increase in StO_2 due to the change from 40 ppm iNO to 40ppm iNO + 100% O_2 and a trend towards decreasing StO_2 due to the change from room air to 40ppm iNO (Figure 25). We observed opposite trends in OEF (Figure 27). We observed no change in CBF due to either condition (Figure 26). Likewise, we observed no change in CaO_2 (Figure 27). While we observed no change in $CMRO_2$ due to the change from room air to 40ppm iNO, we observe a trend towards decreasing $CMRO_2$ due to the change from 40 ppm iNO to 40ppm iNO to 100% O_2 (Figure 27).

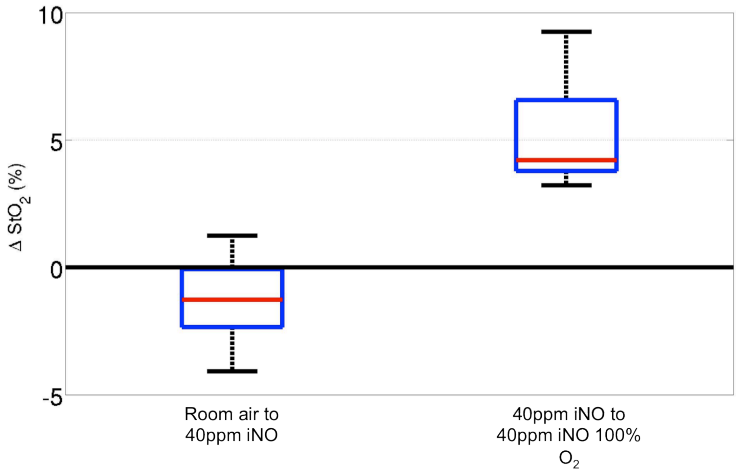

Figure 25: Changes in StO_2 due to 40ppm iNO (left) and due to the addition of 100% O_2 (right). StO_2 increases due to the addition of 100% O_2. The red line denotes the median value; the blue square extends to the 25th and 75th percentiles; the whiskers extend to the most extreme data points that are not outliers; and the outliers are plotted as individual points.

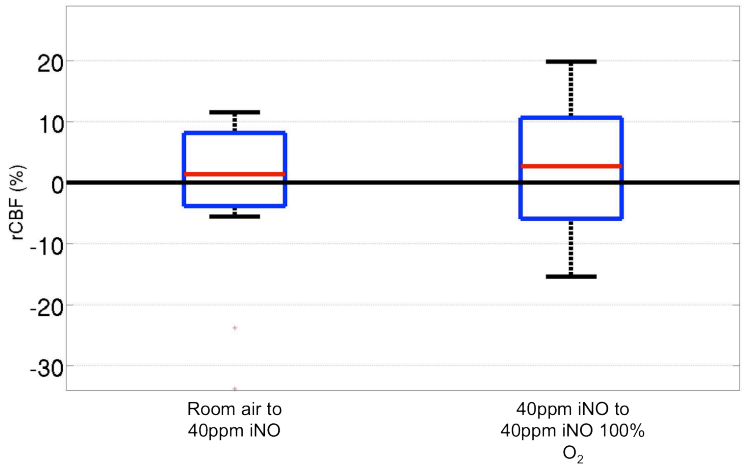

Figure 26: Relative changes in CBF due to 40ppm iNO (left) and due to the addition of 100% O_2 (right). We do not observe any change in CBF due to iNO or 100% O_2. The red line denotes the median value; the blue square extends to the 25th and 75th percentiles; the whiskers extend to the most extreme data points that are not outliers; and the outliers are plotted as individual points.

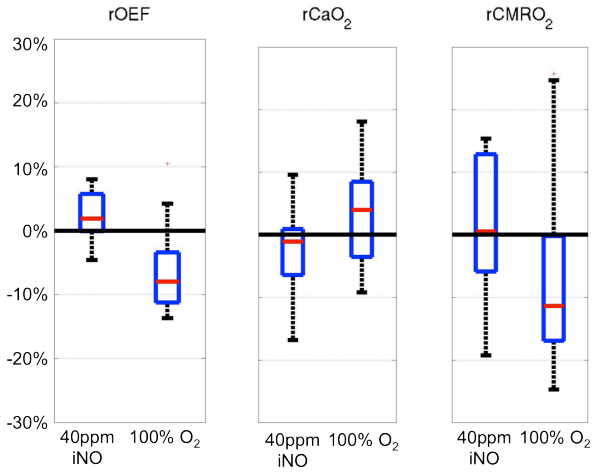

Figure 27: Relative changes in OEF (left), CaO_2 (center), and $CMRO_2$ (right) due to 40ppm iNO (left box) and due to the addition of 100% O_2 (right box). We observe a trend of decreasing OEF and $CMRO_2$ due to the addition of 100% O_2. The red line denotes the median value; the blue square extends to the 25th and 75th percentiles; the whiskers extend to the most extreme data points that are not outliers; and the outliers are plotted as individual points.

5.4.4 Discussion

The results of this study are still being vetted. However, these preliminary results suggest that iNO and 100% O_2 have a normal effect on $CMRO_2$ in children with pulmonary hypertension. In a study of healthy adults, Xu et al. observed that hyperoxia caused an increase in StO_2, no change in CBF, and a slight decrease in $CMRO_2$, similar to the results reported here [63]. Additionally, we did not observe any cerebral effects of iNO, which is expected for healthy cerebral vasculature. However, this population of children with PH was highly heterogeneous with respect to severity of the disease and medications being used to treat the disease. More patients need to be recruited to be able to separate out any effect that disease severity or treatment plans may have on these results.

5.4.5 Conclusion

Hybrid DOS/DCS is a useful tool for non-invasively quantifying $CMRO_2$ at a patient's bedside, or in this case in a catheterization suite. We have shown that these measurements are possible in this population, for which $CMRO_2$ had not been previously measured. These initial results suggest that the cerebral responses to these clinical interventions and perturbations of the pulmonary vasculature may be normal and similar to those seen in healthy adults.

6 Investigating risks for brain injury in infants with critical CHD

In this chapter, I describe a clinical investigation using DOS and DCS to determine the risk factors for brain injury in infants with CHD. The results in Section 6.4.2 have recently been submitted for publication [16], and the results in Sections 6.4.1 and 6.4.3 are currently being prepared for publication.

6.1 Introduction

Approximately 30,000 children each year are born in the United States with congenital heart disease (CHD). Nearly one third of these CHD patients require cardiac surgery in their first few months of life [1]. With the improved survival from these early surgeries, the majority of these patients are now reaching school age [64], the focus of research has shifted to addressing the neurodevelopment difficulties seen among these survivors. Nearly 50% of the school-age survivors exhibit some neurobehavioral symptoms, such as inattention, hyperactivity, and impaired executive function [2, 65, 66].

Neonatal imaging and neuropathologic studies of patients with complex CHD undergoing infant surgical intervention have revealed a high prevalence of periventricular leukomalacia (PVL) [7]. PVL is a specific form of hypoxic-ischemic white matter injury that commonly occurs in a vascular watershed zone near the lateral ventricles (Figure 28); it is most often observed in preterm neonates who have neurodevelopmental outcomes remarkably similar to those of term patients with CHD.

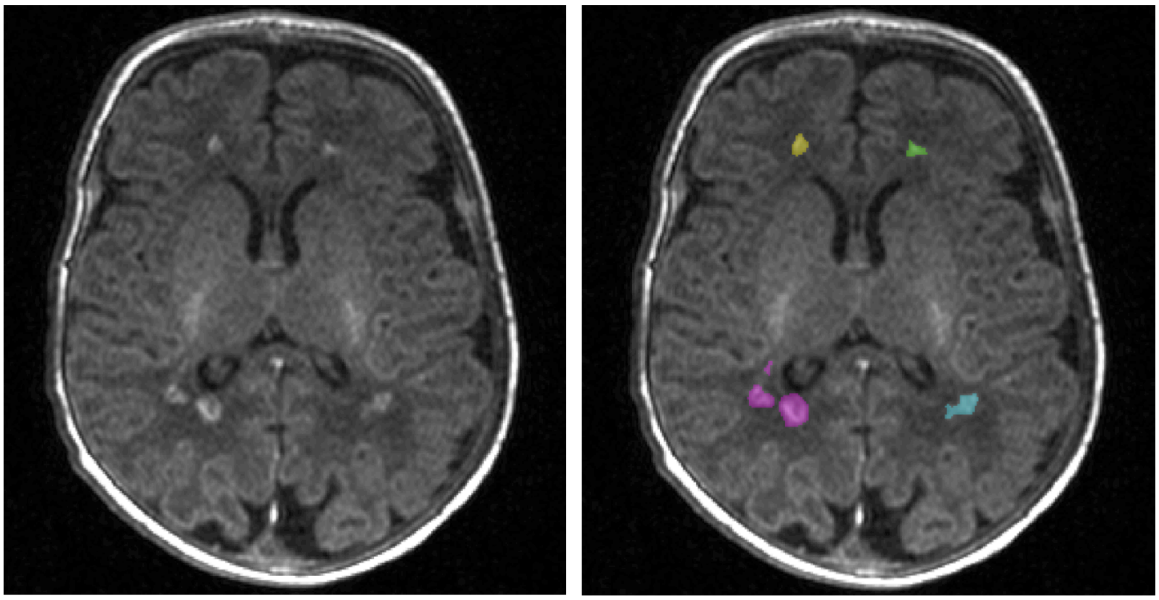

Figure 28: Example of MR image depicting an infant brain with PVL. (Left) Sample T1-weighted MR image of infant brain. (Right) The same image, with the results of a manual segmentation of PVL volumes shown in color.

To date, clinical investigations in CHD neonates have focused on identifying the pre-, peri-, and post-surgical risk factors linked to PVL in order to mitigate or prevent this injury, but uncertainties about its exact cause and timing remain [67-69]. These previous studies have identified possible risk factors for this injury such as abnormal or delayed brain maturation, duration of deep hypothermic circulatory arrest during surgery, and post-operative cerebral oxygenation [9, 67, 70]. However, most of these studies have been carried out in mixed cohorts. In this chapter, I discuss the results from an investigation of a large cohort of neonates with CHD, allowing me to focus on risk factors specific to individual diagnoses. Utilizing diffuse optical and diffuse correlation spectroscopies (DOS and DCS, respectively) for non-invasive bedside quantification of pre- and post-operative cerebral hemodynamics [18, 71], I explore the relationship of

these parameters and other pre-operative, operative, and post-operative variables to the risk of developing PVL.

6.1.1 Physiology of a healthy heart

In order to understand the significance of the impaired physiology of either HLHS or TGA, one must first understand the anatomy of the healthy heart.

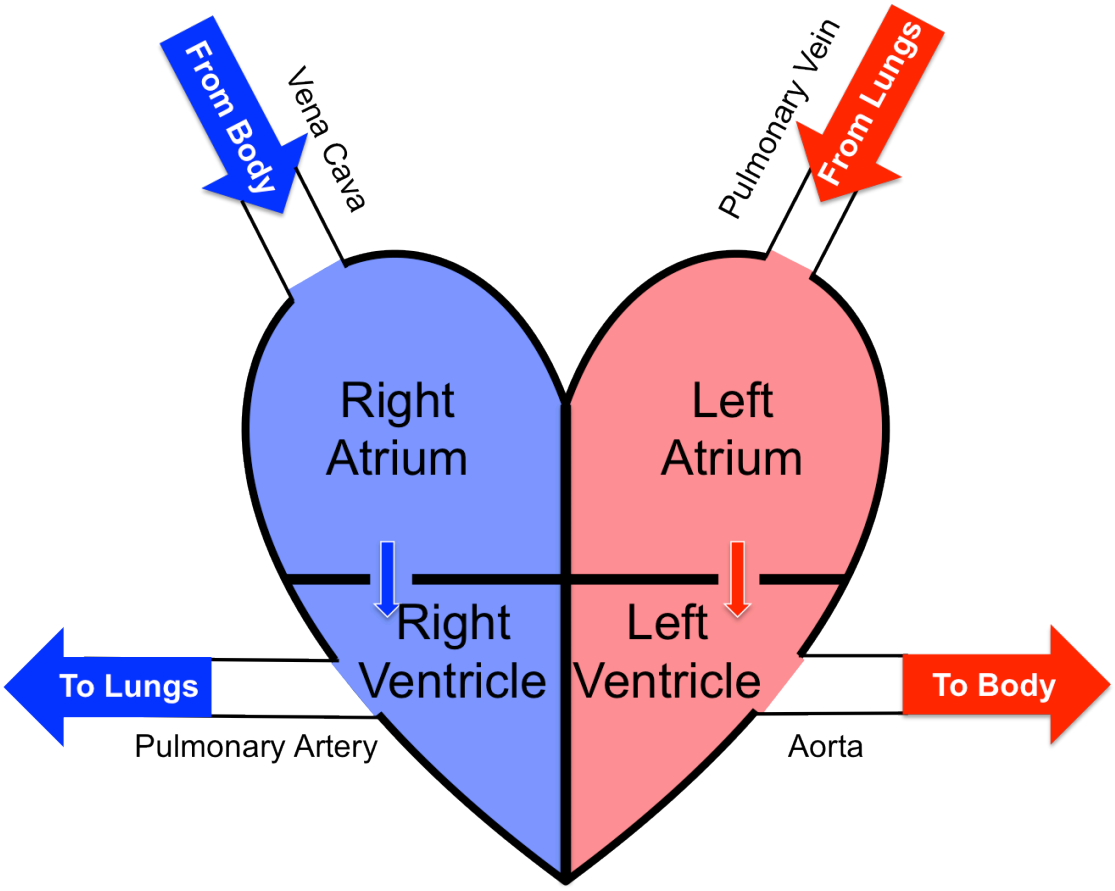

Figure 29: Schematic diagram of a healthy heart.

A normal heart has four chambers: the left ventricle, right ventricle, left atrium and right atrium (Figure 29). Oxygen-poor blood from the body enters the right atrium via the superior and inferior vena cava. From there it travels to the right ventricle, through the

tricuspid valve and then, via the pulmonary valve and artery, into the lungs to become oxygenated. From the lungs, it reenters the heart by traveling through the pulmonary veins and into the left atrium. From the left atrium, the blood travels through the mitral valve into the ascending aorta to deliver oxygenated blood to the systemic circulation, including the brain.

6.1.2 Hypoplastic Left Heart Syndrome

Description of defect

Hypoplastic left heart syndrome (HLHS) is one of the most severe and common critical CHD, making up approximately 9% of critical CHD cases [72]. In this disorder, the left ventricle is critically underdeveloped by a lack of blood flow through either a maldeveloped mitral or aortic valve. Therefore, the right ventricle, which is normally responsible for pumping deoxygenated blood to the lungs, must pump blood to the body and brain as well as the lungs. Blood gets to the systemic circulation via the ductus arteriosis, a developmental artery that connects the common pulmonary artery to the descending aorta. At birth, the ductus arteriosis receives signal to close as a result of infant lungs filling with air for the first time. A medication, called prostaglandin, is given to the baby to hold the ductus arteriosis open. Even with this medication, if left untreated, HLHS is fatal within the first week or two of life. Palliative cardiac surgery is performed usually in 3 stages to treat HLHS by transforming the right ventricle into the systemic ventricle (left ventricle equivalent) and allow the lungs to receive blood from the vena caval system passively (i.e., without going through the heart). During the first

week of life, neonates with HLHS undergo the first stage, the Norwood procedure [72]. All infants with HLHS described in this thesis undergo this operation.

Previous findings on neurodevelopmental outcome

As described in Section 1.2, there are significant neurodevelopmental symptoms that are associated with HLHS. Mahle et al. focused specifically on this cohort, and through a questionnaire filled out by parents, found that approximately 1/3 of children with HLHS were receiving some form of special education [4]. This study also found that median IQ was 86 (below average), and that 18% of patients had mental retardation (defined as an IQ < 70). Believed to be the underlying cause of these symptoms is the high prevalence of PVL seen in this cohort [7].

As seen in this cohort, as well as in previous studies of infants with HLHS, the majority of PVL seen in this cohort is on post-operative MRI scans (see Section 6.4) [16, 70, 73]. Work has been done to identify the risk factors for PVL, however most of this work has been mostly carried out in mixed populations of neonates with various CHDs (including HLHS) and has not been verified in homogenous populations of infants with HLHS [9, 67]. Andropoulus et al. reported brain maturation to be the primary risk for both pre- and post-operative PVL in a mixed cohort of neonates undergoing cardiac surgery with hypothermic cardiopulmonary bypass for 60 minutes or greater [67]. Beca et al. reported duration of DHCA and brain maturation to be significantly associated with post-operative PVL in a mixed cohort of infants undergoing surgery with arch reconstruction [9]. In a *homogeneous* population of infants with HLHS, Dent et al. reported that having a post-operative cerebral oxygenation, measured with commercial

NIRS, less than 45% for at least 180 min was significantly associated with post-operative PVL [70]. This finding was not replicated later in a mixed population by Andropoulus et al [67].

6.1.3 Transposition of the Great Arteries

Description of defect

Transposition of the great arteries (TGA) is another common critical CHD and slightly more prevalent than HLHS [74]. In TGA, the pulmonary artery, which carries oxygen-poor blood from the heart to the lungs, and the aorta, which carries oxygen-rich blood from the heart to the body, are transposed. Therefore, left uncorrected, oxygen-poor blood will continue to cycle through the body without returning to the lungs to become oxygenated. Following birth, a balloon atrial septostomy is performed in some patients, which opens a connection between the right and left atrium, allowing mixing of oxygen-rich and oxygen-poor blood while the baby waits for their corrective surgery.

Previous findings on neurodevelopmental outcome

As with HLHS and other CHD, TGA is associated with neurodevelopmental dysfunction later in life (see Section 1.2). The Boston Circulatory Arrest Study investigated the outcomes of 139 16-year-old children with TGA who underwent corrective surgery as infants [65]. Again, there was a high use of ancillary educational services (65%), which included tutoring (37%), grade retention (17%), early intervention (19%), occupational therapy (23%), full-time special education classroom (25%), and counseling (25)%.

As seen in the cohort presented herein as well as in previous cohorts of infants with TGA, the highest incidence of PVL seen in these patients is on pre-operative MRI scans (see Section 6.4) [10, 75, 76]. Petit et al. investigated risk factors for this pre-operative PVL, and found that time-to-surgery and pre-operative arterial oxygenation [10]. This work was the first to suggest that, at least in infants with TGA, earlier surgery may mitigate the risk for developing PVL. Anderson et al. recently augmented these findings in a retrospective study showing that earlier surgery in infants with TGA was associated with less major morbidity, including seizure and stroke [77].

6.2 Study Protocol

All procedures were approved by the Institutional Review Board at CHOP. Patients with complex congenital heart were included in this study. Patient demographic data, including time of birth, gestational age, birth weight, head circumference on day of surgery, gender and cardiac diagnosis, were recorded. A timeline of the study is presented in Figure 30. On the morning of surgery, all patients received general anesthesia (fentanyl 5-10 μg/kg, pancuronium 0.2mg/kg) with endotracheal intubation. Subsequently, they underwent a brain MRI for pre-operative injury assessment. Pre-operative DOS/DCS measurements of cerebral oxygenation (StO_2) and blood flow index (BFI) were also made at this time.

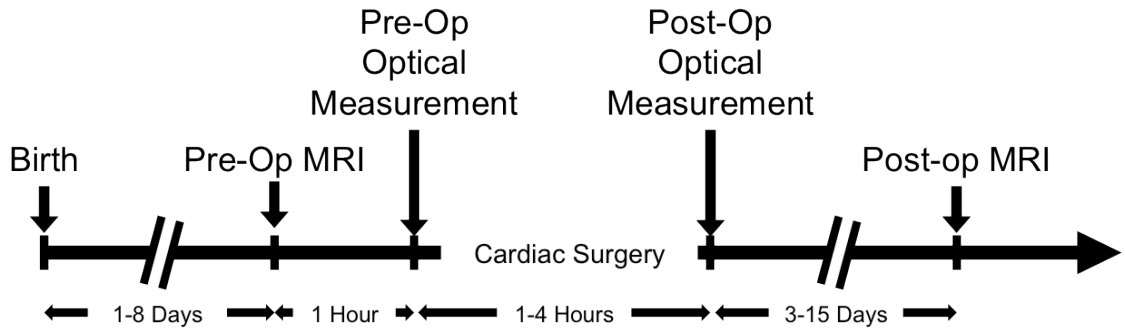

Figure 30: Timeline of study of infants with CHD.

After the MRI, patients underwent surgery. All surgery was performed under cardiopulmonary bypass with some diagnoses requiring deep hypothermic circulatory arrest (DHCA) for aortic arch repair (see Section 6.3). To achieve DHCA, patients underwent core and surface cooling to a nasopharyngeal (NP) temperature of 18°C, at which point the bypass machine is stopped and the bypass cannulas are removed from the surgical field. Antegrade cerebral perfusion was not used as it is at some other centers. The surgeries were either corrective or palliative, depending on the diagnosis (see Section 6.3). Operations were performed by one of four cardiac surgeons. pH-stat blood gas management was used to adjust for gas solubility at lower temperatures. Modified ultrafiltration was performed in all patients after CPB. Commercial cerebral oximetry was not used to guide intraoperative or post-operative management. Surgical strategy included sternal closure where tolerated.

After surgery, the patients were transported back to the cardiac intensive care unit (CICU). Post-operative StO_2 and CBF were quantified every 2 hours for the first 12 hours during recovery in the CICU. Approximately 1 week after surgery, patients underwent a post-operative follow-up MRI scan to assess the development and/or progression of brain

injury.

6.2.1 Brain MRI

All images were acquired on a 1.5T Avanto MRI system (Siemens Medical Systems, Malvern, NJ, USA) using a 12-channel head coil. Studies included T1 MPRAGE (Magnetization-Prepared Rapid Acquisition Gradient Echo) and T2 SPACE (Sampling Perfection with Application-optimized Contrasts using different flip angle Evolution). All sequences were acquired in the axial plane and were later reconstructed in the sagittal and coronal planes. Susceptibility sequences (susceptibility weighted imaging, SWI), and diffusion weighted imaging (DWI) sequences were also acquired. The presence of PVL was assessed from T1 sequences in conjunction with DWI in both the pre- and post-operative scans. Manual segmentation of the T1 hyperintense lesions were performed using ITK-SNAP [78] and were used to calculate PVL volumes. New or worsened PVL was calculated by the difference in PVL volume between the post and pre-operative scans. In addition to PVL classification, two independent observers blinded to clinical data evaluated brain maturation by quantifying a total maturation score (TMS) using axial T1 and T2 images [79, 80].

6.2.2 DOS/DCS Measurements

DOS and DCS measurements were conducted once pre-operatively, once post-operatively immediately after return to the CICU, and then once every 2 hours for the subsequent 12 hours. For statistical analysis of post-operative measurements, we included only the initial value of StO_2 and BFI upon return to the CICU and the lowest measured post-operative value of StO_2. Measurements were made over both the right and

left frontal cortex. At each location, four repetitions were acquired in order to account for local inhomogeneities under the optical probe. These 8 repetitions were then averaged together to derive a global measure of StO_2 and BFI. Optical data measured with DOS and DCS, i.e., StO_2, and BFI, were acquired on only a subset of patients due to a change in protocol that used improved optical instrumentation and allowed for these optical measurements partway through enrollment.

6.2.3 Statistical Analysis

Continuous variables were summarized by standard descriptive statistics (mean, standard deviation (SD), and median, interquartile range (IQR) as appropriate), and frequencies and percentages for categorical variables. Continuous variables were compared between groups by employing Wilcoxon rank-sum tests.

6.3 Patient population

At the time of writing this thesis, we have recruited a total of N=98 subjects under the protocol described in Section 6.2. Three of these subjects were consented but not studied due to availability of the MRI on the morning of the scheduled surgery. All subjects were full term and medically stable for at least 24 hours prior to the day of surgery. Our study protocol excluded recruitment of any infant born prematurely (< 37 week gestational age), infants with neonatal depression, infants who are small for their gestational age (< 2 kg), infants who had perinatal seizures, infants who displayed evidence of other end-organ injury, infants who had pre-operative cardiac arrest acquiring chest compression, and any infant with significant intracerebral hemorrhage.

The majority of the subjects that were studied (N=95) were diagnosed with either hyperplastic left heart syndrome (N=46) or transposition of the great arteries (N=32). The remaining subjects had the following primary diagnoses: Tetralogy of Fallot (N=5), heterotaxy (N=1), coarctation of the aorta (N=1), aortic stenosis (N=1), tricuspid atresia (N=1), double-inlet left ventricle (N=1), hypoplastic arch (N=2), pulmonary atresia (N=1), ventricular septal defect (N=1), and interrupted aortic arch (N=3).

Table 6: Description of groups used to categorize subjects.

	Palliative or Corrective	**DHCA or No DHCA**	**Diagnoses Included**
Group 1	Palliative	DHCA	HLHS, HLHS variants, Tricuspid Atresia, DILV
Group 2	Corrective	No DHCA	TGA, ToF, Heterotaxy
Group 3	Palliative	No DHCA	PA
Group 4	Corrective	DHCA	CoA, Aortic Stenosis, Hypoplastic Arch, IAA, VSD

DHCA, Deep Hypothermic Circulatory Arrest; *HLHS,* Hypoplastic Left Heart Syndrome; *DILV*, Double Inlet Left Ventricle; *VSD*, Ventricular Septal Defect; *TGA,* Transposition of the Great Arteries; *ToF*, Tetralogy of Fallot; *PA*, Pulmonary Atresia; *CoA*, Coarctation of Aorta; *IAA*, Interrupted Aortic Arch

Due to the large number of diagnoses and the limited number of subjects recruited with each diagnosis (other than TGA and HLHS), we group similar diagnoses together. We define four groups based on whether or not the surgery the patient undergoes is palliative or corrective and whether or not the surgery is done under DHCA. A

description of thee groups appears in Table 6. The demographic data for these subjects are reported Table 7.

Table 7 Demographic data for the infants with CHD studied. All continuous variable are listed as mean ± standard deviation.

Group	N	Female (n)	Age at Surgery (days)	Gestational Age (weeks)	Birth Weight (kg)	Head Circumference
Group 1	48	20	4.0±1.8	39.0±0.8	3.4±0.5	34.2±1.3
Group 2	37	15	3.9±1.8	38.9±1.0	3.6±0.5	34.5±1.0
Group 3	1	0	2.0	37.1	3.1	34.0
Group 4	9	6	6.3±4.1	38.6±1.3	3.2±0.6	33.8±1.5
All	**95**	**41**	**4.2±2.2**	**38.9±0.9**	**3.4±0.5**	**34.3±1.2**

6.4 Results

Not all of the optical measurements described in Section 6.2 were made on all 95 subjects. This was due to either data quality or availability of the optical instrument, optical probes, or personnel on the day of surgery. Pre-operative variables measured with optics on the morning of surgery are listed in Table 8, with averages given for each group of subjects. Variables include total hemoglobin concentration (THC, in units of μM), cerebral tissue oxygen saturation (StO_2), cerebral blood flow index (BFI, in units of cm^2/s), oxygen extraction fraction (OEF), and an index of cerebral metabolic rate of oxygen ($CMRO_{2,i}$, in units of $ml/dl \times cm^2/s$). The same variables, measured immediately upon return to the cardiac intensive care unit (CICU) from surgery are reported in Table 9.

Table 8: Preoperative optical variables for all infants with CHD studied. Values are reported as mean ± standard deviation. Not all measurements were conducted on all subjects. The number in brackets represents the number of subjects with that measured parameter.

Group	THC (μM)	StO_2 (%)	BFI (10^8 cm^2/s)	OEF	$CMRO_{2,i}$ (10^{-7} ml/dl × cm^2/s)
Group 1 N=48	38.1±11.5 [39]	46.0±11.7 [39]	2.6±1.6 [37]	0.47±0.14 [33]	1.6±1.4 [32]
Group 2 N=37	38.2±7.9 [25]	51.0±9.9 [25]	3.3±2.1 [24]	0.38±0.12 [22]	1.6±1.1 [21]
Group 3 N=1	37.1 [1]	63.9 [1]	2.5 [1]	0.27 [1]	0.8 [1]
Group 4 N=9	47.3±18.2 [9]	56.0±13.1 [9]	1.3±0.6 [9]	0.33±0.10 [7]	0.6±0.4 [6]
All N=95	**39.4±11.6 [74]**	**49.1±11.7 [74]**	**2.7±1.8 [71]**	**0.42±0.14 [63]**	**1.5±1.3 [60]**

THC, Total Hemoglobin Concentration; *StO_2,* Cerebral Tissue Oxygen Saturation; *BFI*, Blood Flood Index; *OEF*, Oxygen Extraction Fraction; *$CMRO_{2,i}$,* Cerebral Metabolic Rate of Oxygen

One goal of this study was to investigate the difference in post-operative cerebral hemodynamics between these four different groups who underwent significantly different cardiac surgeries and, as we are learning, also display significantly different incidences of PVL (Table 10). However, at the time of writing this thesis, we have not recruited enough subjects for Groups 3 or 4 to perform an adequate analysis on the differences between these four groups. Therefore, the remainder of this Section will focus exclusively on infants with HLHS and TGA.

Table 9: Postoperative optical variables for all infants with CHD studied. Values are reported as mean ± standard deviation. Not all measurements were conducted on all subjects. The number in brackets represents the number of subjects with that measured parameter.

Group	THC (μM)	StO_2 (%)	BFI (10^8 cm^2/s)	OEF	$CMRO_{2,i}$ (10^{-7} ml/dl × cm^2/s)
Group 1 N=48	71.1±14.5 [35]	41.5±7.0 [35]	2.0±1.6 [31]	0.43±0.11 [33]	1.3±1.3 [29]
Group 2 N=37	58.9±15.3 [26]	55.0±11.2 [26]	2.5±1.6 [26]	0.44±0.11 [23]	1.7±1.1 [23]
Group 3 N=1	71.3 [1]	59.8 [1]	3.9 [1]	0.11 [1]	0.5 [1]
Group 4 N=9	69.0±25.9 [8]	52.0±6.9 [8]	1.8±2.1 [8]	0.47±0.09 [7]	1.2±1.3 [7]
All N=95	**66.3±17.0 [70]**	**48.0±10.8 [70]**	**2.2±1.6 [66]**	**0.44±0.11 [64]**	**1.4±1.2 [60]**

THC, Total Hemoglobin Concentration; *StO_2,* Cerebral Tissue Oxygen Saturation; *BFI*, Blood Flood Index; *OEF*, Oxygen Extraction Fraction; *$CMRO_{2,i}$,* Cerebral Metabolic Rate of Oxygen

Table 10 summarizes the results of the volumetric amount of PVL from the pre- and post-operative MRI scans on all N=95 subjects. One can see from this table that there is significant variation between the different groups (see Section 6.4.1). The rest of this Section will delve into predictive risk factors for this PVL in infants with HLHS and TGA.

Table 10: Pre-operative and post-operative volumes of PVL averaged over the four different groups of patients. Continuous variables are reported mean ± standard deviation and incidence of PVL is reported as N (%).The volumetric amount represents the average, non-zero volume of PVL.

Diagnosis	Pre-Operative		Post-Operative		
	PVL N (%)	Volume (mm^3)	MRI N (%)	PVL N (%)	Volume (mm^3)
Group 1 N=48	9 (19.2%)	223.3±288.1	42 (87.5%)	31 (73.8%)	833.9±1637.6
Group 2 N=37	7 (18.9%)	190.7±361.9	35 (94.6%)	7 (20.0%)	179.4±398.5
Group 3 N=1	1 (100%)	16.9	1 (100%)	1 (100%)	37.5
Group 4 N=9	2 (22.2%)	8.5±2.2	8 (88.9%)	4 (50.0%)	107.9±70.3
All N=95	**19 (20.2%)**	**175.3±293.8**	**86 (90.5%)**	**43 (50.0%)**	**641.3±1427.3**

6.4.1 Differences between HLHS and TGA

We have studied a total of N=78 patients with either HLHS (N=46) or TGA (N=32). The demographic data for these 78 patients are described in Table 11.

Table 11: Patient demographics for all infants with HLHS and TGA.

Group	N	Female (n)	Age at Surgery (days)	Gestational Age (weeks)	Birth Weight (kg)	Head Circumference
HLHS	46	20	4.0±1.9	39.0±0.8	3.4±0.5	34.2±1.4
TGA	32	12	3.5±1.2	38.9±1.0	3.5±0.5	34.4±1.0
All	**78**	**32**	**4.8±1.6**	**38.9±0.9**	**3.4±0.5**	**34.3±1.2**

Table 12: Pre-operative and post-operative volumes of PVL averaged over the population of infants with HLHS and infants with TGA. Continuous variables are reported as mean ± standard deviation and incidence of PVL is reported as N (%). The volumetric amount represents the average, non-zero volume of PVL.

Diagnosis	Pre-Operative		Post-Operative		
	PVL N (%)	Volume (mm^3)	MRI N (%)	PVL N (%)	Volume (mm^3)
HLHS N=46	9 (20.0%)	223.3±288.1	40 (87.0%)	29 (72.5%)	793.3±1647.8
TGA N=32	6 (18.8%)	219.8±387.3	30 (93.8%)	5 (16.7%)	237.1±472.7
All N=95	**15 (19.5%)**	**221.8±320.0**	**70 (89.7)%**	**34 (48.6%)**	**711.5±1539.8**

As was briefly mentioned earlier in this Section, we see a difference in the incidence of PVL between these two diagnoses. Table 12 summarizes the incidence and volumetric amount of PVL seen in infants with HLHS and TGA both pre- and post-operatively. As is apparent from Table 12, there is a striking difference between these two groups in both the incidence of post-operative PVL and in the average non-zero volumetric amount. To further illustrate this, Figure 31 shows a boxplot of post-operative volumes separated by diagnosis. Note, this figure includes patients who had a volume of 0 mm^3 and several outliers had to be removed from the HLHS group for visualization purposes. One can see that the median volume of post-operative PVL is significantly different between the two groups ($p<0.00001$; Wilcoxon Rank-sum). Therefore, infants with HLHS are at a much greater risk for injury than infants with TGA, and the majority of injury is seen on a post-operative, rather than pre-operative, MRI scan.

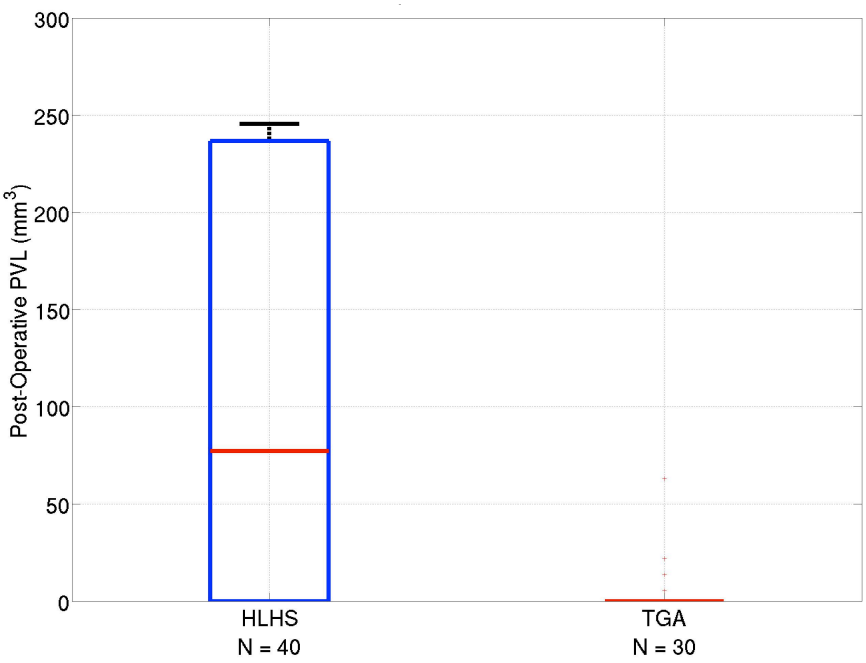

Figure 31: Boxplot of post-operative PVL volumes for infants with HLHS and TGA. Infants with HLHS have significantly more post-operative PVL than infants with TGA. The red line denotes the median value; the blue square extends to the 25th and 75th percentiles; the whiskers extend to the most extreme data points that are not outliers; and the outliers are plotted as individual points.

We do not see a significant difference in volumetric amount or incidence of pre-operative PVL between these two cohorts. However, it is important to note that we observed less incidence of pre-operative PVL in infants with TGA than has been previously reported [10]. This may be due to the fact that the cohort studied by Petit et al. went to surgery an average of 1 day later than the population studied here. This is likely due to change of practice as a result of the findings in the study by Petit at al. that show that shorter time-to-surgery could be preventative against pre-operative PVL [10].

To understand this observed difference in PVL between these two diagnoses, we investigated differences in both pre- and post-operative cerebral hemodynamics. Table

13 summarizes pre-operative optical variables. As you can see, these parameters are fairly similar between the two groups, which is further illustrated in Figure 32.

Table 13: Pre-operative optical variables for infants with HLHS and TGA. Values are reported as mean ± standard deviation. Not all measurements were conducted on all subjects. The number in brackets represents the number of subjects with that measured parameter.

Group	THC (μM)	StO_2 (%)	BFI (10^8 cm^2/s)	OEF	$CMRO_{2,i}$ (10^{-7} ml/dl × cm^2/s)
HLHS N=46	38.3±11.8 [37]	46.3±12.0 [37]	2.5±1.6 [35]	0.47±0.14 [31]	1.6±1.5 [30]
TGA N=32	37.2±7.0 [21]	49.5±9.9 [21]	3.1±2.1 [21]	0.40±0.12 [18]	1.5±1.2 [18]
All N=78	**37.9±10.2 [58]**	**47.5±11.3 [58]**	**2.7±1.8 [56]**	**0.44±0.13 [49]**	**1.5±1.4 [48]**

THC, Total Hemoglobin Concentration; *StO_2,* Cerebral Tissue Oxygen Saturation; *BFI*, Blood Flood Index; *OEF*, Oxygen Extraction Fraction; *$CMRO_{2,i}$,* Cerebral Metabolic Rate of Oxygen

Table 14 summarizes post-operative optical variables measured upon immediate return to the CICU. As is shown in Table 14, there is a significant difference between in post-operative StO_2 and THC between these two groups. This is illustrated in the box-plots in Figure 33.

Table 14: Post-operative variables measured with optics. Values are reported as mean ± standard deviation. Not all measurements were conducted on all subjects. The number in brackets represents the number of subjects with that measured parameter.

Group	THC (μM)	StO_2 (%)	BFI (10^8 cm^2/s)	OEF	$CMRO_{2,i}$ (10^{-7} ml/dl × cm^2/s)
HLHS N=46	71.8±14.0 [34]	41.2±6.7 [34]	1.9 ±1.6 [30]	0.44±0.11 [32]	1.3±1.3 [28]
TGA N=32	58.0±15.3 [22]	55.6±11.2 [22]	2.3±1.5 [21]	0.43±0.11 [20]	1.4±0.7 [19]
All N=78	**66.4±15.9 [56]**	**46.8±11.2 [56]**	**2.1±1.5 [51]**	**0.44±0.11 [52]**	**1.3±1.1 [47]**

THC, Total Hemoglobin Concentration; *StO_2,* Cerebral Tissue Oxygen Saturation; *BFI*, Blood Flood Index; *OEF*, Oxygen Extraction Fraction; *$CMRO_{2,i}$,* Cerebral Metabolic Rate of Oxygen

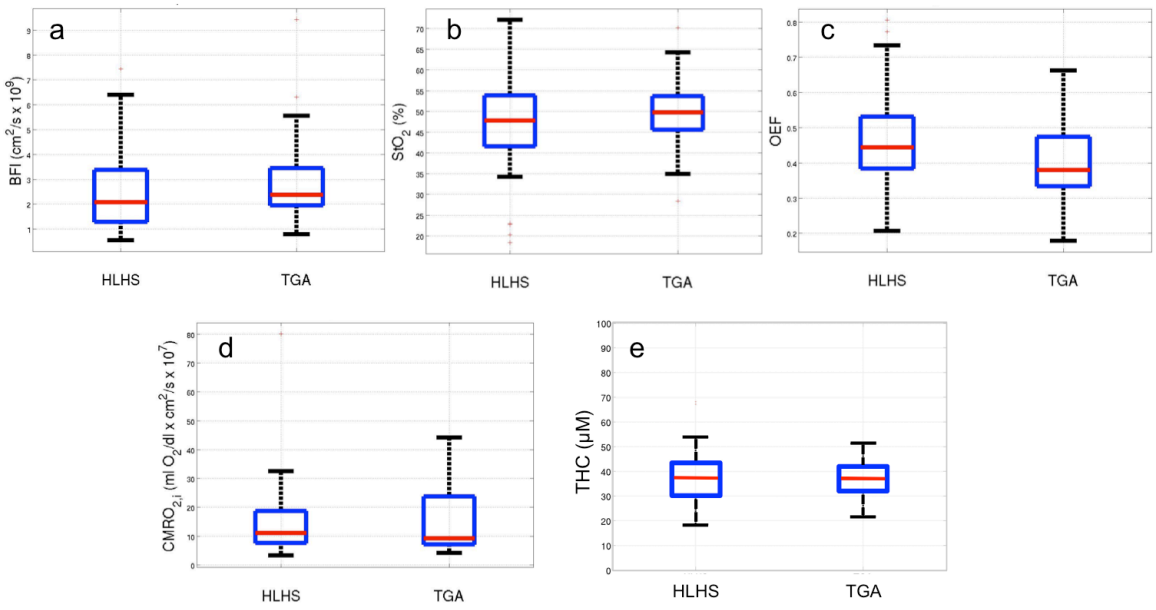

Figure 32: Boxplot of pre-operative optical variables for infants with HLHS and TGA. Pre-operative optical variables are BFI (a), StO_2 (b), OEF (c), $CMRO_{2,i}$ (d), THC (e). We observe no differences in any of these variables between infants with HLHS and TGA. The red line denotes the median value; the blue square extends to the 25th and 75th percentiles; the whiskers extend to the most extreme data points that are not outliers; and the outliers are plotted as individual points.

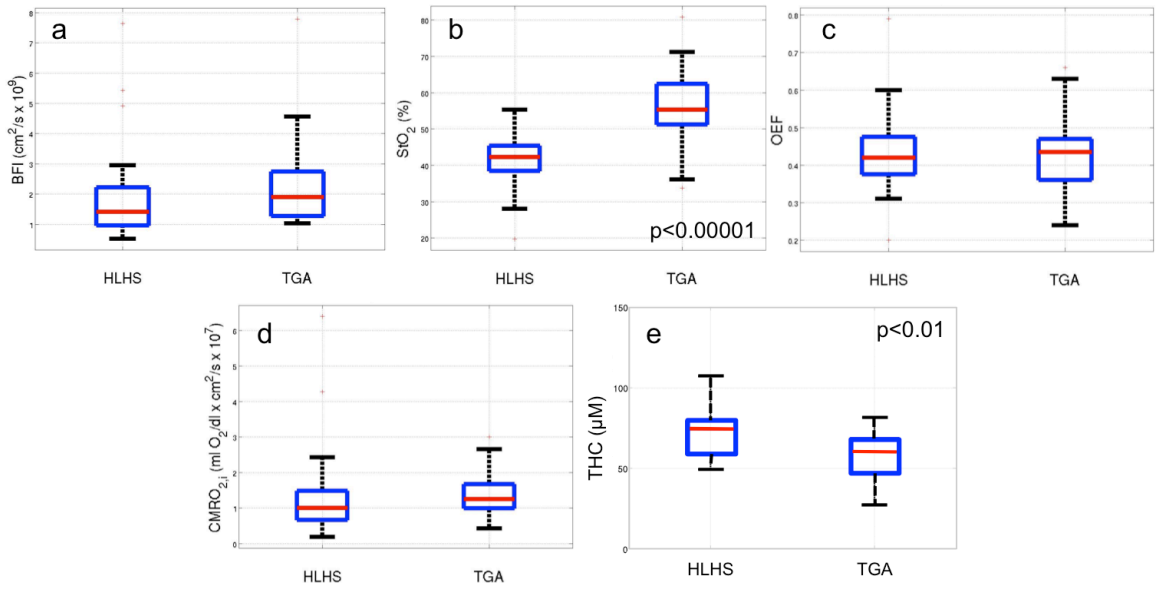

Figure 33: Boxplot of post-operative variables for infants with HLHS and TGA. Post-operative variables are BFI (a), StO_2 (b), OEF (c), $CMRO_{2,i}$ (d), THC (e). WE observe a significant difference in StO_2 and THC between the two diagnoses. The red line denotes the median value; the blue square extends to the 25th and 75th percentiles; the whiskers extend to the most extreme data points that are not outliers; and the outliers are plotted as individual points.

The significant differences in post-operative StO_2 THC, and PVL between infants with HLHS and TGA suggests that the high risk for post-operative PVL seen in HLHS is due to post-operative parameters. The next section focuses only on infants with HLHS to identify risk-factors for this high prevalence of PVL.

6.4.2 Risk factors for PVL in HLHS

The major result to come out of this work is on an investigation of the risk factors for PVL in infants with HLHS. Of the N=46 neonates with HLHS that have been studied so far, post-operative MRIs were not acquired on 6 subjects due to the following reasons: four patients were deemed clinically unstable for a post-operative MRI during study period, one subject had a pacemaker placed and was thus unable to undergo an MRI, and

one subject was withdrawn from the post-operative MRI due to parental request. Thus, both pre- and post-operative MRI scans were acquired on N=40 subjects. Relevant clinical data was not currently available on the most recent 3 subjects, so the subsequent analysis was performed on N=37 neonates diagnosed with HLHS (n=30) or HLHS variants (n=7). The HLHS variants consisted of unbalanced atrioventricular canal (n=4), double outlet right ventricle (n=2), and mitral valve dysplasia and aortic valve stenosis (n=1), and all were associated with significant aortic arch hypoplasia. All patients were full term with an average gestational age of 38.9±0.8 weeks. Patient demographics and pre-operative and post-operative cerebral hemodynamics are described in Table 15.

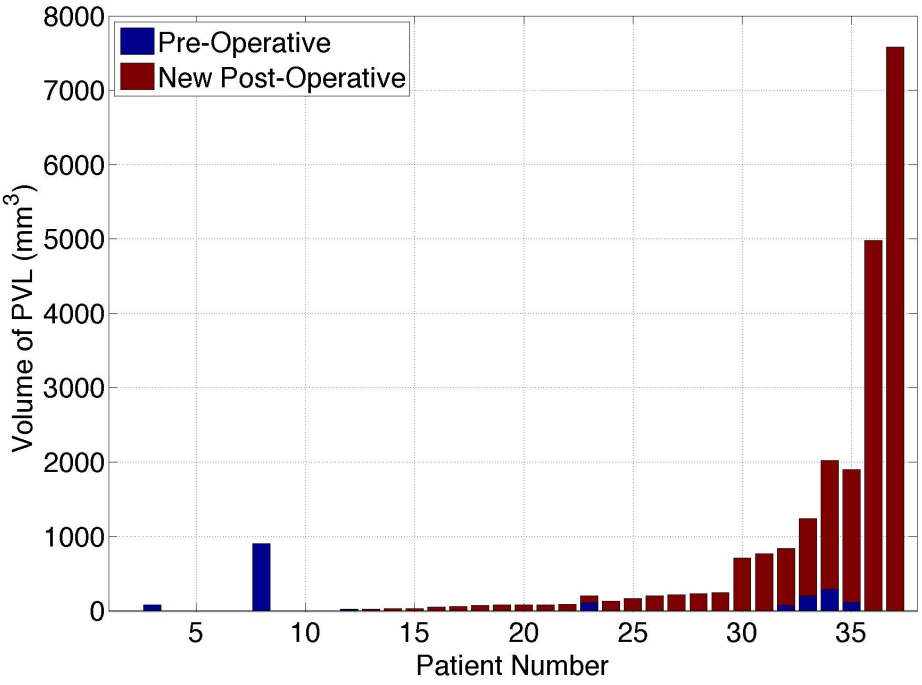

Figure 34: Volumetric amount of pre- and new post-operative PVL in neonates with HLHS. The full bar represents the volume of PVL on post-operative scans, with the volume that was present on pre-operative scans shown in blue. Subjects are numbered in order of increasing change in PVL volume between pre- and post-operative MRI scans.

Table 15: Summary of demographic and pre- and post-operative cerebral hemodynamic variables measured for all subjects with HLHS. Continuous variables are presented by means ± standard deviation for continuous variables and frequencies (%) for categorical variables.

Time-to-surgery, days	4.2±1.9
Time between MRI, days	7.1±2.8
Gestational age, wk	38.8±0.8
Birth weight, kg	3.3±0.5
Head circumference, cm	34.0±1.4
Female, n (%)	19 (51.4)
Aortic Stenosis, n (%)	9 (27.3)
TMS	9.9±0.9
Pre-operative SaO_2, %	90.0±5.2
StO_2, %	48.8±13.3
BFI, 10^{-8} cm^2/s	2.4±1.6
CBV, mL/100g	2.1±0.5
$CMRO_{2,I}$, 10^{-7} ml/dl × cm^2/s	1.6±1.4
CPB time,	92.2±25.3
DHCA time, min	44.8±9.7
Lowest NP temperature,	17.8±0.9
Number of bypass runs, n	1.1±0.4
Delayed sternal closure, n (%)	5 (13.5)
Cardiac arrest, n (%)	1 (2.7)
Initial StO_2, %	40.8±7.2
Initial BFI, 10^{-8} cm^2/s	1.5±0.7
Initial CBV, mL/100g	3.9±0.7
Initial $CMRO_{2,i}$, 10^{-7} ml/dl × cm^2/s	1.4±1.3
Lowest StO_2, %	35.0±9.4

TMS, Total Maturation Score; *SaO_2,* arterial oxygen saturation; *StO_2*, cerebral tissue oxygen saturation; *BFI,* Blood Flow Index; *CBV*, Cerebral Blood Volume; *$CMRO_{2,i}$,* Index of Cerebral Metabolic Rate of Oxygen; *CPB,* Cardiopulmonary Bypass; *DHCA*, Deep Hypothermic Circulatory Arrest; *NP*, Nasopharyngeal.

Figure 34 depicts the volumetric amount of PVL acquired pre- and post-operatively in the 37 subjects studied herein. Eight (21.6%) patients had pre-operative

and 28 (75.7%) had post-operative PVL. Additionally, most subjects who had pre-operative PVL acquired more post-operatively. Therefore, we chose to focus on the difference between the volumes of PVL acquired post- and pre-operatively. The distribution of this parameter is shown in Figure 35. An increase in volume from pre- to post-operative PVL was observed in 26/37 (70.3%) of patients, and the acquired volume ranged from 2.5 mm^3 to 7577.7 mm^3. As is apparent from Figure 35, the distribution of change in volume of PVL is highly skewed.

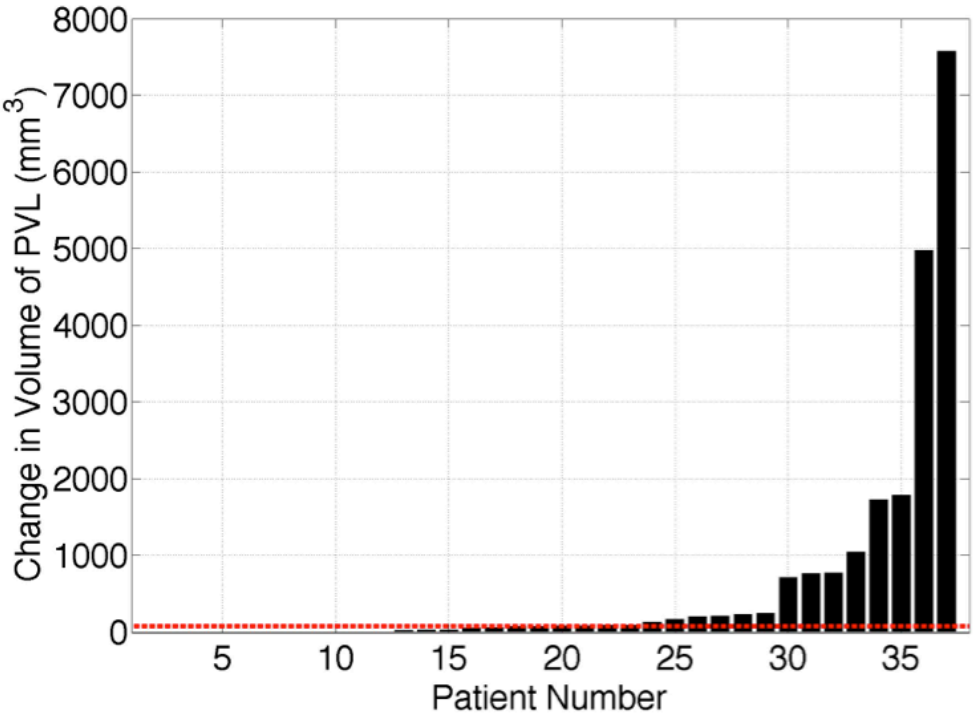

Figure 35: Change in volume of PVL between pre- and post-operative MRI scans. The red line denotes the median value of change in PVL volume. Subjects are numbered in order of increasing change in PVL volume.

Because of the highly skewed distribution of change in PVL volumes in the present dataset, the outcome variable of new or worsened post-operative PVL was dichotomized around its median value. Figure 36 illustrates an example of a large

volume (7577.7 mm^3) versus a small volume (70.7mm^3) of PVL. Table 16 give the pre- and post-operative and demographic data for those subjects with a large change in post-operative PVL and those without or with a small amount. The group with a large amount of post-operative of PVL had a mean time-to-surgery of 5.3±1.5 days, compared with 3.1±1.7 days for the no or small amount of PVL group (p=0.0003). Further, patients with new or worsened post-operative PVL tended to have higher pre-operative BFI (p=0.05) and lower pre-operative StO_2 (p=0.09). Of note, TMS, post-operative StO_2, and DHCA duration were not significantly different between the two groups.

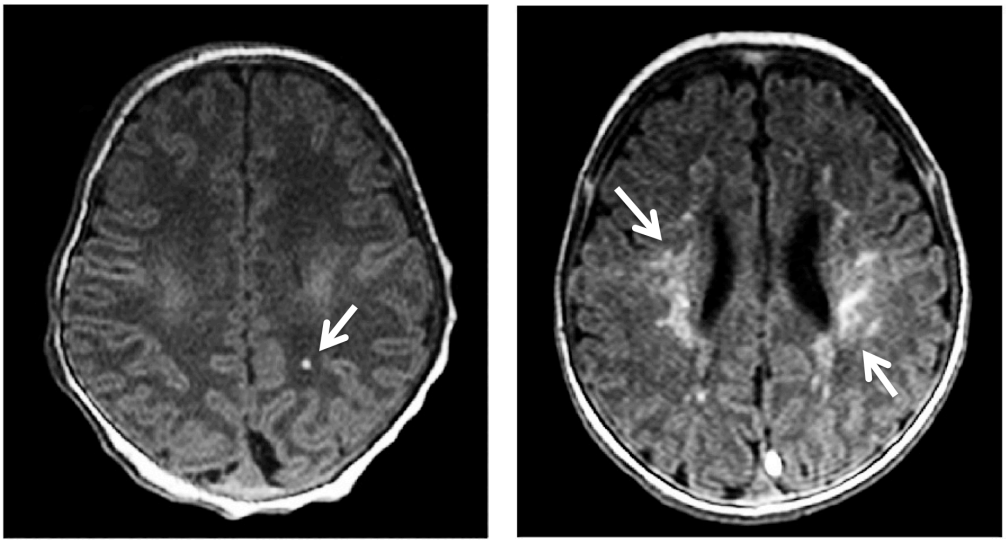

Figure 36: An example of a small volume (left, 70.7 mm^3) and a large volume (right, 7577.7 mm^3) of PVL.

Table 16: Summary of demographic and pre- and post-operative cerebral hemodynamic variables measured for subjects with and without new or worsened PVL > 76.3 mm^3. Continuous variables are presented as means ± standard deviation for continuous variables and frequencies (%) for categorical variables.

Variable	PVL (n=18)	No PVL (n=19)	P
Time-to-surgery, days	5.3±1.5	3.1±1.7	<0.001*
Time between MRI, days	7.1±2.9	7.0±2.9	0.90
Gestational age, wk	38.9±0.9	38.8±0.7	0.59
Birth weight, kg	3.3±0.5	3.2±0.5	0.77
Head circumference, cm	34.1±1.5	34.0±1.3	0.55
Female, n (%)	10 (55.6)	9 (47.4)	0.64
Aortic Atresia, n (%)	5 (31.3)	4 (23.5)	0.64
TMS	10.1±0.9	9.8±1.0	0.34
Pre-operative SaO_2, %	90.1±4.0	89.9±6.1	0.57
StO_2, %	44.3±13.4	54.3±11.3	0.09#
BFI, 10^{-8} cm^2/s	3.0±1.9	1.9±1.1	0.05#
CBV, mL/100g	2.1±0.6	2.1±0.4	0.52
$CMRO_{2,I}$, 10^{-7} ml/dl × cm^2/s	2.1±2.0	1.2±0.7	0.13
CPB time,	96.8±33.0	87.7±14.5	0.70
DHCA time, min	46.4±12.0	43.3±6.7	0.74
Lowest NP temperature,	17.9±1.0	17.6±0.8	0.20
Number of bypass runs, n	1.2±0.5	1.0±0	0.14
Delayed sternal closure, n (%)	4 (22.2)	1 (5.3)	0.14
Cardiac arrest, n (%)	1 (5.6)	1 (0)	0.33
Initial StO_2, %	41.3±7.6	40.4±7.1	0.57
Initial BFI, 10^{-8} cm^2/s	1.6±0.9	1.3±0.3	0.35
Initial CBV, mL/100g	3.9±0.7	3.8±0.8	0.83
Initial $CMRO_{2,i}$, 10^{-7} ml/dl × cm^2/s	1.5±1.1	1.3±1.6	0.24
Lowest StO_2, %	34.2±10.5	35.9±8.3	0.65

A Wilcoxon rank-sum test used to test differences between the two groups. (* significant, # marginally significant). *TMS,* Total Maturation Score; *SaO_2,* arterial oxygen saturation; *StO_2*, cerebral tissue oxygen saturation; *BFI,* Blood Flow Index; CBV, Cerebral Blood Volume; *$CMRO_{2,i}$,* Index of Cerebral Metabolic Rate of Oxygen; *CPB,* Cardiopulmonary Bypass; *DHCA*, Deep Hypothermic Circulatory Arrest; *NP*, Nasopharyngeal.

Furthermore, multivariate logistic regression was performed to evaluate the significance of the explanatory variables to predict the likelihood of developing a large amount (i.e., greater than the median value) of new or worsened post-operative PVL. The final selected model was determined by stepwise selection, which is a combination of backward elimination and forward selections. In stepwise selection, an attempt is made to remove any insignificant variables from the model before adding a significant variable to the model. Each addition or deletion of a variable to or from a model is a separate step and at each step a new model is fitted. The selection criteria was $p<0.1$. All variables tested in the univariate analysis were included for consideration in the stepwise selection approach. The model resulting from this stepwise selection revealed that the probability of acquiring a large amount of PVL was positively associated with time-to-surgery ($p=0.005$), use of delayed sternal closure ($p=0.07$) and pre-operative BFI ($p=0.08$) as described by the formula:

$$\begin{aligned}\text{Log odds of PVL} &= -5.8 + 0.9\times(\text{days to surgery}) \\ &+ 2.9\times(\text{Delayed Sternal Closure}) + 0.8\times(\text{pre-operative BFI}).\end{aligned} \tag{6.1}$$

This model predicts that when holding delayed sternal closure and pre-operative BFI fixed, a one day increase in waiting time will increase the odds of developing PVL by 2.5.

To further illustrate the relationship between time-to-surgery and the likelihood of acquired PVL, Figure 37 shows a boxplot of volume of new or worsened post-operative PVL for those patients going to surgery at day-of-life 4 or earlier and those going to

surgery at day of life 5 or later (p=0.0005). The cut-off of day-of-life 4 was chosen for this visualization, because it resulted in the most significant difference in volume of acquired PVL between groups born before or after the cut-off. However, a cutoff of day-of-life 3 or 5 also resulted in a significant difference in volume of acquired PVL (p=0.005 and 0.02 respectively). Though TMS was included in both the univariate and multivariate analysis, we did not find it to be a significant predictor of new or worsened post-operative PVL.

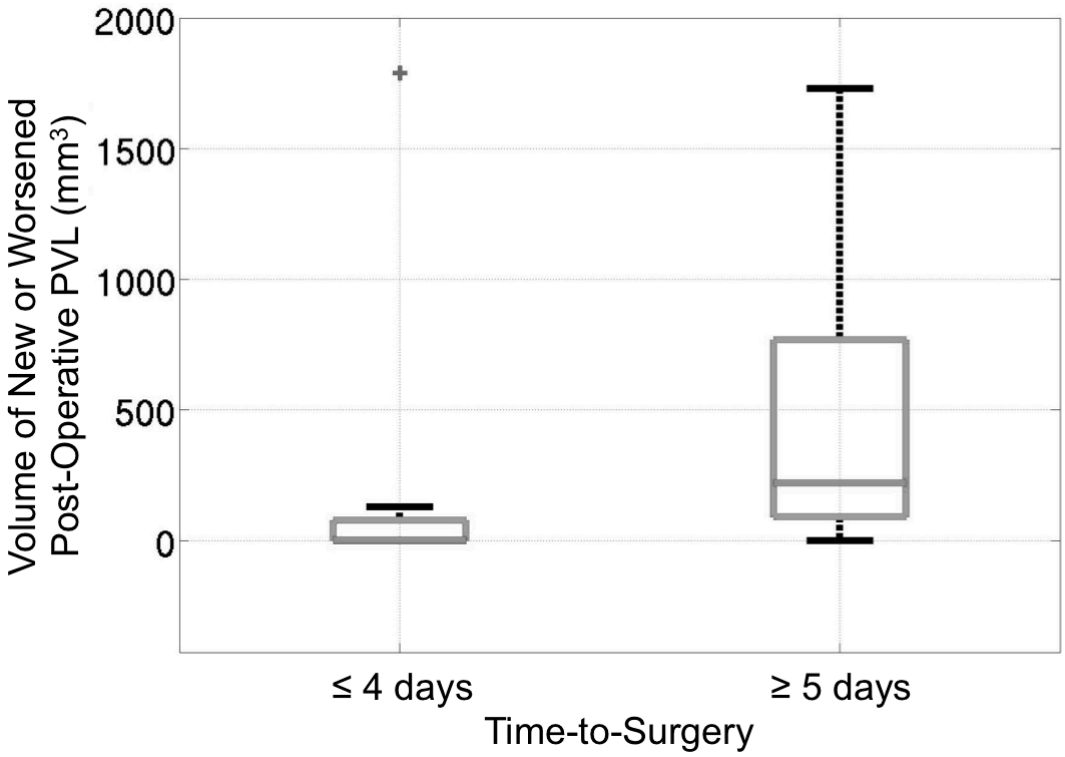

Figure 37: Boxplot of new or worsened PVL. This plot demonstrates the significant (p=0.0005) difference in volume of new or worsened post-operative PVL for those patients going to surgery at day of life 4 or earlier (N=21) and those going to surgery at day of life 5 (N=16) or later. Boxplot demonstrating the significant (p=0.0005) difference in volume of new or worsened post-operative PVL for those patients going to surgery at day of life 4 or earlier (N=21) and those going to surgery at day of life 5 (N=16) or later. Two outliers were removed to improve visualization. One outlier was in the left group and had a PVL volume of 7577.7 mm^3, and the other outlier

was in the right group and had a PVL volume of 4981.5 mm^3. These outliers were only removed from the figure but not from any statistical analysis.

Additionally, we investigated the cross-sectional relationship between day of life and pre-operative StO_2. As seen in Figure 38, a significant and negative linear correlation (R^2=0.15, p=0.05, slope=-2.3±1.2) was observed between time-to-surgery and pre-operative StO_2.

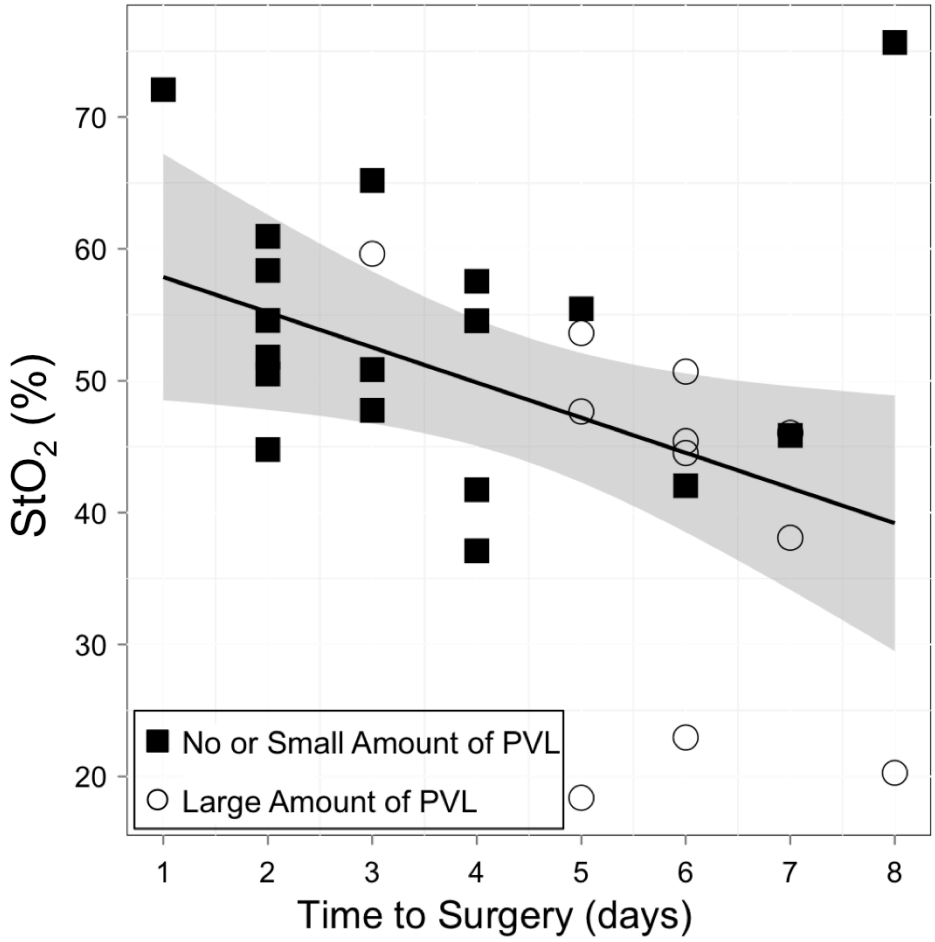

Figure 38: Pre-operative cerebral oxygenation as a function of time-to-surgery. A significant correlation exists between pre-operative StO_2 and time-to-surgery. The solid line represents the bet-fit line to the data (R^2=0.15, p=0.05, slope=-2.3±1.2). The grey ribbon denotes the 95% confidence interval for the mean StO_2. The symbols represent whether or not the subject acquired a large amount of new or worsened post-operative PVL.

Discussion

We focused our study on identifying risk factors for *post*-operative injury, because while patients with HLHS have relatively mild injury pre-operatively, they experience a high rate of new and worsened injury following Stage I palliation [70, 73]. In this cohort the prevalence of any new or worsened PVL was greater than 70%. Because of this highly skewed distribution of PVL volumes, the volumes were dichotomized around the median value to yield 'none/small' volumes and 'large' volumes (more clinically significant). Thus, large volumes of new or worsened *post-operative* PVL occurred in 48.7%.

The major new finding in this study is that acquired *post-operative* PVL in infants with HLHS was highly correlated ($p=0.0003$) with longer time between birth and palliative infant heart surgery (time-to-surgery). No clinical indications were identified that resulted in delay of surgery in the group with a large amount of new or worsened PVL. Delays were due to scheduling or availability of the requested surgeon. The day of the week of the infants birth also played a large role in time-to-surgery. For instance, the n=7 subjects born on a Wednesday had an average time-to-surgery was of 5.1±1.6 days, whereas the n=10 subjects born on a Monday had an average time-to-surgery of 3.7±2.2 days.

One possible explanation for the significance of time-to-surgery on the development of post-operative PVL is the negative linear trend observed between pre-operative StO_2 and time-to-surgery (Figure 38), suggesting that desaturation is occurring from birth until surgery. The correlation of pre-operative StO_2 with new and worsened

post-operative PVL and time-to-surgery suggest that non-invasive optical monitoring of StO_2 during the pre-operative period could be useful in further understanding the timing and cause for PVL and has the potential to further decrease the risk for injury

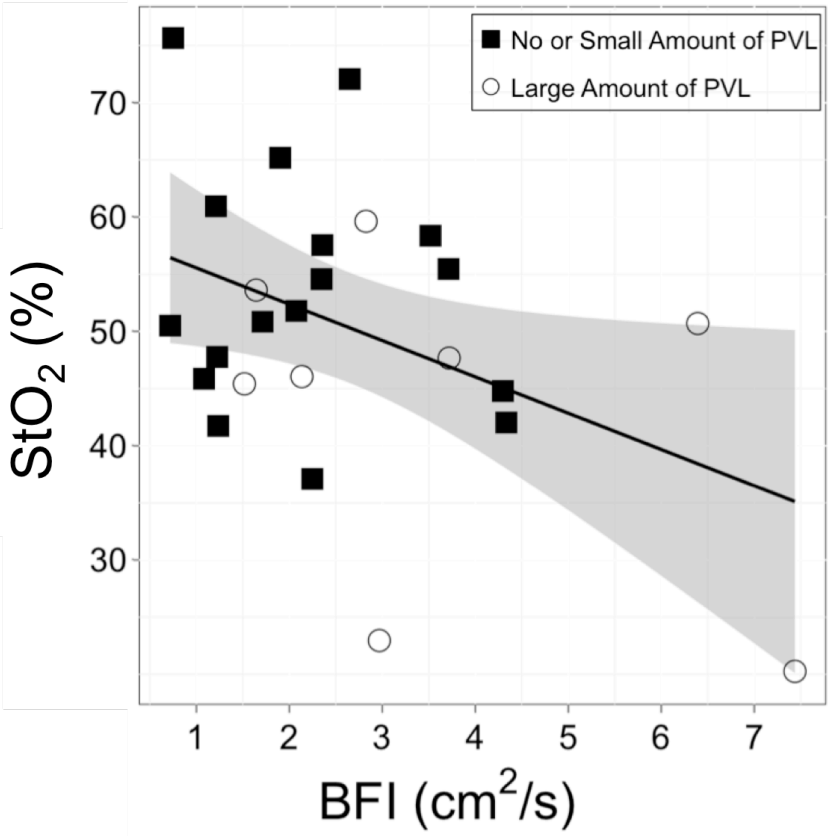

Figure 39: Pre-operative cerebral oxygenation as a function of pre-operative BFI. A significant negative correlation exists between StO_2 and BFI. The solid line represents the bet-fit line to the data (Right: R^2=0.18, p=0.04, slope=-3.2±1.4). The grey ribbon denotes the 95% confidence interval for the mean StO_2. The symbols represent whether or not the subject acquired a large amount of new or worsened post-operative PVL.

The finding that higher pre-operative BFI is associated with new or worsened post-operative PVL in both a univariate and multivariate analysis was surprising and is currently under further investigation. As seen in Figure 39, higher pre-operative BFI is associated with a lower pre-operative StO_2 (R^2=0.18, p=0.04, slope=-3.2±1.4, Figure 39),

suggesting that perhaps cerebral oxygen metabolism is actually increasing pre-operatively in this cohort. That is, this trend is possibly a result of an increasing need for oxygen delivery to meet higher metabolic demand. While this parameter has not been measured in healthy newborn infants, it is likely that $CMRO_2$ increases as infants emerge from the dark, quiet and warm uterine environment into the bright and chaotic world. In infants with severe forms of CHD, this increased oxygen demand may not be well matched with poor, and possibly falling, cerebral oxygen delivery. Although we do not observe higher pre-operative $CMRO_{2,i}$ in infants who waited a long timer for surgery, there exists evidence to suggest that these changes may not be present in the frontal cortex, which is the region probed by all of these measurements. The idea that the oxygen demand is not being met is supported by the observed correlation between higher pre-operative OEF and BFI (Figure 40). Further investigation, including serial measurements of CBF, StO_2, OEF, and $CMRO_2$ from birth to surgery on individual patients with and without severe CHD, is now underway and is crucial for understanding the role of CBF in injury risk (see Section 6.4.4).

It is important to note again that this optically measured BFI is dependent on the optical properties of the tissue, mostly the reduced scattering coefficient (μ_s'), which, in turn, is susceptible to errors arising from the flexible probes used in this study. As explained in Section 4.5, BFI correlated better with blood flow measured in the sagittal sinus by MRI when the reduced scattering coefficient was assumed to be the same for all subjects, i.e., instead of using the measured μ_s' for each subject as was done here. We found that assuming a fixed value for μ_s' for all subjects resulted in a pre-operative BFI

that is not significantly different between the groups with and without a large amount of post-operative PVL. Because of this finding, we believe that further investigation, including more accurate measures of μ_s' and serial measurements of BFI from birth to surgery on individual patients, is necessary.

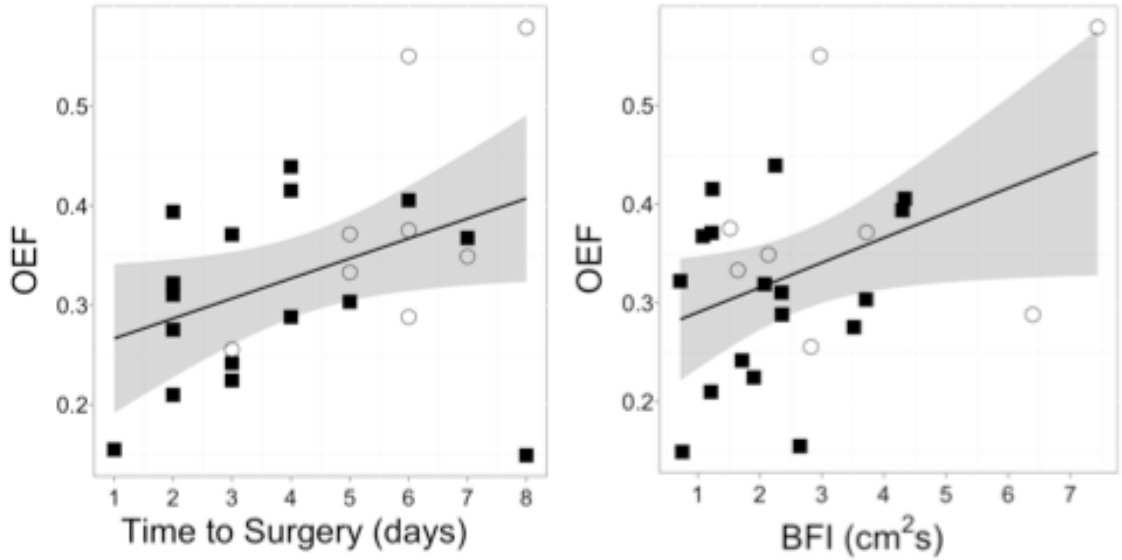

Figure 40: Pre-operative oxygen extraction fraction as a function of time-to-surgery (left) and pre-operative BFI (right). The solid line represents the best-fit line to the data (Left: R^2=0.16, p=0.04, slope=0.02±0.01; Right: R^2=0.16, p=0.05, slope=0.03±0.01). The grey ribbon denotes the 95% confidence interval for the mean OEF. The symbols represent whether or not the subject acquired a large amount of new or worsened post-operative PVL.

In investigations of mixed populations of CHD infants who had early heart surgery with and without DHCA, both the use and total duration of DHCA were found to be a significant risk factor for the development of new post-operative PVL [9]. In the present study, where all patients had HLHS and received DHCA, duration of DHCA was not associated with increased PVL risk.

Operative variables were assessed as risk factors for new or worsened PVL, but

the only variable that rose to significance in the multivariate analysis was whether the sternum was closed primarily or left open due to hemodynamic instability in the immediate post-operative observation period. In the single ventricle reconstruction (SVR) trial, infants who were left with an open sternum post-operatively were at increased risk for both mortality and morbidity [81]. This finding held for both elective delayed sternal closure and for centers where the sternum was routinely left open as part of planned post-operative care. The SVR trial did not evaluate post-operative brain MRIs, so there is no known prior association with white matter injury. However in Beca et al., new postoperative PVL was associated with a higher risk for death after discharge [9].

Previous studies in mixed populations have reported that delayed brain maturation quantified is a risk factor for PVL [9, 67]. In this study, we did not find TMS to be a significant predictor of new or worsened *post-operative* injury in our homogeneous cohort. However, patients with single ventricle physiology have, in general, a lower average brain maturation than other CHD [67] and, as a group, have the highest risk for PVL. Therefore, the association between brain maturation and PVL risk could easily be missed in this report. Other patient characteristics such as gender and HLHS subtype (i.e. aortic atresia or aortic stenosis), which have previously been shown to be significant predictors of *pre-operative* PVL [73], were not significant predictors of acquired *post-operative* injury in this cohort.

The main limitation for this study is that pre-operative cerebral hemodynamics were only measured on the morning of surgery. Thus all temporal data on time-to-

surgery is cross-sectional. To understand the mechanism behind the result that time-to-surgery significantly predicts new or worsened post-operative PVL, longitudinal measures of CBF and StO_2 from birth until surgery are needed. Additionally, the results reported herein are from a single center; these findings should be confirmed at other centers that manage patients with different operative strategies. However, the high statistical significance of the predictability of new or worsened post-operative PVL by time-to-surgery reported herein strongly suggests that decreasing the time to cardiac surgery in neonates with HLHS will decrease the probability of new or worsened post-operative PVL. Since time-to-surgery was largely based on surgeon availability and what day of the week the patient was born on, we find this data provides sufficient justification for modifying the operative scheduling of these patients.

6.4.3 Differences between HLHS and TGA: Revisited

The results described in the previous section are compelling, because, as stated earlier, time-to-surgery was previously found to be predictive of *pre-operative* PVL in infants with TGA [10]. To begin to understand why time-to-surgery is predictive of PVL in both TGA and HLHS we took a closer look at the pre-operative cerebral hemodynamics presented in Section 6.4.1. Figure 41 shows pre-operative BFI, StO_2, OEF, and $CMRO_{2,I}$ for infants with HLHS and TGA who go to surgery on day-of-life 3 and earlier and who go to surgery on day-of-life 4 or later. As can be seen in Figure 41b, infants with both HLHS and TGA who wait longer for surgery have significantly lower

StO_2. Related to this is the result shown in Figure 41c, which shows that infants with both HLHS and TGA who wait longer for surgery have significantly higher OEF.

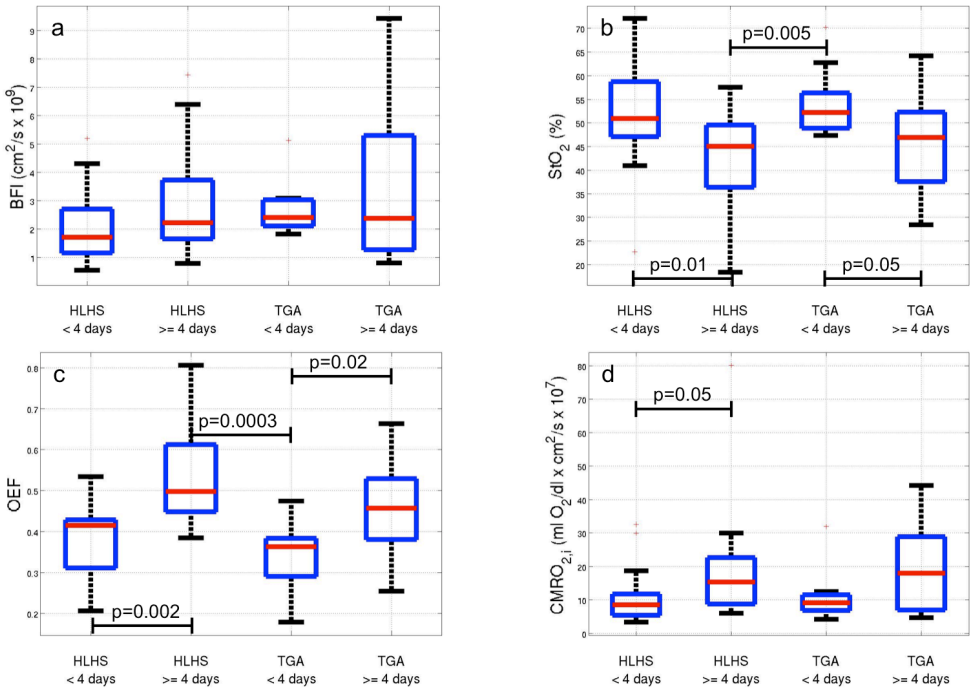

Figure 41: Boxplots of pre-operative BFI for infants with HLHS and TGA who went to surgery earlier or later than day-of-life 4. Pre-operative variables are BFI (a) StO_2 (b), OEF (c), $CMRO_{2,i}$ (d). Each diagnosis is separated into two groups, for patients going to surgery on day of life 3 or early and patients going to surgery on day of life 4 or later. The red line denotes the median value; the blue square extends to the 25th and 75th percentiles; the whiskers extend to the most extreme data points that are not outliers; and the outliers are plotted as individual points. All significant p-values calculated from a Wilcoxon rank-sum test are shown.

These results begin to hint at a mechanism behind the importance of time-to-surgery in the development of PVL in both cohorts of CHD patients. Additionally, these results support the finding from Section 6.4.2 and suggest that earlier surgery is as important for prevention of brain injury in infants with HLHS as it is in infants with TGA. Our original hypothesis that the post-operative time period is important in

predicting the development of PVL is now less supported. Because of these novel results I have just reported, we shifted our focus to the pre-operative time period. In section 6.4.4, I discuss my most recent work which begins this in-depth investigation into the pre-operative time period.

6.4.4 Serial pre-operative measurements

As previously stated, the results reported thus far in this section are from a protocol in which we only acquire DOS/DCS data on a patient on the day of their surgery. Thus, all trends with time-to-surgery are a cross-sectional look of our cohort. To fully understand the changes that are occurring as these patients are waiting for their surgery, we need to follow individual patients from birth until surgery.

My most recent work investigates longitudinal measurements of pre-operative cerebral hemodynamics on individual patients. Optical measurements, identical to the preoperative optical measurements performed on the morning of surgery and described in Section 6.2.2, were performed daily from birth until the morning of surgery. A total of N=16 patients with either HLHS (N=6) or TGA (N=10) have been studied so far. Figure 42 shows these daily measurements of StO_2 for the subjects with HLHS (left) and TGA (right). These plots suggest a negative trend in StO_2, however to quantify this, a linear regression was performed on each patient's data to quantify a slope. Although we have not yet recruited enough subjects to perform a meaningful multivariate analysis on these slopes, the results are promising. Of the 6 subjects with HLHS, 4 had a negative trend of StO_2 with age. The 2 subjects that did not exhibit a negative trend had the shortest times-to-surgery (2 and 3 days). For infants with TGA, the trends of StO_2 with age are even

more varied, however we observe a negative trend in the majority of patients studied so far. Further patients with perhaps more frequent measurements will be necessary to perform further statistical analysis on this data.

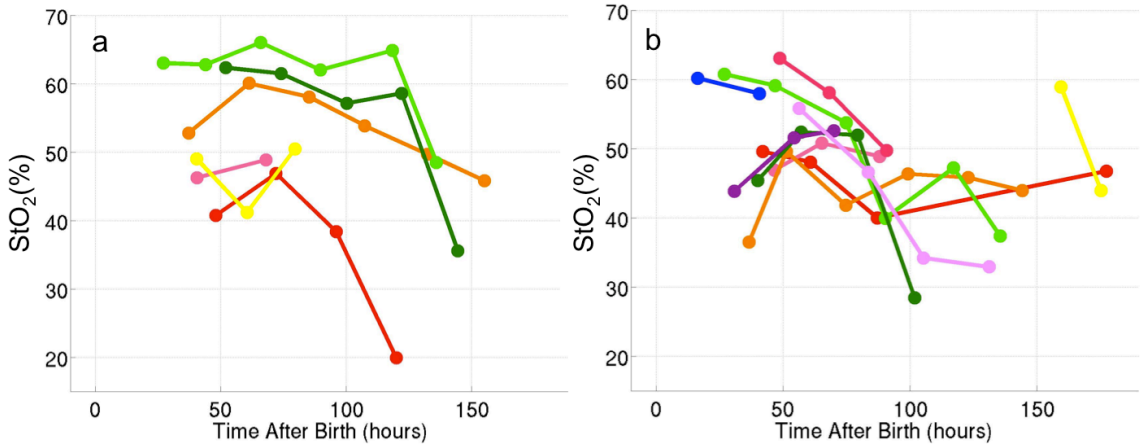

Figure 42: Daily measurements of StO_2 from birth until surgery in N=6 subjects with HLHS (left) and N=10 subjects with TGA (right).

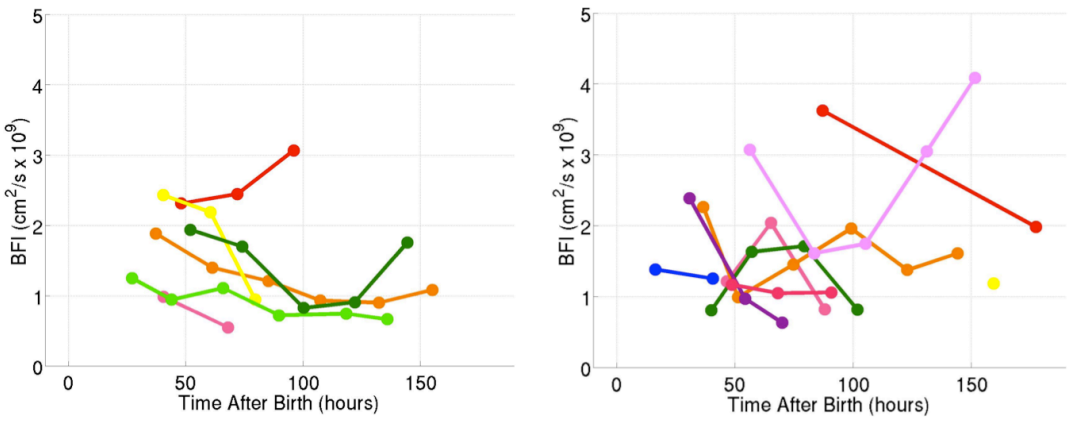

Figure 43: Daily measurements of BFI from birth until surgery in N=6 subjects with HLHS (left) and N=10 subjects with TGA (right).

Daily measurements of BFI were also acquired (Figure 43). We see a negative slope in linear fits of BFI versus age for all infants with HLHS and a majority (N=6/7) infants with TGA, however more subjects must be recruited before conclusions on the trends of cerebral hemodynamics with waiting time to surgery can be drawn.

6.5 Conclusion

I have studied pre- and post-operative cerebral oxygenation and blood flow in N=95 infants with critical congenital heart disease. I have focused my efforts to understanding risk factors for pre- and post-operative PVL in infants with hypoplastic left heart syndrome and transposition of the great arteries. I found that the prevalence of PVL is greater in infants with HLHS than with TGA, and that the majority of PVL seen in this cohort is observed on post-operative MRI scans. Specifically, we observed a large amount of new or worsened post-operative PVL in 48.7% (18/37) of patients in our cohort.

The main result reported herein is from the investigation of risk factors for acquired post-operative PVL in neonates with HLHS. The risk for injury in this population significantly increases with longer time to surgical repair. Additionally, a significant correlation exists between time-to-surgery and cerebral oxygen saturation, suggesting that changes in cerebral oxygen metabolism are occurring between birth and surgical repair and may be at the core to this increase risk for injury.

Comparisons of infants with HLHS and TGA show that both groups have higher cerebral oxygen extraction fractions and lower cerebral tissue oxygen saturation associated with longer time-to-surgery. The results suggest that correcting the native, abnormal vascular anatomy as soon as possible in both of these cohorts may be the most important factor in mitigating brain injury.

7 Conclusions and Future Directions

Over the past decade, research in the field of congenital heart disease has focused on improvements of neurodevelopmental outcomes. With the now understood high prevalence of brain injury in the form of periventricular leukomalacia (PVL) that exists in these children, current efforts aim to identify risk factors for this quantifiable injury Diffuse optical spectroscopies enable monitoring of highly relevant physiological parameters in this patient population, namely cerebral blood oxygenation and blood flow. In this thesis, I described the use of these techniques for the investigation of risk factors for PVL, among other studies.

The most important result from this dissertation concerns risk factors for new or worsened post-operative PVL in infants with hypoplastic left heart syndrome. Specifically, my work has shown that longer time-to-surgery, lower pre-operative cerebral oxygenation, and higher pre-operative cerebral blood flow, measured with diffuse optics, are associated with occurrence of new post-operative PVL and increases in post-operative PVL from pre-operative levels. This novel result paves the way for further exploration into the exact reasoning behind this association as well as possible prevention strategies in hospitals and situations when earlier surgery is not possible. Because of these results, the focus of research at CHOP has now shifted to concentrating on the pre-operative time period in infants with CHD. The future direction of the studies reported herein is to employ diffuse optical spectroscopy and diffuse correlation spectroscopy to monitor cerebral hemodynamics from birth until surgery in infants with congenital heart disease. Additionally, the effect of time-to-surgery on the risk for PVL needs to be

investigated in infants with other forms of CHDs, since currently this has only been shown in HLHS and TGA. The ultimate goals will be to pinpoint the ideal time for surgery and optimal values for cerebral oxygenation and blood flow to avoid PVL in all forms of CHD.

DOS and DCS are uniquely suited for pediatrics and especially for neonatal brain monitoring. Practically speaking, the relative thinness of the neonatal skull and scalp allows for deeper penetration of brain tissue. While this technology, especially DCS, has improved and expanded significantly over the past decade, there are several roadblocks that need to be overcome before DCS can be fully and widely integrated into a clinical setting. While DCS has been extensively shown to provide an accurate measurement of changes in CBF, validation of absolute blood flow has been carried out in limited populations and, in general, is less robust. Calibrating DCS measures to estimate absolute values of blood flow will depend on the accurate measurements of μ_s'. Improvement of this measurement, in turn, will depend on understanding the partial volume effects of the DOS measurements, accuracy in the source-detector separation, and improvements on the assumption of geometry.

In addition to improving the measurements of BFI, a user-friendly interface needs to be developed to give clinicians the ability to use these instruments with ease. Similarly, the patient interface needs to be improved. All of the work presented in this thesis was from measurements made only on the frontal cortex. Improvements in instrumentation need to be made to allow for more source-detector pairs and thus more

coverage of the brain. To do this, issues like interaction of hair follicles need to be addressed.

Despite these current roadblocks, I believe that diffuse optics will play a critical role in the clinical care of pediatric patients in the years to come. DOS and DCS will continue to be used in research for understanding the complex changes in cerebral physiology that are occurring after birth. Beyond its already impressive role in research, I believe that hybrid DOS/DCS devices will be commercialized and become part of clinical care. I envision these optical techniques will be used to individualize care and gather information about cerebral hemodynamics in real time. For instance, if two infant with CHD are born on the same day and one must be operated on first, optical monitoring of cerebral hemodynamics could lend insight into which patient is more at risk for acquiring injury and thus help clinicians make these difficult decisions.

In addition to infants with CHD, DOS and DCS will be a valuable tool in a multitude of pediatric, as well as adult, patient populations. Examples include understanding the relationship between healthy electroencephalography (EEG) signals during seizures with cerebral hemodynamics in different regions of the brain, which will provide clinicians valuable insight into the effects of these seizures on cerebral vasculature. I believe that within the next 20 years, hybrid DOS/DCS instruments will be part of clinical care and used for individual monitoring of patients cerebral hemodynamics at the bedside for individualizing patient care.

BIBLIOGRAPHY

1. Hoffman, J.I.E. and S. Kaplan, *The incidence of congenital heart disease.* Journal of the American College of Cardiology, 2002. **39**(12): p. 1890-1900.
2. Shillingford, A., et al., *Inattention, hyperactivity, and school performance in a population of school-age children with complex congenital heart disease.* Pediatrics, 2008. **121**(4): p. 759-767.
3. Bellinger, D., et al., *Neurodevelopmental status at eight years in children with dextro-transposition of the great arteries: the Boston Circulatory Arrest Trial.* The Journal of Thoracic and Cardiovascular Surgery, 2003. **126**(5): p. 1385-1396.
4. Mahle, W., et al., *Neurodevelopmental outcome and lifestyle assessment in school-aged and adolescent children with hypoplastic left heart syndrome.* Pediatrics, 2000. **105**(5): p. 1082-1089.
5. Majnemer, A., et al., *Long-term neuromotor outcome at school entry of infants with congenital heart defects requiring open-heart surgery.* Journal of Pediatrics, 2006. **148**(1): p. 72-77.
6. Wernovsky, G., A. Shillingford, and J.W. Gaynor, *Central nervous system outcomes in children with complex congenital heart disease.* Current Opinion in Cardiology, 2005. **20**(2): p. 94-99.
7. Mahle, W., et al., *An MRI study on neurological injury before and after congenital heart surgery.* Circulation, 2002. **106**(12 Suppl 1): p. 109-114.
8. Back, S.A., et al., *Selective vulnerability of late oligodendrocyte progenitors to hypoxia-ischemia.* The Journal of Neuroscience, 2002. **22**(2): p. 455-463.

9. Beca, J., et al., *New white matter injury after infant heart surgery is associated with diagnostic group and use of circulatory arrest.* Circulation, 2013. **127**: p. 917-979.

10. Petit, C.J., et al., *Preoperative brain injury in transposition of the great arteries is associated with oxygenation and time to surgery, not balloon atrial septostomy.* Circulation, 2009. **119**(5): p. 709-716.

11. Buckley, E.M., *Cerebral hemodynamics in high-risk neonates probed by diffuse optical spectroscopy.* University of Pennsylvania: Philadelphia, 2011.

12. Wintermark, M., et al., *Comparative overview of brain perfusion imaging techniques.* Stroke, 2005. **36**(9): p. 83-99.

13. Lynch, J.M., et al., *Noninvasive optical quantification of cerebral venous oxygen saturation in humans.* Academic Radiology, 2014. **21**(2): p. 162-167.

14. Jain, V., et al., *Cerebral Oxygen Metabolism in Neonates with Congenital Heart Disease Quantified by MRI and Optics.* Journal of Cerebral Blood Flow and Metabolism, Accepted.

15. Lynch, J.M., et al. *Cerebral blood flow response of intravenous adenosine infusion*. in *ISCBFM Brain 2013*. 2013. Shanghai, China.

16. Lynch, J.M., et al., *Time-to-Surgery and Pre-operative Cerebral Hemodynamics Predict Post-operative White Matter Injury in Neonates with Hypoplastic Left Heart Syndrome.* The Journal of Thoracic and Cardiovascular Surgery, Submitted.

17. Haskel, R.C., et al., *Boundary Conditions for the Diffusion Equation in Radiative Transfer.* Journal of the Optical Society of America A, 1994. **11**(10): p. 2727-2741.

18. Durduran, T., et al., *Diffuse optics for tissue monitoring and tomography.* Reports on Progress in Physics, 2010. **73**.

19. Fishkin, J. and E. Gratton, *Propagation of photon-density waves in strongly scattering media containing an absorbing semi-infinite plane bounded by a straight edge.* Journal of the Optical Society of America A, 1993. **10**(1): p. 127-140.

20. Fantini, S., et al., *Quantitative determination of the absorption spectra of chromophores in strongly scattering media- A ligt-emitting diode based technique.* Applied Optics 1994. **33**(22): p. 5204-5213.

21. Fantini, S., et al., *Non-invasive optical monitoring of the newborn piglet brain using continuous-wave and frequency-domain specroscopy.* Physics in Medicine and Biology, 1999. **44**(6): p. 1543-1563.

22. Arridge, S., M. Cope, and D.T. Delpy, *The theoretical basis for the determination of optical pathlengths in tissue: temporal and frequency analysis.* Physics in Medicine and Biology, 1992. **37**(7): p. 1531-1560.

23. Duncan, A., et al., *Optical pathlength measurements on adult head, calf and forearm and the head of the newborn infant using phase resolved optical spectroscopy.* Physics in Medicine and Biology, 1995. **40**(2): p. 295-304.

24. Prahl, S. *Optical Absorption of Hemoglobin*. 1999.

25. Wolthuis, R., et al., *Determination of water concentration in brain tissue by Raman spectroscopy.* Analytical Chemistry, 2001. **73**(16): p. 3915-3920.

26. Wyatt, J.S., et al., *Quantification of cerebral oxygenation and haemodynamics in sick newborn infants by near infrared spectrophotometry.* The Lancet, 1986. **328**(8515): p. 1063-1066.

27. Poser, C.M., *Arterial Behavior and Blood Circulation in the Brain.* The Journal of the American Medical Association, 1987. **257**(19).

28. Nitzan, M., et al., *Measurement of oxygen saturation in venous blood by dynamic near infrared spectroscopy.* Journal of Biomedical Optics, 2000. **5**(2): p. 155-162.

29. Skov, L., et al., *Estimation of cerebral venous saturation in newborn infants by near infrared spectroscopy.* Pediatric Research, 1993. **33**: p. 52-55.

30. Yoxall, C.W., et al., *Measurement of cerebral venous oxyhemoglobin saturation in children by near-infrared spectroscopy and partial jugular venous occlusion.* Pediatric Research, 1995. **38**: p. 319-323.

31. Goldberg, R.N., et al., *The effect of head position on intracranial pressure in the neonate.* Critical Care Medicine, 1983. **11**(6): p. 428-430.

32. Brown, D.W., et al., *NIRS measurement of venous oxygen saturation in the adult human head.* Adv Exp Med Biol, 2006. **578**: p. 251-256.

33. Franceschini, M.A., et al., *Near-infrared spiroximetry: noninvasive measurements of venous saturation in piglets and human subjects.* Journal of Applied Physiology, 2002. **92**(1): p. 372-384.

34. Leung, T.S., et al., *Cerebral tissue oxygen saturation calculated using low frequency haemoglobin oscillations measured by near infrared sectroscopy in adult ventilated patients.* Adv Exp Med Biol, 2008. **614**: p. 235-244.

35. Wolf, M., et al., *Continuous noninvasive measurement of cerebral arterial and venous oxygen saturation at the bedside in mechanically ventilated neonates.* Critical Care Medicine, 1997. **25**(9): p. 1579-1582.

36. Klabunde, R.E., *Cardiovascular Physiology Concepts Second Edition*2011: Lippincott Williams & Wilkins.

37. Franceschini, M.A., et al., *Near-infrared spiroximetry: noninvasive measurements of venous saturation in piglets and human subjects.* Journal of Applied Physiology, 2002. **92**: p. 372-384.

38. R Development Core Team, *R: A Language and Environment for Statistical Computing*2011: R Foundation for Statistical Computing.

39. Lin, L.I.-K., *A Concordance Correlation Coefficient to Evaluate Reproducibility.* Biometrics, 1989. **45**(1): p. 255-268.

40. Bland, J.M. and D.G. Altman, *Statistical methods for assessing agreement between two methods of clinical measurement.* Lancet, 1986. **1**(8476): p. 307.

41. Barratt-Boyes, B.G. and E.H. Wood, *The oxygen saturation of blood in the venae cavae, right-heart chambers, and pulmonary vessels of healthy subjects.* The Journal of Laboratory and Clinical Medicine, 1957. **50**(1): p. 93-106.

42. Boas, D.A., L.E. Campbell, and A.G. Yodh, *Scattering and imaging with diffusing temporal field correlations.* Physical Review Letters, 1995. **75**(9): p. 1855-1858.

43. Boas, D.A. and A.G. Yodh, *Spatially varying dynamical properties of turbid media probed with diffusing temporal light correlation.* Journal of the Optical Society of America A, 1997. **14**: p. 192-215.

44. Berne, B.J. and R. Pecora, *Dynamic Light Scattering with Applications to Chemisry, Biology, and Physics*1990, Malabar, FL: Krieger.

45. Brown, W., *Light Scattering: The Method and Some Applications*1993, New York: Clarendon.

46. Chu, B., *Laser Light Scattering, Basic Principles and Practice*1991, New York: Academic.

47. Ackerson, B.J., et al., *Correlation transfer: Application of radiative transfer solution methods to photon correlation problems.* Journal of Thermophysics and Heat Transfer, 1992. **6**(4): p. 577-588.

48. Buckley, E.M., et al., *Validation of diffuse correlation spectroscopic measurement of cerebral blood flow using phase-encoded velocity mapping magnetic resonance imaging.* Journal of Biomedical Optics, 2012. **17**(3): p. 037007.

49. Durduran, T., et al., *Optical measurement of cerebral hemodynamics and oxygen metabolism in neonates with congenital heart defects.* Journal of Biomedical Optics, 2010. **15**(3): p. 037004.

50. Buckley, E.M., et al., *Cerebral hemodynamics in preterm infants during positional intervention measured with diffuse correlation spectroscopy and transcranial Doppler ultrasound.* Optics Express, 2009. **17**(15): p. 12571-12581.

51. Diop, M., et al., *Comparison of time-resolved and continuous-wave near-infrared techniques for measuring cerebral blood flow in piglets.* Journal of Biomedical Optics, 2010. **15**(5): p. 057004-057004.

52. Kim, M.N., et al., *Noninvasive measurement of cerebral blood flow and blood oxygenation using near-infrared and diffuse correlation spectroscopies in critically brain-injured adults.* 2010.

53. Zhou, C., et al., *Diffuse optical monitoring of hemodynamic changes in piglet brain with closed head injury.* Journal of Biomedical Optics, 2009. **14**(3): p. 034015.

54. Winn, H.R., S. Morli, and R.M. Berne, *The Role of Adenosine in Autoregulation of Cerebral Blood Flow.* Annals of Biomedical Engineering, 1985. **12**(2): p. 8.

55. Forrester, T., et al., *Effect of adenosine triphosphate and some derivatives on cerebral blood flow and metabolism.* The Journal of Physiology, 1979. **296**: p. 343-355.

56. Heistad, D.D., et al., *Effect of adenosine and dipyridamole on cerebral blood flow.* American Journal of Physiology, 1981. **240**(5): p. H775-H780.

57. Hussain, R., et al., *Vasodilatory effect of adenosine triphosphate does not change cerebral blood flow: a PET study with (15)O-water.* Annals of Nuclear Medicine, 2009. **23**(8): p. 717-723.

58. Sollevi, A., et al., *Effect of adenosine on human cerebral blood flow as determined by positron emission tomography.* Journal of Cerebral Blood Flow and Metabolism, 1987. **7**(6): p. 673-678.

59. Banks, B.A., et al., *Changes in oxygenation with inhaled nitric oxide in severe bronchopulmonary dysplasia.* Pediatrics, 1999. **103**(3): p. 610-618.

60. Tanaka, Y., et al., *Inhaled nitric oxide therapy decreases the risk of cerebral palsy in preterm infants with persistent pulmonary hypertension of the newborn.* Pediatrics, 2007. **119**(6): p. 1159-1164.

61. Kety, S.S. and C.F. Schmidt, *The effects of altered arterial tensions of carbon dioxide and oxygen on cerebral blood flow and cerebral oxygen consumption of normal young men.* The Journal of Clinical Investigation, 1948. **27**(4): p. 484-492.

62. Watson, N.A., et al., *The effect of hyperoxia on cerebral blood flow: a study in healthy volunteers using magnetic resonance phase-contrast angiography.* European Journal of Anaesthesiology, 2000. **17**(3): p. 152-159.

63. Xu, F., et al., *Effect of hypoxia and hyperoxia on cerebral blood flow, blood oxygenation, and oxidative metabolism.* Journal of Cerebral Blood Flow and Metabolism, 2012. **32**: p. 1909-1919.

64. Graham, E.M., et al., *Comparison of Norwood Shunt Types: Do the Outcomes Differ 6 Years Later?* Ann Thorac Surg, 2010. **90**(1): p. 31-35.

65. Bellinger, D., et al., *Adolescents With d-Transposition of the Great Arteries Corrected With the Atrial Switch Procedure.* Pediatric Cardiology, 2011. **124**: p. 1361-1369.

66. Marino, B., et al., *Neurodevelopmental outcomes in children with congenital heart disease: evaluation and management: a scientific statement from the American Heart Association.* Circulation, 2012. **126**(9): p. 1143-1172.

67. Andropoulus, D., et al., *Brain immaturity is associated with brain injury before and after neonatal cardiac surgery with high-flow bypass and cerebral oxygenation monitoring.* The Journal of Thoracic and Cardiovascular Surgery, 2010. **139**(3): p. 543-556.

68. Bellinger, D., et al., *Developmental and neurologic effects of alpha-stat versus pH-stat strategies for deep hypothermic cardiopulmonary bypass in infants.* The Journal of Thoracic and Cardiovascular Surgery, 2001. **121**(2): p. 374-383.

69. Gaynor, J., et al., *Abstract 12437: Early Neurodevelopmental Outcomes after Cardiac Surgery in Infancy Have Not Improved; A Multi-center Retrospective Analysis of 1,718 Patients.* Circulation, 2012. **126**: p. A12437.

70. Dent, C., et al., *Brain magnetic resonance imaging abnormalities after the Norwood procedure using regional cerebral perfusion.* The Journal of Thoracic and Cardiovascular Surgery, 2005. **130**(6): p. 1523-1530.

71. Goff, D.A., et al., *Noninvasive Cerebral Perfusion Imaging in High-Risk Neonates.* Seminars in Perinatology, 2010. **34**(1): p. 46-56.

72. Norwood, W.I., *Hypoplastic left heart syndrome.* The Annals of Thoracic Surgery, 1991. **52**: p. 688-695.

73. Goff, D.A., et al., *Risk factors for preoperative periventricular leukomalacia in term neonates with hypoplastic left heart syndrome are patient related.* The Journal of Thoracic and Cardiovascular Surgery, 2013.

74. Centers for Disease Control and Prevention (CDC), *Improved national prevalance estimates for 18 major birth defects--United States, 1999-2001.* Morbidity and Mortality Weekly Report, 2006. **54**(51): p. 1301-1305.

75. Beca, J., et al., *Pre-operative brain injury in newborn infants with tarnsposition of the great arteries occurs at rates similar to other complex congenital heart disease and is not related to balloon atrial septosomy.* Journal of the American College of Cardiology, 2009. **53**(19): p. 1807-1811.

76. Block, A., et al., *Clinically silent preoperative brain injuries do not worsen with surgery in neonates with congenital heart disease.* The Journal of Thoracic and Cardiovascular Surgery, 2010. **140**(3): p. 550-557.

77. Anderson, B., et al., *Earlier arterial switch operation improves outcomes and reduces costs for neonates with transposition of the great artieries.* Journal of the American College of Cardiology, 2014. **63**(5): p. 481-487.

78. Yushkevich, P., et al., *User-guided 3D active contour segmentation of anatomical structures: Significantly improved efficiency and reliability.* Neuroimage, 2006. **31**(3): p. 1116-1128.

79. Childs, A.M., et al., *Cerebral maturation in premature infants: quantitative assessment using MR imaging.* American Journal of Neuroradiology, 2001. **22**: p. 1577-1582.

80. Licht, D.J., et al., *Brain maturation is delayed in infants with complex congenital heart defects.* The Journal of Thoracic and Cardiovascular Surgery, 2009. **137**(3): p. 529-536.

81. Tabbutt, S., et al., *Risk factors for hospital morbidity and mortality after the Norwood procedure: A report from the Pediatric Heart Network Single Ventricle Reconstruction trial.* The Journal of Thoracic and Cardiovascular Surgery, 2012. **144**(4): p. 882-895.